2015

Computational Modeling of 3D Actin Organization through Polymerization, Turnover, Crosslinking, and Motor Pulling

Haosu Tang
Lehigh University

Computational Modeling of 3D Actin Organization through Polymerization, Turnover, Crosslinking, and Motor Pulling

by

Haosu Tang

A Dissertation

Presented to the Graduate and Research Committee

of Lehigh University

in Candidacy for the Degree of

Doctor of Philosophy

in

Department of Physics

Lehigh University

May 2015

Approved and recommended for acceptance as a dissertation in partial fulfillment of the requirements for the degree of Doctor of Philosophy

Haosu Tang
Computational Modeling of 3D Actin Organization through Polymerization, Turnover, Crosslinking, and Motor Pulling

_____

Defense Date

_____

Dimitrios Vavylonis
Dissertation Director

_____

Approved Date

Committee Members:

_____

James D. Gunton

_____

Xiaolei Huang

_____

Jeetain Mittal

_____

Daniel Ou-Yang

ACKNOWLEDGMENTS

First and foremost I offer my sincerest gratitude to my advisor, Dr. Dimitrios Vavylonis, who has supported me throughout my Ph. D. research with his patience and knowledge. His virtues of honesty, humility, diligence and curiosity are the beacon to not only my career in science but also my life. For that I am forever grateful.

I owe a great deal of my success to the rest of my thesis committee: Drs. James Gunton, Xiaolei Huang, Jeetain Mittal and Daniel Ou-Yang, for their knowledgeable insights on my thesis work and kind guidance as mentors.

I would like to thank the Vavylonis' group members that I spent the last few years with. Special thanks go to Drs. Nikola Ojkic, Tyler Drake, Tamara Bidone and Matthew Smith, who offered valuable advices that helped me carry on research, and at the same time being wonderful friends.

I thank my dear friends, both in the US and back in China, for their help and company. I was constantly impressed by their wit and humor. The cheerful moments we spent together composed the most cherished memory of my life. I thank Shijue Wang for weathering the storm alongside me. For her love and caring with continued understanding and respect.

Finally, I owe heartfelt gratitude to my father Jinnan Tang, mother Yaping Wu for their endless love and support. For creating an environment that kindled my early interest in science. For encouraging me to overcome adversity during my endeavor in research. For always having faith and taking pride in me. Thank you.

Table of Contents

List of Figures

List of Tables

Abstract

The cellular actin cytoskeleton is an intricate system of actin filaments that supports cell morphology and is crucial for numerous cell functions including cell growth and cell division. Among the most important actin cytoskeleton structures are actin cables and cytokinetic ring, which are bundles of actin filaments. The actin cables span the cell and serve as tracks for vesicle transport while the actin cytokinetic ring forms in the middle and constricts to divide the cell. The focus of my work is to gain a quantitative understanding of how such cables and ring are formed, what are the essential components, how overexpression and underexpression of certain proteins will affect the structure and dynamics. I built a 3D computational model that starts out from the basic physical and mechanical properties of actin filaments and accounts for known interactions with other proteins, to reproduce the experimental observations of the actin cytoskeleton in different cell systems and further make testable predictions for cell mutants.

First, I modeled individual actin filament as a semiflexible worm like chain. I coarse grained the filamentous actin segment using a bead-spring model with spring, bending and thermal forces. This model represents of the actin filament's spatial and dynamical properties. I tested that the model reproduces the correct persistence length, relaxation dynamics and equipartition of energy.

Second, to obtain a quantitative understanding of these actin structures and dynamics in fission yeast, I extended the individual actin filament model and added actin-interacting

factors. Polymerization out of formin cortical sites, bundling by cross-linkers, pulling by type V myosin, and severing by cofilin, are simulated as growth, cross-linking, pulling and turnover of the semiflexible polymers. With the above mechanisms my quantitative model generated actin cable structures and dynamics similar to those observed in live cell experiments. The simulations reproduced the particular actin cable structures in *myoVΔ* cells and predicted the effect of increased myosin V pulling. I found that increasing cross-linking parameters generated thicker actin cables and led to anti-parallel and parallel phases with straight or curved cables. I further analyzed the cable number, curvature and loop occurrences of experimental images of cells overexpressing crosslinkers and cell treated with drugs that depolymerize actin patches, provided by our collaborator Damien Laporte. Our predictions are in quantitative agreement with the experiments. Furthermore, the model predicts that clustering of formins at cell tips promotes actin cable formation.

Third, I adapted the actin cable model to budding yeast, another well-studied model organism. Budding yeast differs from fission yeast in that it has a more complex geometry and different types of interacting proteins. I refined the previous fission yeast actin cable model by considering a more accurate model of orientation-dependent crosslinking by fimbrin and a more accurate aging mechanism for turnover. It also included polymerization by formins at the bud tip and bud neck, crosslinking, severing, and myosin pulling. Parameter values were estimated from prior experiments. The model generates actin cable structures and dynamics similar to those of wild type and formin deletion mutant cells. Simulations with increased polymerization rate result in long, wavy

cables. Simulated pulling by type V myosins stretches actin cables. Increasing the affinity of actin filaments for the bud neck together with reduced myosin V pulling promotes the formation of a bundle of antiparallel filaments at the bud neck, which I suggest as a model for the assembly of actin filaments to the contractile ring.

Finally, my colleague Dr. Tamara Bidone and I further extended the model to simulate the actin contractile ring. We showed that the ring formation region in parameter space lies close to regions leading to clumps, meshworks or double rings, and stars/cables, which are consistent with prior experiments with mutations that alter the morphology of the condensing network. We also quantified tension along actin filaments and forces on nodes during ring assembly and showed that the mechanisms describing ring assembly can also drive ring constriction once the ring is formed.

In summary, this work provides a numerical way to study the morphology and dynamics of the actin cytoskeleton in model cell organisms. Combining simulated, analytical and experimental results, the proposed model with minimal set of interactions successfully reproduced experimental observations and made predictions for further studies.

Chapter 1 Introduction

1.1 Organization of this Thesis

Cells are units of life. How cells sense the environment, maintain shapes, migrate, organize polarized growth and divide, all involve one important type of protein - actin. In this thesis, I study the structure and dynamics of actin cables and actin cytokinetic ring, two common actin structures, in model organism yeasts. The thesis is organized into five chapters corresponding to two published papers and one submitted at the time of writing.

The first chapter serves as an background introduction to actin, actin cytoskeleton and model organism yeasts. An overview of multiple types of actin interacting proteins is then presented regarding their crucial roles in organizing actin filaments into complex structures. Furthermore, I discuss some of the previous physical models intended to interpret the actin structure and its mechanical properties.

The second chapter describes how I model the actin filament using a semiflexible bead-spring chain. This is a 3D generalization of a previously developed 2D model (Laporte *et al.*, 2012) and other works of the semiflexible polymer model (Pasquali *et al.*, 2001; Nédélec and Foethke, 2007). I validated this model in the 3D space by testing the mechanical and dynamic properties.

In the third chapter, I show how the addition of polymerization, turnover, crosslinking and pulling can reproduce and predict the actin cable features observed in fission yeast.

Our collaborator, Dr. Damien Laporte, provided experimental images for us to do analysis and compare with the simulations.

The fourth chapter describes how I refined the previous model, especially turnover and crosslinking mechanisms. I applied the model to budding yeast system and was able to explore different factors that affects the dynamics of actin cables and transition from cables to actomyosin ring.

The fifth chapter describes the effort we put into extending this model to cytokinetic ring assembly in fission yeast. Dr. Tamara Bidone, a postdoc in our group, added node capture mechanism and analyzed the morphological and mechanical properties of the contractile ring model.

1.2 Actin Cytoskeleton in Yeast Systems

Actin, an ancient protein found in the earliest life forms, is ubiquitous in all eukaryotic cells. Actin is a globular protein, consisting of four subdomains, forming a U shape (Figure 1A). Actin monomers (G-actin) polymerize into a two-stranded helical chain called actin filaments (F-actin) through spontaneous nucleation and elongation (Figure 1B). These actin filaments are a crucial component of the cytoskeleton (along with microtubules and intermediate filaments), which gives rise to numerous cellular processes, including cell motility, maintenance of shape, mechanosensing, polarity and division (Pollard and Borisy, 2003; Pollard and Earnshaw, 2004; Pollard and Cooper, 2009; Kovar *et al.*, 2011; Blanchoin *et al.*, 2014; Mishra *et al.*, 2014). The actin filaments organize into bundle and network structures with the help of nucleating, side-binding,

severing, crosslinking and capping proteins (Figure 1C-E). With different kinds of actin binding proteins, actin filaments form diverse actin network structures in the cell system (Figure 1F), including actin cables, patches and cytokinetic ring, which would be described in the following paragraphs. Lamellipodia made of actin filaments branched by the Arp2/3 complex, undergo treadmilling and drives cell motility at the leading edge. Filapodia, bundles of actin filaments crosslinked by fascin, serve the adherent cells to explore the environment. Stress fibers, actin bundles pulled by myosin motors, provides force for cell adhesion and morphogenesis (Pollard and Earnshaw, 2004; Ridley, 2011; Blanchoin *et al.*, 2014).

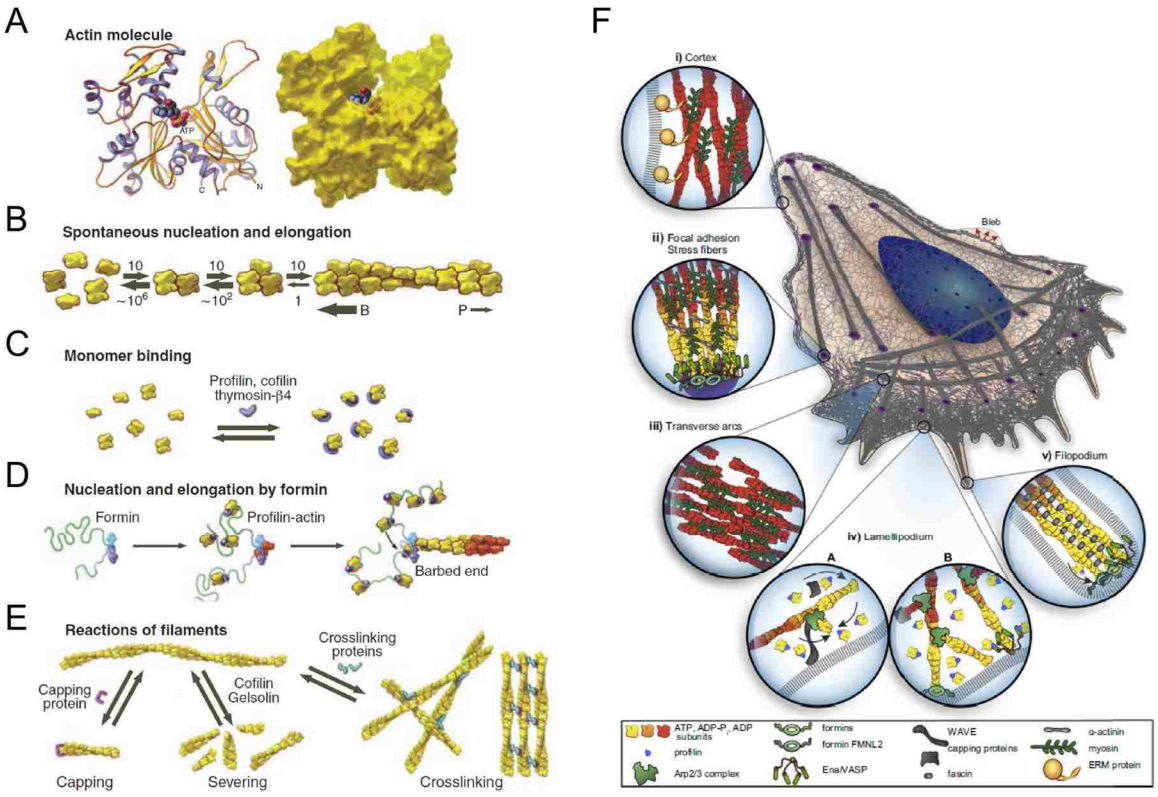

Figure 1. Structures of actin, actin filament and cellular actin organizations. (A) Ribbon and space-filling models of the actin molecule. (B) Spontaneous nucleation and elongation. Dimers

and trimers are unstable. Longer polymers grow rapidly at the barbed end and slowly at the pointed end. (C) Actin monomer binding proteins. Profilin promotes nucleotide exchange and inhibits pointed-end elongation and nucleation but not barbed-end elongation; cofilin inhibits nucleotide exchange and promotes nucleation. (D) Nucleation and elongation by formins. Formins initiate polymerization from free actin monomers and remain associated with the growing barbed end. Profilin-actin binds to formin and transfers actin onto the barbed end of the filament. (E) Reactions of actin filaments. Capping proteins bind to and block barbed ends; cofilin and gelsolin sever filaments; cross-linking proteins assemble networks and bundles of actin filaments. (F) Examples of actin organization structures in motile cell i) cell cortex anchoring the membrane, ii) stress fibers, which are contractile bundles attached to focal adhesions iii) transverse arcs found at the back of the lamellipodium iv) the lamellipodium, which are branched actin networks v) filopodia, filled with parallel actin bundles crosslinked by fascin. Panels (A-E) are reproduced from (Pollard and Cooper, 2009) and (F) from (Blanchoin *et al.*, 2014).

Yeast is a good model organism to study actin related processes such as cell polarity, endocytosis and mitosis for the following reasons: 1) its rigid cell wall that prevents itself from undergoing locomotion, 2) its relatively simple shape and actin cytoskeleton, 3) its ability to undertake genetic modifications and microscopic imaging (Moseley and Goode, 2006; Kovar *et al.*, 2011; Mishra *et al.*, 2014). A study of yeast actin cytoskeleton provides implications for other cell systems. In this thesis work, I study fission yeast (*Schizosaccharomyces pombe*) and budding yeast (*Saccharomyces cerevisiae*), two widely used model systems. Fission yeast has a rod-like shape – a cylinder capped by two hemispheres. The typical length of wild type fission yeast ranges from 5 μm to 20 μm as it undergoes different phases of the cell cycle (Figure 2A). During G1 phase, usually the longest phase right after division, the fission yeast grows in size and mass. In S phase,

chromosomes in fission yeast are duplicated. G2 phase is the growth phase right before division where enzymatic activities take place and the cell prepares for mitosis. During G2, the cell shape and the actin cable structure are most stable. Mitosis represents the whole process of cell division. First, two poles of the mitotic spindle form and the microtubules emanating from the two poles accumulate sister chromatids at the cell middle. The sister chromatids then separate from each other and a cytokinetic ring of actin and myosin forms and contracts, dividing into two daughter cells (Pollard and Earnshaw, 2004) (Figure 2C). Budding yeast has very similar cell cycle process. Budding yeast (G2 phase) has a relatively more complex cell shape than fission yeast – it consists of two ellipsoids, one large (mother) and the other small (bud), connected at the neck (Figure 2B). In this study, I build 3D computational models that study the actin cable structures during G2 phase for both fission yeast (Tang *et al.*, 2014) and budding yeast (Tang *et al.*, 2015) and we further extended this model with previous 2D model to study the cytokinetic ring assembly in cytokinesis (final stage of M phase) (Bidone *et al.*, 2014).

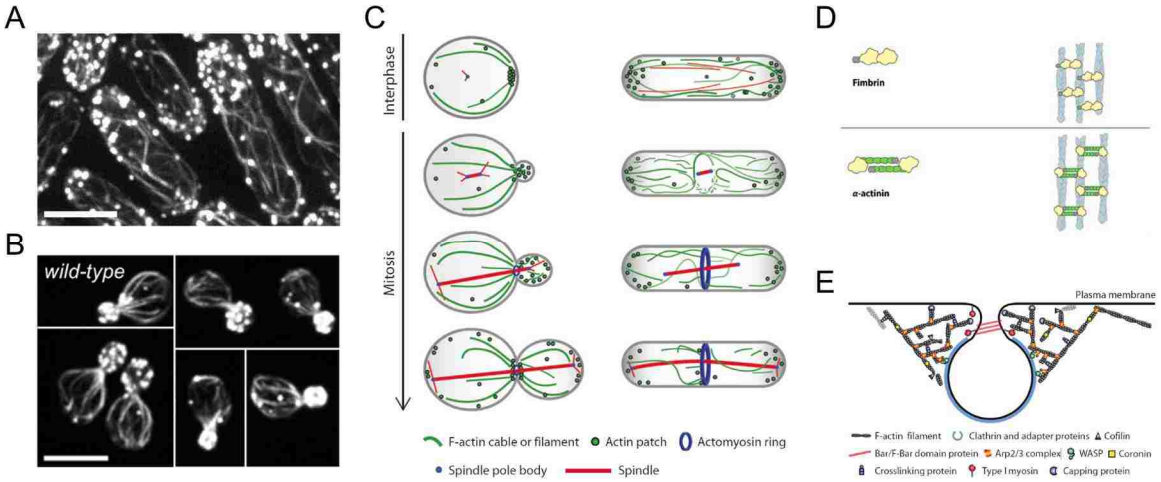

Figure 2. Actin organization structures in fission yeast and budding yeast. (A) Images of actin cables in fission yeast. GFP-CHD tagged actin showing structures of actin cables (bright lines) and actin patches (bright dots). (B) Actin cables in budding yeast. Cells were grown to log phase at 25°C in YEPD, fixed, and stained with Alexa Fluor 488–phalloidin. Bars = 5 μm. (C) Actin organization during cell cycle in budding yeast and fission yeast. In both budding yeast (left panel) and fission yeast (right panel), F-actin forms three distinct filamentous structures: actin patches, actin cables, and actin ring. Actin patches are assembled at the endocytic sites, and their distribution is correlated with region of polarized growth. Actin patches appear at the cell growth zones during interphase and the cell division site during late mitosis. Actin cables are present in all stages of cell cycle in both yeasts, run along the length of the cell, and are involved in intracellular cargo transport. In fission yeast, actin cables also play a role in actin ring assembly. Actin ring (depicted in blue) is assembled at the division site early in mitosis, which constricts after completion of anaphase to divide the mother cell into two daughter cells. Microtubules are shown in red. (D) Actin crosslinkers fimbrin and α-actinin dimers form actin bundles. (E) A cross-section of an endocytic actin patch. Actin patch assembles at the endocytic sites. Clathrin and adaptor proteins arrive early and mark the endocytic site. The Arp2/3 complex nucleates a dense network of branched actin filaments by generating a new branch of F-actin on a pre-existing filament at an angle of 70°. WASP and myosin 1 are the two NPFs (nucleation promoting factors) of the Arp2/3 complex present in spatially distinct regions of actin patches. Myosin 1 is localized to the neck region of the endocytic vesicle, while the WASP protein localizes to more distal region. Fimbrin cross-links the actin filaments in the actin patches. Capping proteins cap the filaments and limit their growth, and filaments are severed by cofilin. These two families of proteins along with coronin control the filament length and dynamics of the actin network in cortical patches. BAR- and F-BAR-domain-containing amphiphysin proteins cooperate with F-actin to promote membrane invagination and scission. Figure panel (A) is reproduced from (Tang *et al.*, 2014), (B) from (Graziano *et al.*, 2014), (C) and (E) from (Mishra *et al.*, 2014) and (D) from MBInfo (www.mechanobio.info).

In G2 fission yeast and budding yeast, actin monomers form two major types of structures: patches and cables (Figure 2A and B). Actin patches are dendritic networks of actin filaments branched by Arp2/3 complex and capped by Acp1/2. They are involved in the endocytosis process, where the cell engulfs macromolecules from outside the cell body (Kubler and Riezman, 1993; Moseley and Goode, 2006; Mishra *et al.*, 2014). Clathrin forms a coat around the site of cell invagination. Short, dense actin filaments then accumulate around these endocytic sites and help to sever and drive the sac motion (Figure 2E). Actin cables, on the other hand, are bundles of long actin filaments that provide tracks for polarized vesicle transport. With the help of formins, crosslinking proteins, myosin motors, severing proteins and side binding proteins, actin cables function in a dynamic way with traceable properties and characteristics (Figure 2C and Figure 3C).

In cytokinesis, the major actin structure of interest is the contractile ring. In the fission yeast, the cytokinetic ring assembles from a broad band of membrane-associated node complexes, which bind myosin II molecular motors and Cdc12 formins. The nodes condense into a narrow ring in a process that depends on actin polymerization and lasts about 10 minutes (Lee *et al.*, 2012; Mishra *et al.*, 2014) (Figure 2C).

1.3 Mechanisms of Actin-associated Proteins

Actin filament dynamics are regulated by multiple proteins that bind to the filament sides, the filament ends, and to actin monomers. They affect nucleation, regulate

polymerization and turnover. Here I review a few important actin associated protein mechanisms that are relevant to this thesis.

Formins. Formin proteins bind to the barbed end of the actin filament and regulated its polymerization rate by recruiting actin subunits from solution and transferring them to the filament end. They localize at the cell cortex and nucleate and polymerize actin filaments growing out of the cell membrane (Faix and Grosse, 2006; Chesarone *et al.*, 2010; Firat-Karalar and Welch, 2011). In fission yeast, growing and shrinking microtubules deposit transient landmark protein aggregates to the cell tips. Formin proteins For3 are then recruited at these cortical landmarks and nucleate actin filament (Feierbach and Chang, 2001; Kovar, 2005; Martin *et al.*, 2005) (Figure 3C). In budding yeast, there are two types of formins: Bni1p, which localizes at the bud tip, and Bnr1, which localizes at the bud neck. Besides the location, these two types of formins differ further in their abilities to polymerize actin filaments (Kovar and Pollard, 2004; Moseley and Goode, 2005; Paul and Pollard, 2008; Miao et al., 2013; Graziano et al., 2014) (Figure 3D and E). *In vitro* experiments show that, under the same actin monomer and formin concentration, Bnr1 is a order of magnitude more potent than Bni1p in polymerizing actin filaments (Moseley and Goode, 2005).

Cofilin. In both fission and budding yeasts, severing protein cofilin (Cof1) binds to the sides of actin filaments (Nakano and Mabuchi, 2006; Chen and Pollard, 2011) and destablizes the actin filament (Figure 1E and Figure 3C). Cof1 provides a twist to the filament and thus can sever it with the help of Aip1 (Moseley and Goode, 2006), thus allowing constant actin turnover. Other proteins such as profilin Prf1p, tropomyosin

Tpm1p, actin-interacting protein Aip1 and cyclase-associated protein work together with cofilin to regulate the severing events and increases the turnover rate (Moon *et al.*, 1993; Balcer *et al.*, 2003; Andrianantoandro and Pollard, 2006; Okada *et al.*, 2006; Fan *et al.*, 2008; Bugyi *et al.*, 2010; Chaudhry *et al.*, 2013).

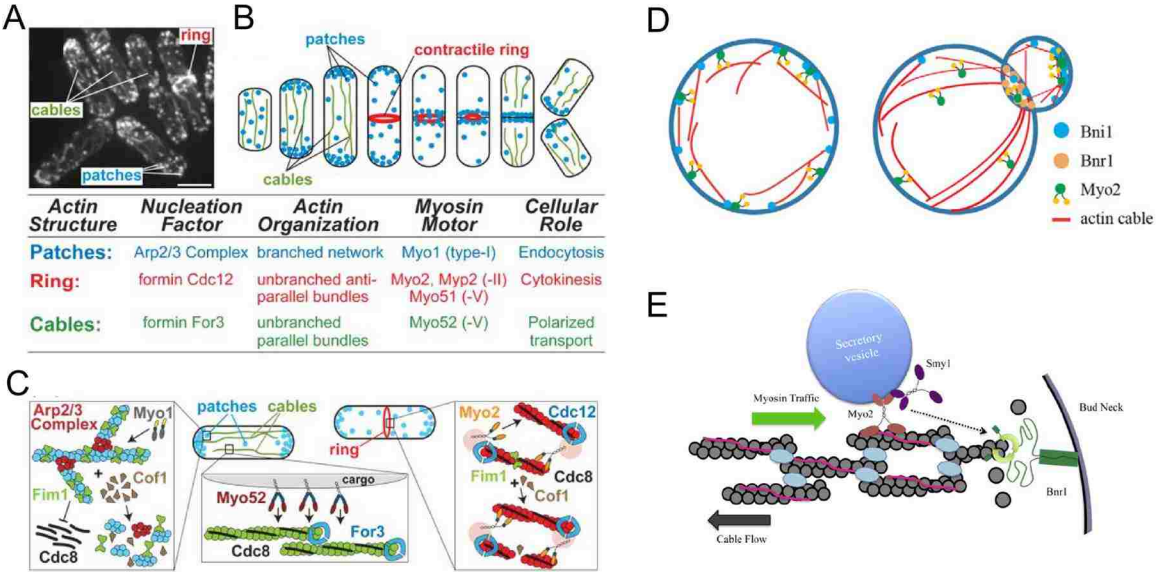

Figure 3. Actin-associated protein mechanisms for fission yeast and budding yeast. (A) Fluorescent image of the actin cytoskeleton expressing the general F-actin marker GFP-CHD. (B) Cartoon summarizing the subcellular distribution of actin structures during the cell cycle (centering on mitosis). The table below highlights the basic features and roles of the three actin structures. (C) Regulation of actin filament turnover and myosin motors by tropomyosin and fimbrin. Actin patches: High concentrations of fimbrin Fim1 prevent tropomyosin Cdc8 from binding the Arp2/3 complex-nucleated branched filaments, which allows efficient cofilin Cof1-mediated actin filament turnover and recruitment of myosin-I Myo1. Actin cables: tropomyosin favors myosin-V Myo52-directed motility on formin For3-nucleated straight parallel filaments. Contractile rings: Lower concentrations of fimbrin allow limited cofilin severing by partially inhibiting tropomyosin. Tropomyosin also favors myosin-II Myo2-mediated compaction of the

formin Cdc12-nucleated straight antiparallel filaments. (D) In unpolarized G1 cells, actin cables are randomly oriented and their polymerization is largely mediated by the cortical formin Bni1. Bnr1 is supposedly kept inactive by Bud14. In polarized cells cable become mostly oriented towards the bud neck, where they are polymerized by bud-neck-confined Bnr1. At the same time, Bni1 is recruited to the bud tip and bud neck, where it also participates in the generation of polarized cable array. Myo2 is depleted from the cell cortex and targeted to the bud by polarized transport. (E) A model for Smy1 regulation of Bnr1-mediated actin cable assembly. Bnr1 (green) is tethered to the bud neck and polymerizes actin filaments that are incorporated into extending cables. The filaments in cables become decorated with tropomyosin (pink) and bundling proteins (turquoise), which maintain filament organization and stability. Myosin-V (Myo2 in yeast, red) rapidly transports secretory vesicles and Smy1 (purple) on actin cables to the bud neck, where Smy1 transiently interacts with Bnr1 to reduce the speed of actin cable extension and prevent cable overgrowth. Figure panels and captions (A)-(C) are reproduced from (Kovar *et al.*, 2011), (D) from (Yu *et al.*, 2011), and (E) from (Chesarone-Cataldo *et al.*, 2011a).

Crosslinkers. Actin filament cross-linking proteins keep the filaments together in bundles. Cross-linking protein fimbrin Sac6 is found in budding yeast cables (Moseley and Goode, 2006) but not fission yeast fimbrin Fim1 (Nakano *et al.*, 2001; Wu *et al.*, 2001; Skau *et al.*, 2011), likely because of its low concentration (Figure 3E and Figure 2D). α-actinin (Ain1) is another cross-linker in fission yeast that may contribute to actin cable bundling. The highly compacted fimbrin is a smaller crosslinker than α-actinin (Figure 2D). Both Fim1 and Ain1 can bundle filaments in parallel or anti-parallel orientations (Skau and Kovar, 2010; Skau *et al.*, 2011; Falzone *et al.*, 2012; Laporte *et al.*, 2012).

Myosins. Myosin motor proteins carry cargo along actin cables, a mechanism that is important as an intracellular transport mechanism. In fission yeast, myosin V motor proteins (Myo51, Myo52), carrying secretory vesicles or anchoring on organelles, walk along actin filament towards the barbed end (Lo Presti *et al.*, 2012) (Figure 3C). Some of these myosin V molecules associate with the cortical endoplasmic reticulum that is tightly attached to the plasma membrane while the two heads remain bound to actin cables (Zhang *et al.*, 2012). In budding yeast, type V myosin Myo2 works in a similar way as in fission yeast except for the processivity and walking speed (Schott *et al.*, 2002a; Sheltzer and Rose, 2009; Hodges *et al.*, 2012b) (Figure 3E). Myo2 motor processivity and velocity depend greatly on different types of cargo Myo2 carries and the location as it travels (Reck-Peterson *et al.*, 2001a; Hodges *et al.*, 2009; Hodges *et al.*, 2012b). Smy1, a passenger protein transported to the Bnr1 sites and interacts with Bnr1 to reduce cable elongation rate and prevent cable overgrowth (Chesarone-Cataldo *et al.*, 2011a) (Figure 3E). Furthermore, a different type of myosin, type II myosin Myo1, which localizes around the bud neck (Bi *et al.*, 1998b; Lippincott and Li, 1998; Vallen *et al.*, 2000), affects the actin cable dynamics in budding yeast (Huckaba *et al.*, 2006; Higuchi *et al.*, 2013) (Figure 3D).

1.4 Physical Models Describing the Actin Network

Mathematical and computational models have proven to be very useful in reproducing and predicting the properties of the cytoskeleton (Carlsson *et al.*, 2010; Mogilner and Odde, 2011; Yamaoka *et al.*, 2012; Sept and Carlsson, 2014; Unterberger and Holzapfel, 2014). With increasing knowledge of physical and chemical properties of various

proteins, modeling can be applied to a wide range of systems covering different space and time scales (Figure 4A). At the Angstrom level (10^{-10} m), molecular dynamic (MD) simulations are used to describe the microstructure and dynamics of actin (Pfaendtner *et al.*, 2009). MD–based methods can also be used to slightly larger systems such as actin filament in solvent with various actin-binding proteins, at the in nanometer level (10^{-9} m) (Matsushita *et al.*, 2010; Pfaendtner *et al.*, 2010). At this level, fine structures of proteins are sometimes neglected and coarse-grained to bypass the computational complexity. When studying the process of actin filament elongation, mathematical models can represent the addition and subtraction of actin subunits as a random walk along the filament length (Hill, 1987; Vavylonis *et al.*, 2005). The topic of this thesis is the behavior of actin filaments and actin networks at the micrometer level (10^{-6} m), within live cells.

The cell system itself is in nature complex, with a myriad of molecules forming proteins functioning in completely diverse ways. A theoretical model that accounts for all molecular scale interactions, and builds up a whole cellular system is hardly attainable. But with the knowledge of measured kinetic data on the interactions of many of the players in actin biochemistry made possible the creation of more detailed and accurate models that could permit investigators to dissect interdependent roles of individual molecular components (Ditlev *et al.*, 2013). And therefore a lot of the models in this field are phenomenological or conceptual, providing a general understanding of the physics at play.

To simulate the formation kinetics of actin networks at this scale requires a coarse-grained representation of the actin filaments and interacting proteins. Multiple approaches have been used before, (Figure 4B-D). In the simplest beads-connected by-springs model, filaments are coarse-grained into beads that represent groups of actin subunits connected by extensile springs, incorporating the tension and bending properties (Pasquali *et al.*, 2001; Kierfeld *et al.*, 2005; Laporte *et al.*, 2012) (Figure 4D). In constrained Langevin dynamics the springs connecting filament beads are replaced by rigid rods, which speeds up computation of their motions (Nédélec and Foethke, 2007; Kurniawan *et al.*, 2012). Some models use the mechanical properties of rods to calculate the forces that result from filament stretching and bending (Head *et al.*, 2003; Kim *et al.*, 2009b; Cyron *et al.*, 2013; Dasanayake and Carlsson, 2013) (Figure 4C). In those cases where the stretching and bending elasticity can be neglected, actin filaments can be represented as rigid rods (Borukhov *et al.*, 2005; Schreiber *et al.*, 2010). Other works represented actin filaments as tubes, using a finite element approach (Heussinger *et al.*, 2007; Muller *et al.*, 2014) (Figure 4B). Finally, lattice models have also been used to study network structures (Das *et al.*, 2007; Wang and Wolynes, 2012).

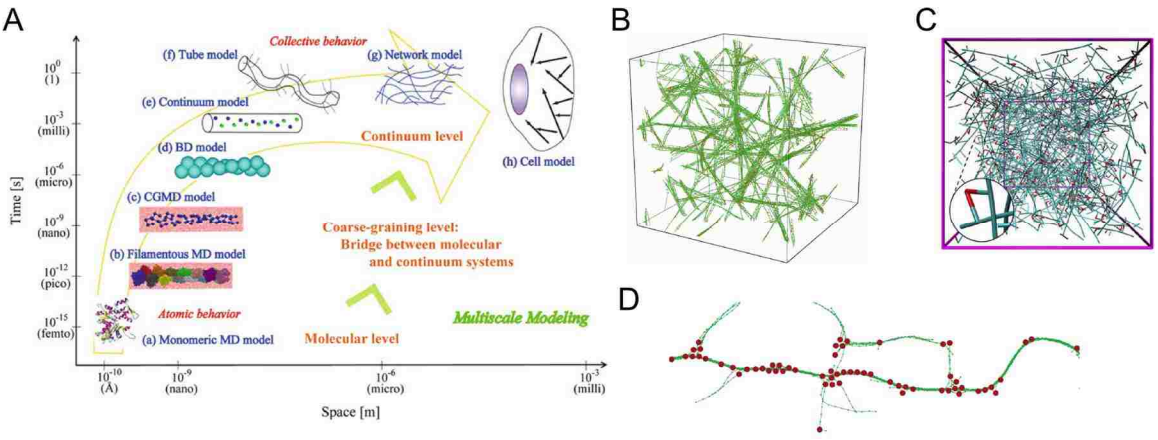

Figure 4. Temporal and spatial scales and simulation examples of the actin filament network structures. (A) Various temporal and spatial scales of actin filament structures. Molecular dynamics approach (a, b) is applied to the investigation of mechanical behaviors at the atomic scale, while continuum dynamics approach (e, f, g) is done to investigate the collective behaviors of filaments. Many coarse-grained approaches (c, d) are proposed as techniques bridging between molecular and continuum systems. (B) Example of a simulated bundle network. The simulation cube ($V = 216\ \mu m^3$) has periodic boundary conditions and 360 filaments that are in chemical equilibrium with a solution of linkers. Singly bound linkers (blue) and doubly bound linkers (red) are shown. (C) A simulated network bundled via actin crosslinking protein (ACP), consisting of actin filaments of various lengths (cyan) and ACPs (red). Two arms of each ACP drawn with partial red and cyan are connected to filaments, forming crosslinks. The inset of each plot shows the detailed geometry of bundled or crosslinked structures consisting of actin filaments and ACPs. (D) Simulation of actin filaments crosslinked by α-actinin and pulled by myosin motors, resembling a contractile ring structure (flattened in 2D). Figure panel (A) is reproduced from (Yamaoka *et al.*, 2012), (B) from (Muller *et al.*, 2014), (C) from (Kim *et al.*, 2009b), and (D) from (Laporte *et al.*, 2012).

As an example, Kim et al. (Kim *et al.*, 2009a; Kim *et al.*, 2009b) proposed an actin gel network model composed of crosslinked actin filaments. The actin filaments are polymerized out from an actin monomer pool. The motion of the coarse-grained cylindrical segments is governed by Langevin equation. The authors studied the contribution of thermal fluctuations of the network, stiffness of filaments and crosslinking to the network mechanics under shear.

Nédélec and collaborators developed a numerical model that is available as compiled software (Cytosim) to simulate the semiflexible cytoskeletal fibers (Nédélec and Foethke,

2007). In their model, fibers are simulated as linear set of points. They accounted for the bending elasticity of the fiber by applying opposite forces to the neighboring points to restore the linear line shape. They added a stochastic part to represent the Brownian motion of the fibers. The programs allows to simulate spherical structures, such as the nucleus, that is represented as a spherical set of points. The motion of such points is described by constrained Langevin dynamics to conserve certain distance in the objects. These models have been used to show that actin networks become contractile above a myosin threshold and that actin+motor systems can self-organize into various structures such as stars and bundles, similar to cell structures such as the mitotic spindle.

In my thesis work, I use computational modeling as a tool to look at the structure and dynamics of actin cables and rings in cellular systems. The wealth of previous studies, both experimental and theoretical, underlie this thesis. I'm inspired by a lot of elegant works such as those mentioned above that helped me refine the models to become more realistic and efficient. I referenced to a large number of experimental works that give me reasonable values for the parameters. And the sense of approximation and coarse-graining runs through the thesis. Mechanisms I used are mostly built on simple, yet powerful physical interactions. With these mechanisms, my models are able to reproduce actin cable and ring structures as what is observed in real-world experiments and generate similar features in different cell mutants. The models further provide quantitative insights to look at the systems. Moreover, they make some testable predictions that can be helpful for future research in biophysics and molecular biology.

Chapter 2 Semiflexible Polymer Model for Actin Filament

This chapter describes the semiflexible polymer model I built to represent the actin filament. It lays the foundation for higher order actin filament network modeling described in the following chapters 3, 4 and 5.

2.1 The Model

Actin filaments are helical polymer chains composed of actin monomers. To capture the mechanical properties of actin filaments, I used a coarse-grained bead-spring model to represent the actin filament (Figure 5), generalizing an earlier 2D model (Laporte *et al.*, 2012). In this model, a chain of beads that are connected by springs is initialized in equilibrium producing the persistence length of 10 μm. The first two segments were generated deterministically, and the rest were generated using a walk with step size 0.1 μm. The angle θ between successive tangent vectors was drawn from distribution $\sim\theta\exp\left(-\frac{\theta^2}{2\sigma_\theta{}^2}\right)$ (Smith *et al.*, 2010). The tangent correlation plot of initialization matches that predicted by theory (Figure 6A).

2.1.1 Equation of Motion

This bead-spring chain are free to move in 3D space, subject to mechanical forces (spring, bending, thermal) that maintain its shape and to additional forces from other proteins. I used Langevin dynamics (Pasquali *et al.*, 2001; Nédélec and Foethke, 2007; Kim *et al.*, 2009b) to update the bead positions $\mathbf{r}_i$ of the i^{th} bead in simulation time dt:

$$\mathbf{F}_i^{spring} + \mathbf{F}_i^{bend} + \mathbf{F}_i^{thermal} = \zeta_b \frac{d\mathbf{r}_i}{dt}, i = 1,2,..N \quad (1)$$

The different forces are described below. Spring, bending and thermal forces are intrinsic to the actin filament, describing its mechanical properties including elastic modulus, bending rigidity, persistence length and thermal fluctuation. ζ_b is an effective drag coefficient of a filament segment in cytoplasm. For simplicity, I assumed the drag coefficient to be the same for all directions and approximated it using the perpendicular translational movement (Howard, 2001; Laporte *et al.*, 2012):

$$\zeta_b = \zeta_\parallel = \zeta_\perp = \frac{4\pi\eta l_0}{\ln\left(\frac{l_0}{2a}\right) + 0.84} \quad (2)$$

In our simulations, each segment $l_0 = 0.1$ μm, representing about 37 subunits (Pollard and Earnshaw, 2004). $\eta = 350\ \eta_{\text{water}} = 0.301$ pN · s is the cytoplasmic viscosity. I used the radius of the actin filament helix cross-section $a = 3.5$ nm. Putting these together, the drag coefficient $\zeta_b = 0.216$ pN·s/μm.

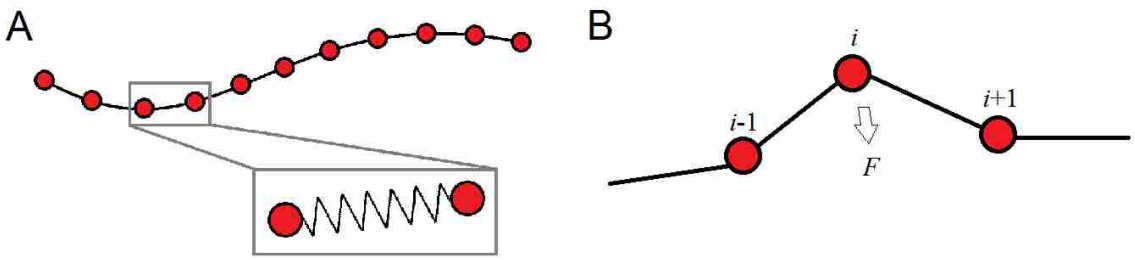

Figure 5. Spring-bead model for actin filament. Actin filament is simulated as a chain of beads connected by springs. Spring, bending and thermal forces together maintain its mechanical properties.

2.1.2 Spring force

The spring force exerted on the i^{th} bead from the neighboring two springs is calculated from the derivative of harmonic potential:

$$\mathbf{F}_i^{spring} = -\frac{\partial E^{spring}}{\partial \boldsymbol{r}_i} = -\frac{k}{2}\sum_{j=1}^{N-1}\frac{\partial\left(\left|\mathbf{r}_{j+1}-\mathbf{r}_j\right|-l_0\right)^2}{\partial \mathbf{r}_i} \tag{3}$$

where E^{spring} is the total spring energy and l_0 is the equilibrium length (0.1 μm). In vitro experiment showed that the stiffness k of a 1-μm-long actin filament is 43.7 ± 4.6 pN/nm (Kojima *et al.*, 1994). This means the stiffness of a 0.1-μm-long actin filament is about 437 pN/nm, a number ten times larger, since $= ES/l_0$, where E is the Young's modulus and S is the cross-sectional area of an actin filament. This means the actin filament is inextensible. However, I found that if we were to use a large spring constant k, we would have to decrease the simulation time step dt. Therefore, I use a much smaller $k =$

100 pN/μm in the model, a number that is enough to suppress extensile stretching while at the same time allowing us to use a larger dt so that the simulations are more efficient. In the next section, I show using this smaller spring constant the filament remains inextensible and it does not affect the mechanical properties of the filament.

2.1.3 Bending force

The bending force is calculated by measuring the local deformation of neighboring beads.

$$\mathbf{F}_i^{bend} = -\frac{\partial E^{bend}}{\partial \mathbf{r}_i} = -\frac{\kappa}{l_0}\sum_{j=1}^{N-1}\frac{\partial(\mathbf{t}_j \cdot \mathbf{t}_{j-1})}{\partial \mathbf{r}_i} \tag{4}$$

where E^{bend} is the elastic bending energy, $\mathbf{t}_i \equiv \frac{\mathbf{r}_{j+1}-\mathbf{r}_j}{|\mathbf{r}_{j+1}-\mathbf{r}_j|}$ is the local unit tangent vector, κ is the flexural rigidity, $\kappa = k_B T l_p$, where $k_B = 1.38 \times 10^{-5}$μm·pN/K is Boltzmann's constant, T is temperature (we use 300 K (Laporte *et al.*, 2012)) and l_p is the persistence length of the filament (Gittes *et al.*, 1993a). We used $l_p = 10$ μm in the simulations. Since $\frac{\partial \mathbf{t}_j}{\partial \mathbf{r}_j} = \mathbf{t}_j{}^{\mathrm{T}}\mathbf{t}_j - I_{3\times3}$ and $\frac{\partial \mathbf{t}_{j-1}}{\partial \mathbf{r}_j} = I_{3\times3} - \mathbf{t}_{j-1}{}^{\mathrm{T}}\mathbf{t}_{j-1}$, we can simplify Eq. (4) to:

$$\mathbf{F}_i^{bend} = \frac{k_B T l_p}{{l_0}^2}\left[\left(I_{3\times3} - \mathbf{t}_{i-1}{}^{\mathrm{T}}\mathbf{t}_{i-1}\right)\cdot(\mathbf{t}_{i-2} + \mathbf{t}_i) - \left(I_{3\times3} - \mathbf{t}_i{}^{\mathrm{T}}\mathbf{t}_i\right)\cdot (\mathbf{t}_{i-1} + \mathbf{t}_{i+1})\right] \tag{5}$$

In the next section, I show we can successfully generate filament with various persistence length from 2 μm to 20 μm and such property does not change with time.

2.1.4 Thermal force

The thermal force represents random fluctuating forces acting on the filament and satisfies:

$$\langle \mathbf{F}_i^{thermal} \cdot \mathbf{F}_i^{thermal^T} \rangle_{\alpha,\beta} = \frac{2k_B T \zeta_b}{\Delta t} \hat{I}_{\alpha,\beta} \quad (6)$$

where $\hat{I}_{\alpha,\beta}$ is the second-order unit tensor, and Δt is the simulation time step (Pasquali *et al.*, 2001; Nédélec and Foethke, 2007; Kim *et al.*, 2009b). I generated the random thermal forces in each coordinate basis under Gaussian distribution ~N(0, $\frac{2k_B T \zeta_b}{\Delta t}$).

2.2 Model Validation

In this section, I show how I tested the mechanical properties of individual filaments to reproduce known expressions for the tangent correlation function, relaxation dynamics and elastic energy.

2.2.1 Tangent correlation

The shape of an actin filament of length *L* can be represented by a parametric 3D curve $\boldsymbol{r}(x,t)$, where x is the contour length along the filament ($0 \leq x \leq L$) and t is the time. In thermal equilibrium we have:

$$\langle \mathbf{t}(x)\mathbf{t}(x+\Delta x) \rangle = e^{-\Delta x(D-1)/2l_p} \quad (7)$$

where $\mathbf{t}(x) = d\mathbf{r}/dx$ is the unit tangent vector along its contour, D = 3 is the dimension of free space, and l_p is the persistence length. The persistence length is given by $l_p = k_B T/\kappa$, where T is temperature and κ is the flexural rigidity of the filament,. Actin filaments in vitro have a persistence length of about 10 μm (Gittes *et al.*, 1993b), which is what we used throughout the simulations. Figure 6 shows our simulations of single filaments of constant length maintain the persistence length of filaments initialized with equilibrium configurations. Figure 6A shows that filaments can be initialized with a defined persistence length satisfying Eq. (7). Figure 6B shows that use of Langevin dynamics to evolve such filaments over times longer than the longest relaxation time τ maintains the persistence length and the shape of the tangent correlation function of Eq. (7).

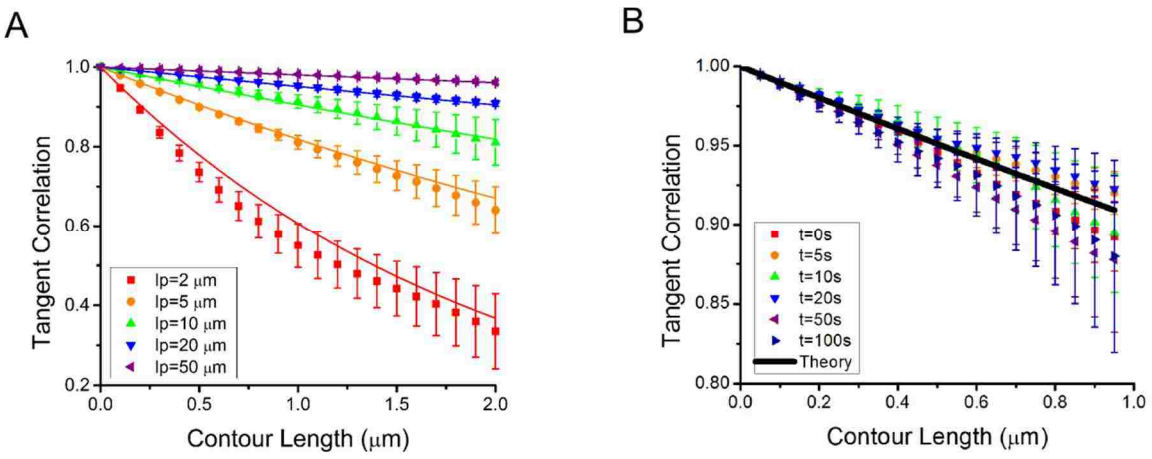

Figure 6. Validation of tangent correlation .Theoretical calculation (solid lines) is given by $e^{-\Delta x/l_p}$. Simulated filaments are initialized in equilibrium (fully relaxed). All error bars are standard error (SEM) from five simulations. (A) Comparison of tangent correlation function of initialized filaments of length 10 μm with persistence lengths l_p 2-50 μm. (B) Evolution of tangent correlation in time for an isolated 2 μm actin filament with persistence length l_p = 10 μm initialized in equilibrium.

The tangent correlation function remains unchanged from the equilibrium shape during simulations. We tested t = 0 – 100 s. The theoretical longest relaxation time is 4.5s.

2.2.2 Relaxation dynamics

In (Gittes *et al.*, 1993a), they used Fourier transformation to decompose the actin filament contour shape and analyze the relaxation time of the dynamic modes. To test that my simulations reproduce the known dynamics of single worm-like chains, I expanded the 3D filament space curve using an orthonormal set $\{Q_n(x)\}$:

$$\mathbf{r}(x,t) = \sum_n \mathbf{q}_n(t) Q_n(x), \quad n = 1,2,\ldots \tag{8}$$

where the orthonormal set is (Fujime and Maruyama, 1973):

$$Q_1(x) = \left(\frac{12}{L^3}\right)^{\frac{1}{2}} \left(\frac{L}{2} - x\right) \tag{9}$$

$$Q_n(x) = L^{-\frac{1}{2}} \Big[(\cos \alpha_n x + \cosh \alpha_n x) - \frac{\cos \alpha_n L - \cosh \alpha_n L}{\sin \alpha_n L - \sinh \alpha_n L} (\sin \alpha_n x + \sinh \alpha_n x)\Big], n \geq 2 \tag{10}$$

where L is filament length and the coefficient $\alpha_n = \left(n - \frac{1}{2}\right)\frac{\pi}{L}$. Thus vector $\mathbf{q}_n(t)$ is a complete representation of the filament shape.

For a given time difference τ, I calculated the correlation coefficient $R_{q_n}(\tau)$ (Figure 7A):

$$R_{q_n}(\tau) = \frac{\langle \mathbf{q}_n(0)\mathbf{q}_n(\tau)\rangle}{\langle \mathbf{q}_n(0)\mathbf{q}_n(0)\rangle} = \frac{\frac{1}{T-\tau}\int_0^{T-\tau} dt[\mathbf{q}_n(t) - \overline{\mathbf{q}}_n][\mathbf{q}_n(t+\tau) - \overline{\mathbf{q}}_n]}{\frac{1}{T}\int_0^T dt\,[\mathbf{q}_n(t) - \overline{\mathbf{q}}_n]^2} \quad (11)$$

where $\overline{\mathbf{q}}_n$ is the time average of $\mathbf{q}_n(t)$. From the fluctuation-dissipation theorem (Fujime and Maruyama, 1973), we also have:

$$\langle \mathbf{q}_n(0)\mathbf{q}_n(\tau)\rangle = \langle \mathbf{q}_n(0)\mathbf{q}_n(0)\rangle e^{-\tau/\tau_n} \quad (12)$$

I fitted $R_{q_n}(\tau)$ to the exponential decay $e^{-\tau/\tau_n}$ to get the simulated relaxation time τ_n for mode n (Figure 7B). I compared this value to the calculated theoretical value for τ_n (Fujime and Maruyama, 1973) (Figure 7B):

$$\tau_n = \frac{\zeta/l_0}{k_B T l_p}\frac{L^4}{(n-1/2)^4\pi^4} \quad (13)$$

where ζ/l_0 is the drag coefficient per segment length (i.e. per filament bead). In our simulations the drag coefficient per bead is the drag coefficient of a rod of segment l_0 for movement perpendicular to the rod axis, as in Eq. (2). Figure 7B shows good accordance between our simulated data and calculation from theory. I also varied the temperature T, filament segment length l_0, and persistence length l_p to find that the calculated relaxation times are all in agreement with theory (Figure 7C, D, E).

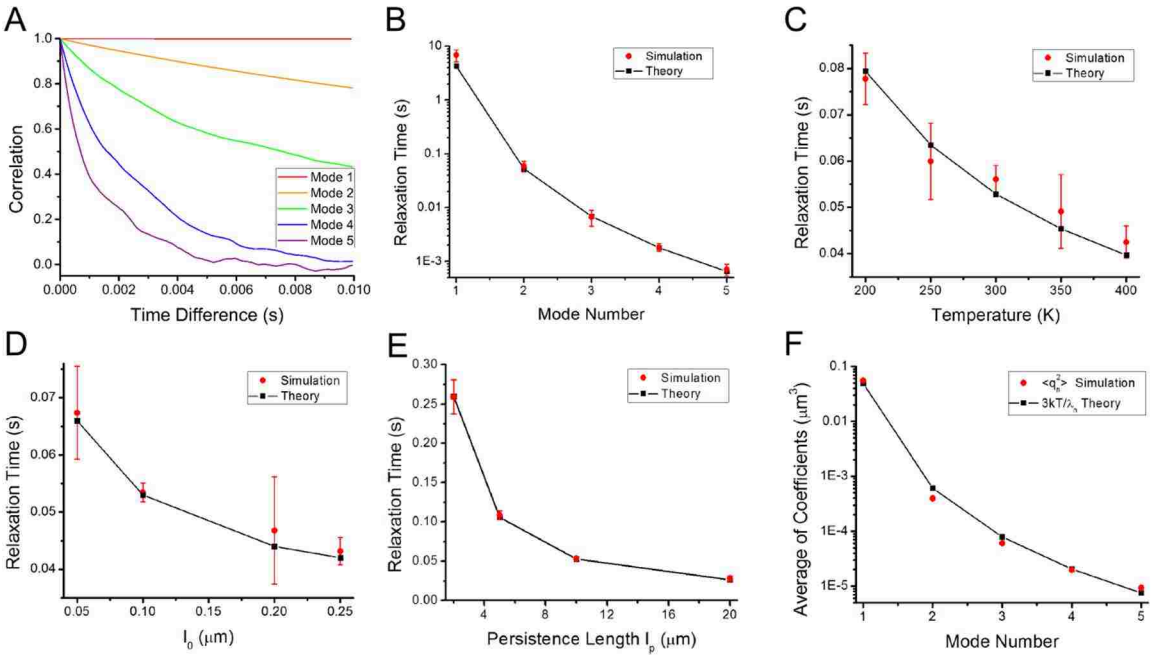

Figure 7. Validation of relaxation dynamics and energy equipartition . Simulated individual actin filament is 2 μm long with persistence length $l_p = 10\ \mu\text{m}$, $l_0 = 0.2\ \mu m$, at $T = 300\ \text{K}$ unless varied. All error bars are SEM from 5 runs. (A) The time correlation of coefficients $\{\mathrm{q}_{\boldsymbol{n}}(t)\}$ of expansion in space $\{\boldsymbol{Q}_n(x)\}$ for modes $n = 1 - 5$. (B) Relaxation time calculation from exponential fits to simulation results in panel A compared to the theoretical calculation in Eq. (13) for different modes n. (C-E) Relaxation time of mode 2 under different parameters: (C) temperature, (D) model spring equilibrium length l_0, (E) persistence length l_p. Black lines are theoretical calculations from Eq. (13). (F) Test of equipartition of energy among modes for a filament of length 1 μm. Mean value of coefficients $\langle \mathrm{q}_n{}^2 \rangle$ compared with the theoretical value in Eqs. (15) and (16).

2.2.3 Equipartition of energy

The elastic bending energy of the filament polymer chain is given by (Fujime and Maruyama, 1973):

$$\langle V \rangle = \langle \frac{1}{2} \int_0^L \left\{ \kappa \left(\frac{\partial^2 \boldsymbol{r}}{\partial x^2} \right)^2 \right\} dx \rangle = \frac{1}{2} \sum_n \lambda_n \langle \boldsymbol{q}_n(0) \boldsymbol{q}_n(0) \rangle \tag{14}$$

By equipartition theory, one has (Fujime and Maruyama, 1973):

$$\langle \boldsymbol{q}_n(0) \boldsymbol{q}_n(0) \rangle = \langle {\boldsymbol{q}_n}^2 \rangle = 3k_B T / \lambda_n \tag{15}$$

where

$$\lambda_n = \kappa [\tfrac{(n-1/2)\pi}{L}]^4, \text{ with } \kappa = k_B T l_p \tag{16}$$

Figure 7F shows a comparison of the energy per mode from theory from Eqs. (15) and (16) with the energy in our simulations calculated using Eq. (14).

Chapter 3 Modeling Actin Cables in Fission Yeast

This chapter describes the computational model I built for actin cables in fission yeast. Our collaborator Damien Laporte performed the experiments at Ohio State University. I analyzed the experimental results and compared them with the model. The work is published in the Molecular Biology of the Cell (Tang *et al.*, 2014).

3.1 Introduction

The cellular actin cytoskeleton is crucial for numerous cell functions such as cell motility, cytokinesis and cell division (Blanchoin *et al.*, 2014). Actin filaments organize into polymerizing and contractile networks and bundles with the help of nucleating, severing, side-binding and cross-linking proteins (Blanchoin *et al.*, 2014). A large body of work has studied how these molecular-level processes contribute to mesoscopic organization at the micron scale using controlled in vitro experiments with purified proteins (Gardel *et al.*, 2004; Reymann *et al.*, 2010; Alvarado *et al.*, 2013) and mathematical modeling (Kim *et al.*, 2009a; Wang and Wolynes, 2012; Cyron *et al.*, 2013). A big challenge is to develop a similar quantitative understanding of actin structures in cellular systems. Mathematical models have been very useful in providing insight on the mechanisms of cellular actin networks nucleated by the Arp2/3 complex (Carlsson *et al.*, 2010). However, very few modeling studies have examined cell structures nucleated by formin proteins, which generate bundles of antiparallel or parallel filaments (Wang and Vavylonis, 2008; Laporte *et al.*, 2012).

Budding and fission yeast cells are ideal for quantitative studies of actin organization because they are amenable to genetic modifications and microscopic imaging. Their interphase actin cytoskeleton is organized into two distinct components (Figure 8A): actin patches (nucleated by the Arp2/3 complex) and actin cables (nucleated by formins) (Drake and Vavylonis, 2010; Kovar *et al.*, 2011). The actin cables are bundles of ~10 actin filaments (Kamasaki *et al.*, 2005) that help cells establish polarized growth by providing tracks to transport secretory vesicles and organelles towards the growing part of the cell in both yeasts and plants (Vidali *et al.*, 2009; Wu *et al.*, 2010). In this work we develop a model of actin cables in fission yeast that has a simple tube-like shape and a single actin cable nucleator, formin For3. In fission yeast, actin cables growing from either tip can meet and cross-link with one another and form different morphologies depending on the cross-linking dynamics. Importantly, actin cables are critical for polarized growth, by supporting myosin cargo directional motility.

Several actin associated proteins are known to be involved in actin cable dynamics in fission yeast (Win *et al.*, 2001; Moseley and Goode, 2006; Goode and Eck, 2007; Skau and Kovar, 2010; Lo Presti *et al.*, 2012; Miao *et al.*, 2013). Formin protein For3 localizes at the cell tips and nucleates actin filaments by associating with transient cortical landmarks (Feierbach and Chang, 2001; Kovar, 2005; Martin *et al.*, 2005) . Severing protein cofilin (Cof1) binds to the sides of actin filaments (Nakano and Mabuchi, 2006; Chen and Pollard, 2011) and, with the help of Aip1 (Moseley and Goode, 2006), severs them, thus allowing constant actin turnover. Actin filament cross-linking proteins likely keep the filaments together in bundles. Cross-linking protein fimbrin Sac6 is found in

budding yeast cables (Moseley and Goode, 2006) but not fission yeast fimbrin Fim1 (Nakano *et al.*, 2001; Wu *et al.*, 2001; Skau *et al.*, 2011), likely because of its low concentration. α-actinin (Ain1) is another cross-linker in fission yeast that may contribute to actin cable bundling. Both Fim1 and Ain1 can bundle filaments in parallel or antiparallel orientations (Skau and Kovar, 2010; Skau *et al.*, 2011; Falzone *et al.*, 2012; Laporte *et al.*, 2012). Myosin V motor proteins (Myo51, Myo52), carrying secretory vesicles or anchoring on organelles, walk along actin filament towards the barbed end (Lo Presti *et al.*, 2012). Some of these myosin V molecules associate with the cortical endoplasmic reticulum that is tightly attached to the plasma membrane while the two heads remain bound to actin cables (Zhang *et al.*, 2012).

Here we develop a 3D coarse-grained computational model to explore how the above molecular mechanisms contribute to the large scale actin cable organization in Figure 8A. We address the following questions: (*i*) Can a model that uses simple mechanisms such as polymerization, severing and cross-linking explain important features of actin cables such as their thickness and network topology? (*ii*) How is cable organization related to how motor proteins like myosin V anchor on cargos or endoplasmic reticulum? (*iii*) How do formin clustering, cross-linker strength and concentration influence actin cable structure, orientation, dynamics and polarity?

We use the model to quantify actin cable distributions and predict the effects of myosin V pulling, cross-linker concentration and strength, and formin clustering at cell tips. The model reproduces prior experimental results in *myoVΔ* fission yeast cells where actin cables curl up close to the tips and fail to span the entire cell (Lo Presti *et al.*, 2012). We

predict that overexpression of myosin V may result in unbundling of actin cables into individual stretched filaments. We show that increasing concentration and strength of cross-linkers, as well as increased clustering of formin nucleation sites, promotes actin filament bundling. At the high cross-linking strength regime, actin filaments get cross-linked in mostly parallel orientations while anti-parallel bundles bulge or break up. Analysis of experiments of cells overexpressing Ain1 supports these predictions. Our work provides a framework for further quantitative understanding of actin structures in cellular systems.

3.2 Model, Methods and Materials

3.2.1 Actin filament model

We used the bead-spring model to represent the semiflexible actin filament chain. For details, refer to previous chapter.

We use Langevin dynamics to update the positions $\mathbf{r}_i$ of the i^{th} filament bead in simulation time dt (Figure 8B):

$$\mathbf{F}_i^{spring} + \mathbf{F}_i^{bend} + \mathbf{F}_i^{thermal} + \mathbf{F}_i^{crslnk} + \mathbf{F}_i^{myo} = \zeta_b d\mathbf{r}_i/dt, \qquad (17)$$

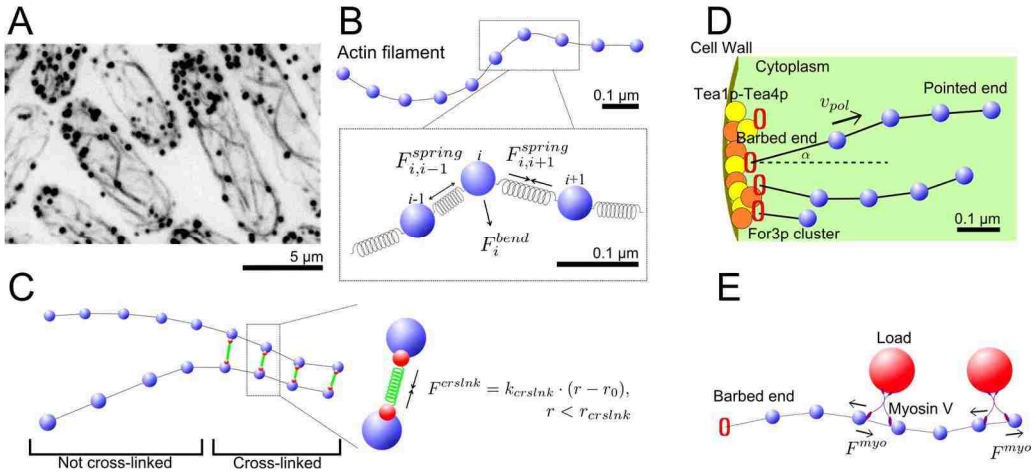

Figure 8. Model mechanism. (A) Images of actin cables in fission yeast (inverted black and white). GFP-CHD tagged actin showing structures of actin cables (black lines) and actin patches (black dots). (B) A single actin filament is described by bead-spring model. (C) The effect of cross-linking proteins that link neighboring actin filaments into bundles is represented as finite-range spring interactions. (D) Tea1/Tea4 landmark proteins at the cell tip recruit For3 molecules to form clusters, which polymerize actin subunits into actin filaments. This is represented by growth of semiflexible polymers from fixed positions at cell tips. (E) Myosin V pulls actin filaments by carrying or anchoring on heavy loads. This is represented by tangential forces along actin filaments.

Myosin V (Myo51 and Myo52) that carries secretory vesicles or anchors on stationary organelles can exert a stochastic force on the actin cables when walking towards the barbed end (Grallert *et al.*, 2007; Clayton *et al.*, 2010; Lo Presti *et al.*, 2012; Zhang *et al.*, 2012). Myosin V clusters move along cables with speeds 0.5-2.5 μm/s over a few μm (Grallert *et al.*, 2007; Clayton *et al.*, 2010). We simulate the effects of myosin V on cables as a transient tangential force applied on the filament, towards the barbed end (Figure 8E). We assume 0.5 pN force per myosin V (Mehta *et al.*, 1999) and 5 s

association time and vary the linear density of motors along the filament to observe the effects of myosin V pulling.

3.2.2 Polymerization

Formin-mediated polymerization of actin filaments is simulated as elongation of the first segment of the semi-flexible chain at a fixed angle from a few cortical sites at the cell tips (Figure 8D, Table 1). These sites represent For3 bound to Tea1-Tea4 clusters (Martin *et al.*, 2005). We assume a constant total number of formin dimers at the cell tips (72 at each end). These formins are distributed into $N_{cluster}$ clusters. Each cluster contains $72/N_{cluster}$ formin dimers. Changing $N_{cluster}$ we are able to evaluate the clustering effect of the formins. The clusters are chosen to be randomly distributed on the cell tip surfaces. Formins within the same cortical site are distributed randomly over a small area around the center of the site. Polymerization of filaments is simulated as elongation of the segments attached to the formin nucleation sites. We use a polymerization rate v_p = 0.3 μm/s (Lo Presti *et al.*, 2012). If the elongating segment reaches twice the size of spring equilibrium length l_0, a new bead is added to the middle of the segment.

3.2.3 Cross-linking

Cross-linking is simulated as attraction between beads that come close to one another. The cross-linking force, $\mathbf{F}_i^{crslnk}$, when bead i is within r_{crslnk} of bead j (belonging to the same or different filament) is defined as:

$$\mathbf{F}_i^{crslnk} = -\frac{k_{crslnk}}{2}\sum_j \frac{\partial(|\mathbf{r}_i-\mathbf{r}_j|-r_0)^2}{\partial \mathbf{r}_i}, \qquad \text{for } |\mathbf{r}_i - \mathbf{r}_j| \le r_{crslnk}, \tag{18}$$

where the interaction range r_{crslnk} and interaction spring constant k_{crslnk} are varied in the simulations. r_{crslnk} and k_{crslnk} characterize the binding/unbinding kinetics of the cross-linkers and their concentration. We use $r_0 = 0.03$ μm as the equilibrium distance between the two cross-linked filament beads, which represents an effective distance between two actin segments cross-linked by cross-linkers such as α–actinin or fimbrin (Klein *et al.*, 2004; Sjoblom *et al.*, 2008).

3.2.4 Filament turnover

We do not explicitly simulate the dissociation and recycling of formin For3 at the tips that has been previously studied (Wang and Vavylonis, 2008). Both For3 dissociation from cell tips and cofilin severing contribute to actin filament turnover. Since the precise mechanism is unknown, we employ a simplified mechanism for filament turnover: we remove whole filaments with a rate that gives an average filament lifetime 15s (Vavylonis *et al.*, 2008). In the simulation, filaments are tested for removal every 0.001 s. Other than cofilin, For3 dissociation from cell tips may also contribute to actin filament turnover (Wang and Vavylonis, 2008).

3.2.5 Fission yeast shape

Fission yeast during G2 phase has a rod-like shape with a diameter of 3 to 4 μm and a length of 7 to 12 μm. In our simulations, we use a cylinder capped by two hemispheres

(tips), with a diameter of 3.6 μm and length of 9 μm (end to end) to represent the shape. We simulate the boundary as a hard wall by a large repelling force applied to filament beads crossing the cell boundary.

3.2.6 Excluded volume

Excluded volume by the larger organelles such as the vacuoles and the nucleus is simulated by immobile spheres that prevent actin filaments from going through them. We used 2.4 μm as the diameter of the nucleus at the center. The vacuoles are simulated as spheres randomly distributed in the remaining volume. The volume fraction occupied by the spheres (excluding nucleus) is 17.14%, consistent with the 10%-20% measurements in (Milo, 2013). We note that the vacuole volume can drastically change in different medium or under osmotic pressure (Bone *et al.*, 1998). The diameter of the spheres is 0.8 μm, based on electron tomography (Hoog *et al.*, 2007), giving a total number of 40. This is bigger than 0.4 μm reported in (Bone *et al.*, 1998; Mulvihill *et al.*, 2001) and the number of spheres 40 is smaller than the number of vacuoles counted in (Bone *et al.*, 1998; Mulvihill *et al.*, 2001).

3.2.7 Myosin pulling

We assume 0.5 pN force per myosin V (Mehta *et al.*, 1999) and 5 s association time. We vary the density of motors per μm, ρ_{myo}, along the filament to observe the effects of myosin V pulling under different myosin V concentrations. We simulate the effects of

attached myosin V on the i^{th} bead of a filament as a transient tangential force towards the barbed end:

$$\mathbf{F}_i^{myo} = -F_{myo}\,\mathbf{t}_{i-1} \tag{19}$$

3.2.8 Distribution of cortical sites and For3 dimers within cortical sites

The cortical cluster sites are randomly distributed on the semi-spherical cell tips. Formin For3 dimers are found distributed in landmark protein clusters on the tips (Martin and Chang, 2006). In our simulations, formin dimers within the same cortical site are distributed randomly within a small area. For 6 formin dimers per cluster, the diameter of the cortical site is 0.1 μm.

3.2.9 Strains, growing conditions, and cellular methods

(Laporte) The *S. pombe* strains used in this study are JW1349-2 (41nmt1-GFP-CHD (rng2)-leu1+ rlc1-tdTomato-natMX6 ade6-M210 leu1-32 ura4-D18) and JW3764 (kanMX6-3nmt1-ain1 41nmt1-GFP-CHD (rng2)-leu1+ rlc1-tdTomato-natMX6 ade6-M210 leu1-32 ura4-D18). In JW3764, AIN1 was under the control 3nmt1 promoters integrated at its native chromosomal loci (Bähler *et al.*, 1998). To induce nmt1 promoters, cells were first grown at 25°C in YE5S medium for 24 h at exponential phase, washed four times in EMM5S medium, and then grown for 18h in EMM5S before microscopy.

3.2.10 Microscopy and data analysis

(Laporte) Live cell microscopy was performed as described previously (Laporte *et al.*, 2013) at 24‑25°C, using a thin layer of EMM5S liquid medium with 20% gelatin (Sigma-Aldrich) and 0.1 mM n‑propyl‑gallate. For imaging, we used a 100×/1.4 NA Plan-Apo Nikon objective lens on a spinning disk confocal microscope (UltraVIEW ERS; Perkin Elmer Life and Analytical Sciences, Waltham, MA) with 440-, 488-, 514-, and 568-nm lasers and an ORCA-AG camera (Hamamatsu, Bridgewater, NJ). No binning was used for strains expressing GFP-CHD. Images were analyzed using ImageJ (http://rsb.info.nih.gov/ij/). Images in figures are maximum-intensity projections of z sections spaced at 0.2–0.4 µm.

3.2.11 Experiments with drugs

(Laporte) For CK-666 treatment, exponential growing cells were washed in EMM5S with 0.1 mM n‑propyl‑gallate and preincubated with 100 µM Arp2/3 inhibitor CK-666 (Chemdiv, San Diego, CA; (Nolen *et al.*, 2009)) for 5 min to reduce the interference of actin patches for analysis. Then, cells were imaged immediately on bare slides where the start of the observation is defined as time 0. GFP-CHD images were collected in 8-s intervals for wild type strain and 10-s intervals for overexpressing Ain1 strain over 10 min.

3.3 Results

Simulation results using the parameter set in Table 1 reproduce actin cable structures similar to those observed in cells. Figure 9A shows simulations of actin filaments that grow out of 12 cortical sites per tip, with blue and red colors marking filaments that grow from either tip. After 180 s, which is long enough to reach steady state, the filaments organize into a few bundles that contain filaments in both parallel and antiparallel orientation (Figure 9B). Filaments grow through the gaps among vacuoles and the nucleus, reaching filaments that polymerize from the opposite tip, generating bundles that span the cell length as in experimental images (Figure 8A).

Table 1. Model parameters for fission yeast actin cables.

Parameter	Description	Value	Unit
N	Number of the formins at one tip (total 2N)	72	
$N_{cluster}$	Number of clusters at one tip	12, 4→72	
$\rho_{cluster}$	Cluster density, $\rho_{cluster}= N/N_{cluster}$	6, 1→18	
D_{yeast}	Diameter of yeast cell	3.6	μm
L_{yeast}	Length of yeast cell	9	μm
N_{vac}	Number of vacuoles	40	
D_{vac}	Diameter of vacuole	0.8	μm
D_{nuc}	Diameter of nucleus	2.4	μm
v_{pol}	Polymerization rate (barbed end growth)	0.3	μm/s
$v_{pointed}$	Pointed end growth/shrinking rate	0	μm/s
τ_{sever}	Average turnover time	15	s
l_{sever}	Severing characteristic length, $l_{sever}= v_{pol}\ \tau_{sever}$	4.5	μm
T	Temperature	300	K
l_p	Persistence length of actin filaments	10	μm
κ	Flexural rigidity, $\kappa = k_BT\ l_p$	0.0414	pN·μm^2
l_0	Filament model segment length	0.1	μm
k	Spring constant	100	pN/μm
η	Cytoplasmic viscosity (350 times larger than water)	0.301	pN/μm^2·s
k_{crslnk}	Cross-linking spring constant	2, 0→15	pN/ μm
r_0	Cross-linking gap distance	0.03	μm
r_{crslnk}	Cross-linking interaction range	0.09, 0→0.16	μm
F_{myo}	Myosin walking force	0.5	pN
ρ_{myo}	Myosin linear density along filament	1, 0→10	#/μm

λ_{myo}	Myosin force density, $\lambda_{myo}= F_{myo}* \rho_{myo}$	0.5, 0.5→5	pN/μm
τ_{myo}	Myosin V lifetime on actin filament	5	s

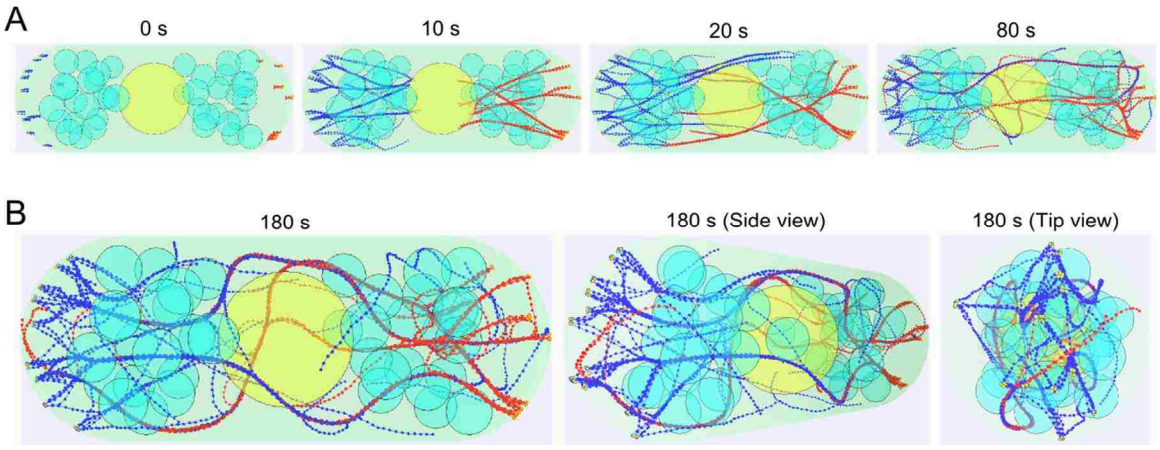

Figure 9. Simulated actin cables using parameter values from Table 1.(A) Time evolution of the simulation. Nucleus (yellow) and vacuoles/organelles (cyan) are simulated as impenetrable immobile spheres. The cytoplasmic region is marked in light green. Actin filaments growing from the left (right) side tip are marked in blue (red). Formin For3 clusters localized at the cell tip are marked in orange. (B) Simulated steady state actin cables viewed from different perspectives (front, 45°, and 90°) showing a complete 3D cable structure.

3.3.1 Myosin V pulling impact on cable distribution

Prior experiments show that deletion of both copies of myosin V, Myo51 and Myo52, leads to short, curved, and misoriented cables in interphase fission yeast cells (Lo Presti *et al.*, 2012) (Figure 10A). By eliminating the simulated Myosin V pulling, actin filaments converge into thicker and less straight bundles near the cell tips that do not span the entire cell, in agreement with experimental observations (Figure 10B). Simulations predict that excessive myosin V pulling unbundles the cables (Figure 10B): as the number of myosin V per unit length along the filament, ρ_{myo}, increases from 0 to 10/μm,

the percentage of bundled actin filaments decreases from 75% to 58% (Figure 10C). Increase in ρ_{myo} also leads to a more uniform distribution of filaments across the cell (Figure 10D, Figure 11D). Enhanced myosin pulling affects the number of filaments in the largest linked cable, increases the total number of cables, and straightens them (Figure 11, A-C). This highlights the critical role of motors in actin cable organization.

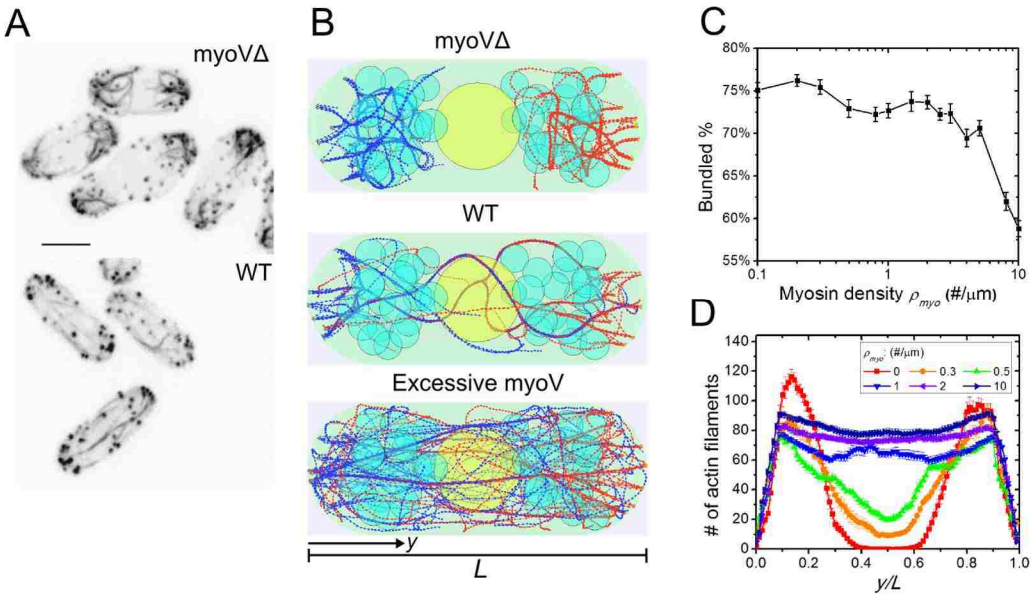

Figure 10 Simulations of myosin V force straightening actin cables .(A) Experimental figures of actin cables in *myoV*Δ cells where >95% of the cells showed misoriented and thick cables and >70% of the cells showed an extension defect, reproduced with permission from (19). (B) Simulated steady state configurations of myosin density ρ_{myo} = 0, 1, and 10 μm^{-1}, showing misoriented cables at the tip, normal actin cables or straightened but thin actin cables. (C) Bundled actin filament percentage as a function of myosin V density ρ_{myo}. Fewer actin filaments are bundled for high ρ_{myo}. (D) Graph of actin filament bead concentration along the long axis of the cell (average of 3 cells). More actin filaments are able to span the cell as ρ_{myo} increases.

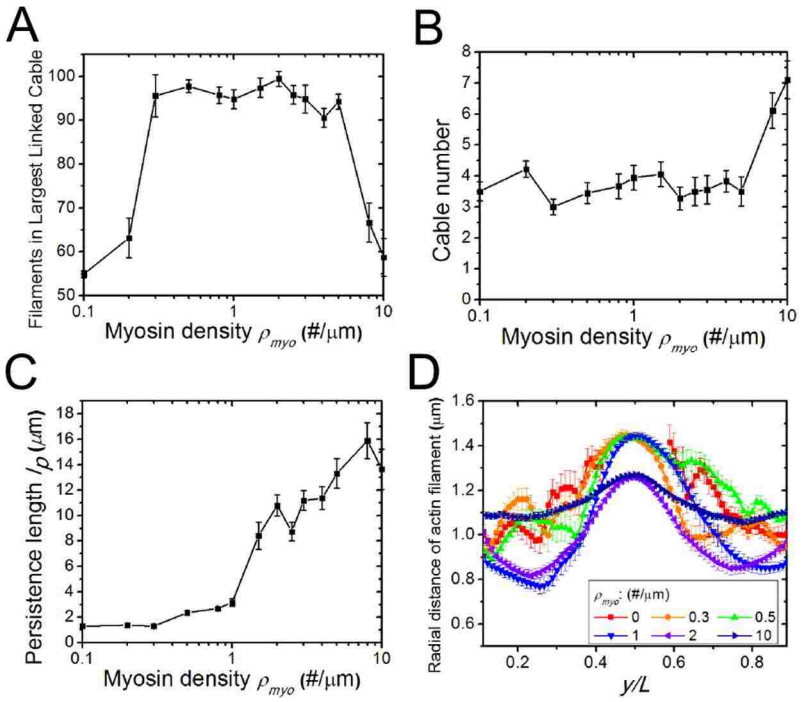

Figure 11. Myosin V walking along actin filaments influences cable thickness and stiffness. All parameters other than ρ_{myo} are given in Table 1. Error bars are SEM from 5 runs. (A) Thickest cable size as a function of ρ_{myo}. At low ρ_{myo}, actin filaments are not able to span the whole cell and form a connected structure near cell tips that contains ~55 filaments. At intermediate ρ_{myo} the filaments extend through the middle and can form a connected structure that contains ~ 95 filaments. At the highest ρ_{myo}, myosin pulling unbundles the filaments, resulting in smaller values for the thickest cable size. (B) Cable number as a function of ρ_{myo}. The total number of cables increases about 2-folds as ρ_{myo} increases. (C) Effective cable persistence length as a function of ρ_{myo}. The effective persistence length is the average persistence length of the filaments in the simulation, excluding filament segments within the semispherical cell tips. The persistence length grows from ~1.5 μm to more than 12 μm as myosin V density increases, suggesting a straightening effect due to pulling. (D) Graph of average radial distance of actin filaments along the long axis of the cell, y/L. At high ρ_{myo}, straightened actin cables are stretched closer to the nucleus.

3.3.2 Cross-linking strength and dynamics influence cable morphology

In our simulations, the kinetics of cross-link formation and breakage are described by two parameters: cross-linking range $r_{crslnk,}$ and spring constant k_{crslnk}, which determines the depth of the interaction potential between cross-linked filament beads (for given r_{crslnk}). These parameters determine the rates of cross-link formation / breakage and reflect the type and concentration of cross-linker proteins in cells, with larger values representing stronger cross-linking. The simulated actin cable configurations at steady state vary depending on the values of r_{crslnk} and k_{crslnk} (Figure 12A). We found that larger r_{crslnk} and k_{crslnk} promote actin filament bundling (Figure 12B). At k_{crslnk} = 2 pN/μm, the standard parameter, the actin filament bundled percentage increases from 2% to 77% as r_{crslnk} changes from 0.06 μm to 0.11 μm (Figure 12B). Conversely, the bundled percentage increases from 4% to 74% as k_{crslnk} increases from 0.1 pN/μm to 5.0 pN/μm when r_{crslnk} = 0.09 μm (Figure 12B). Similar trends to Figure 12B are observed when measuring the number of filaments in the largest linked cable (Figure 13A). Moreover, we show that r_{crslnk} and k_{crslnk} together regulate the number of cables (Figure 12C). For a given r_{crslnk} there exists a k^*_{crslnk} value giving maximum number of cables (the cables at the peak value have average 3-6 filaments each, see Figure 13B). For values of k_{crslnk} below k^*_{crslnk} the system has mostly unbundled filaments so the number of cables increases with increasing r_{crslnk}. For $k_{crslnk} > k^*_{crslnk}$ most filaments become bundled. In this range the dependence of the number of cables on k_{crslnk} and r_{crslnk} is weak, reflecting the maximum filament bundling that can be achieved within the filament turnover time with the given geometry and polymerization rate.

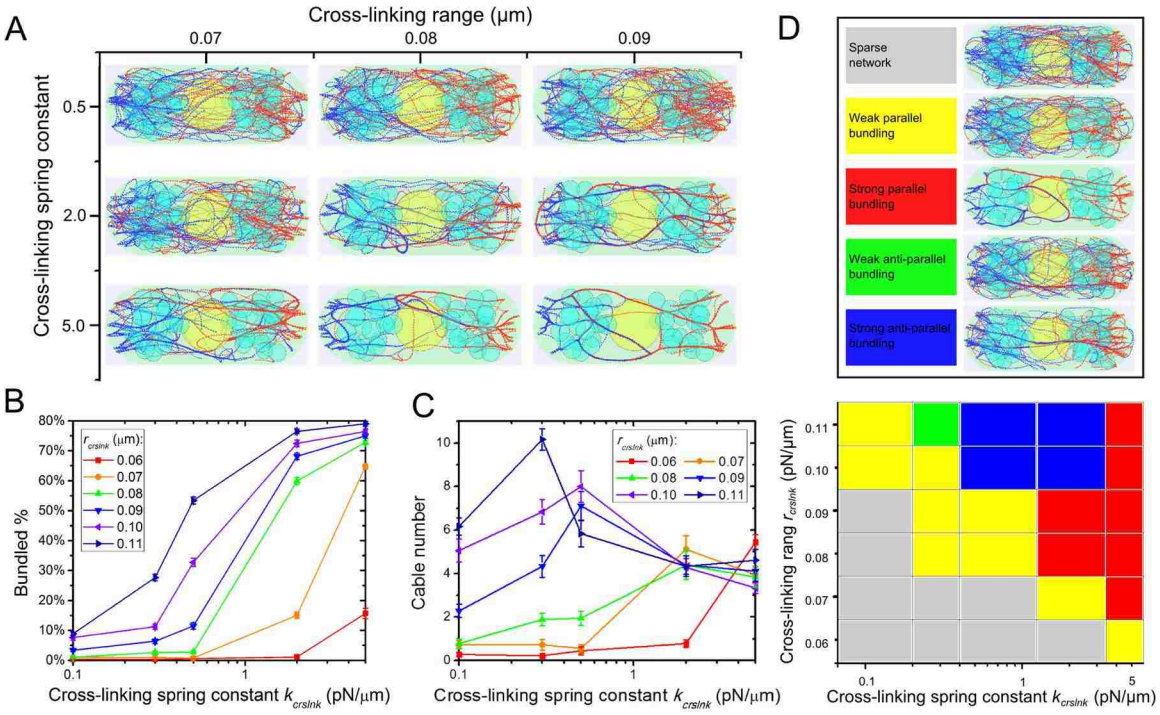

Figure 12. Stronger cross-linking interactions promote actin cable formation in simulations. (A) Steady state configurations under different cross-linking spring constants (k_{crslnk}) and cross-linking interaction ranges (r_{crslnk}). (B) Bundled actin filament percentage increases with increasing rcrslnk and kcrslnk. (C) Cable number as a function of r_{crslnk} and k_{crslnk}. (D) Polarity of actin filaments in cables varies with cross-linking parameters. In “weak” regions most actin filaments are unbundled. In “strong” regions most filaments are bundled in either primarily parallel or anti-parallel orientations. Anti-parallel orientations occur due to bundling of filaments that grow from different cell tips.

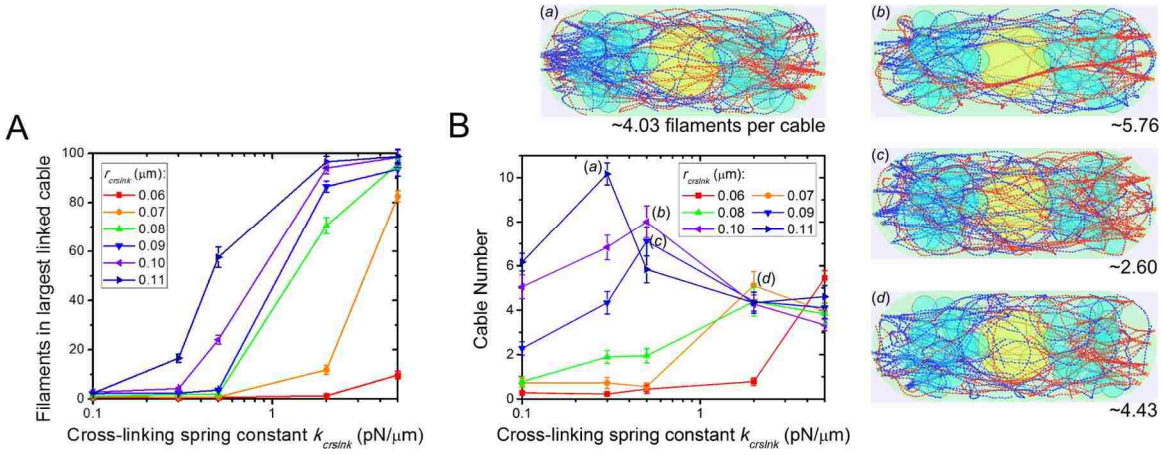

Figure 13. Modifying crosslinking parameters affects actin cable thickness and number. All error bars are SEM from 5 runs. (A) Number of filaments in the thickest cable as a function of k_{crslnk} under different rcrslnk. Increasing r_{crslnk} and k_{crslnk} leads to thicker cables. (B) Cable number as a function of kcrslnk and rcrslnk. As k_{crslnk} increases from 0.1 pN/μm, it first causes unbundled filaments to come together in bundles. Further increase causes the bundles to merge into fewer but thicker cables. (a)-(d) Snapshots of simulations at peak positions in the graph.

3.3.3 Polarity of filaments in simulated actin cables

Another feature of actin cables that changes with cross-linker parameters is the orientation of filaments within the cables, which is critical for cargo transport along cables. By measuring the filament orientation and degree of bundling as function of k_{crslnk} and r_{crslnk}, we find different regimes in parameter-space (Figure 12D) that include "weak" parallel and antiparallel regimes when less than 30% of the filaments are bundled and "strong" parallel and antiparallel regimes when more than 30% are bundled.

Figure 14A shows enlarged snapshots of cells at steady state in the strong anti-parallel (left panel) and strong parallel (right panel) regimes. In the standard condition (k_{crslnk} = 2

pN/μm), actin filaments that grow out of the opposite tips form mostly cables with anti-parallel filaments (solid arrowheads) and a few with parallel filaments (hollow arrowheads). In this condition, cross-linking is sufficiently weak to allow filaments polymerizing from opposite tips to slide past one another when they meet by end-to-end encounter or by lateral fluctuations, leading to steady cables with minor undulations (Figure 14B and C). In the high cross linking condition (k_{crslnk} = 5 pN/μm), we find mostly cables with parallel filaments and only few with anti-parallel filaments. In this condition, cross-links are long-lived, which induces buckling and bulging of filaments that meet by end-to-end encounter or lateral fluctuations (Figure 14B and C). This results in formation of junctions at which filaments change direction to bundle in parallel (Figure 14A(*c*)(*d*)(*e*)). The outcome of end-to-end encounters also depends on the angle of encounter, with a higher probability of parallel bundle formation for larger angle, similar to prior in vitro experiments (Reymann *et al.*, 2010). These results further highlight how cross-linking dynamics combine with actin filament mechanics and nucleation geometry to regulate polarity of actin filaments in bundles (Reymann *et al.*, 2010).

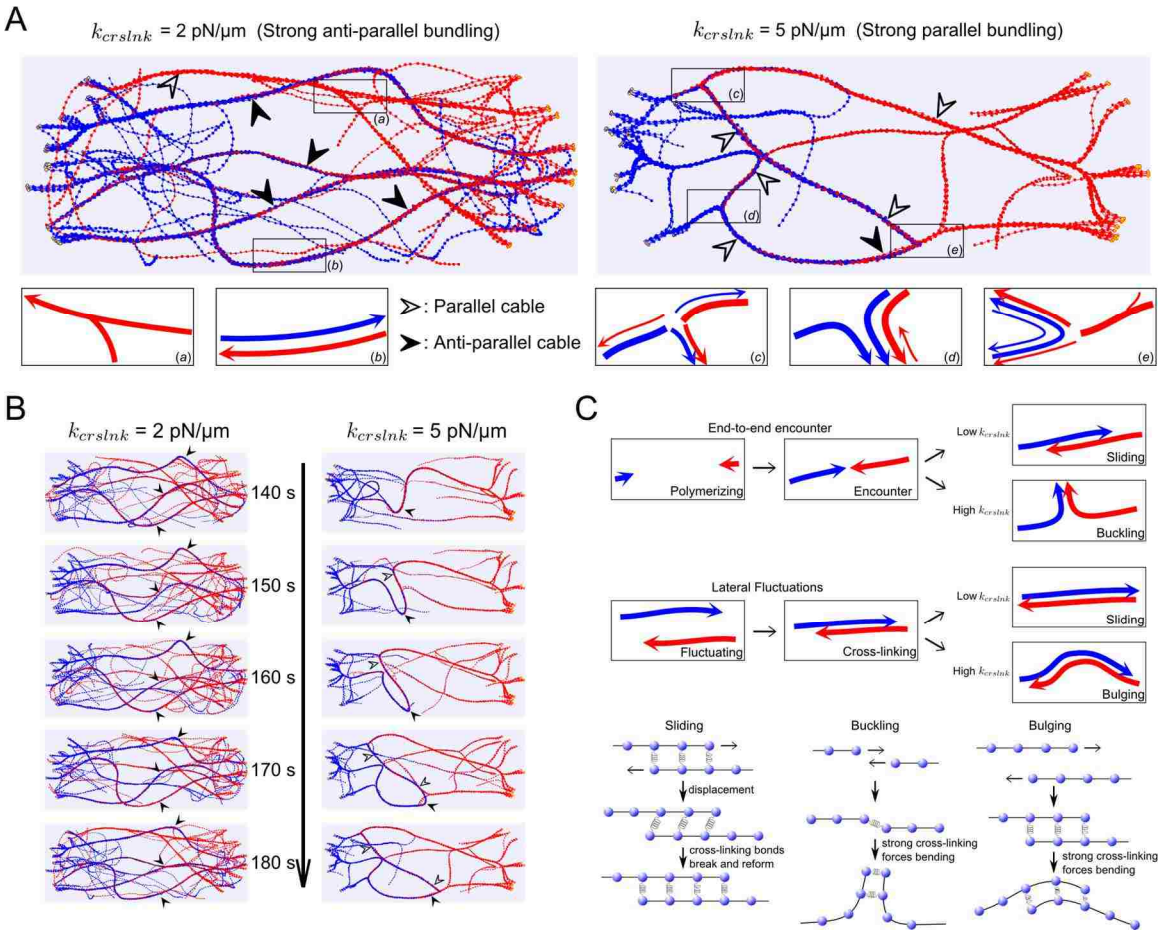

Figure 14. Cross-linking strength and dynamics influences the dynamics of actin cables. (A) Actin cable structures with cross-linking spring constant k_{crslnk} = 2 pN/μm (corresponding to the strong parallel case of Figure 4), compared with k_{crslnk} = 5 pN/μm (strong parallel case in Figure 4). Solid arrows point to anti-parallel cables (blue and red filaments, the barbed end of which is towards opposite directions). Hollow arrows point to parallel cables. (B) Time evolution of actin cable structures under high k_{crslnk} = 5pN/μm in comparison with 2 pN/μm. For high k_{crslnk}, anti-parallel cables are not stable: the cables bulge and sometimes even break to form parallel cables while for low k_{crslnk}, anti-parallel cables remain stable. (C) Schematic representation of sliding, buckling and bulging mechanisms. In the low k_{crslnk} case, filaments can slide through each other as they polymerize to form anti-parallel bundles. In the high k_{crslnk} case, cross-linking forces overcome mechanical forces to bend the cables, resulting in buckling and bulging and formation of mostly

parallel bundles. The outcome of an encounter also depends on the angle of encounter and the thickness of the bundles.

3.3.4 Overexpression of α-actinin changes actin cable morphology

To further investigate the predicted effect of cross-linkers, we analyzed actin cables in wild-type cells and cells over-expressing α-actinin, using the *3nmt1Ain1* promoter (Figure 18A). We chose α-actinin since the effect of overexpression of the other cross-linker in fission yeast, fimbrin, is very drastic with overexpression mutants having significantly modified cable morphologies (Wu *et al.*, 2001; Laporte *et al.*, 2012; Burke *et al.*, 2014) (see also Discussion). To better visualize actin cables we also treated cells with CK666, an inhibitor of the Arp2/3 complex that depolymerizes actin patches (Nolen *et al.*, 2009). This treatment causes an increase in the amount of actin in the cables, which also become longer and more curved (Burke *et al.*, 2014). Treatment by CK666 may also release fimbrin from actin patches, resulting in an increase in cable cross-linking (Burke *et al.*, 2014).

First we compared changes in cable numbers. Since cables do not have a clear beginning and end in either experiment or simulations, we counted the minimum number of distinct continuous cable segments that are required to generate the observed network structure in maximum intensity projections. While some statistically-significant differences were observed, there was no big variation in average cable number among the four experiments (Figure 18B). The resulting cable number is of the same order as in simulations of the strong bundling cases (parallel and anti-parallel) in Figure 12D. The

weak dependence on cross-linker concentration is also consistent with the weak dependence of cable number on cross-linking parameters within the strong bundled regimes described in our model (Figure 12C and Figure 13B).

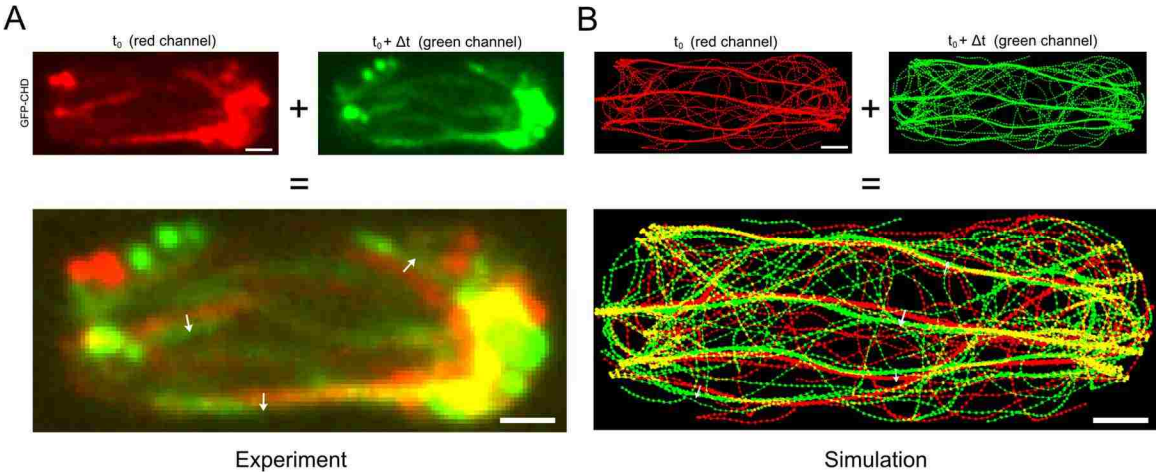

Figure 15. Measurement of lateral movement of actin cables in experiments and simulations. Red channel shows actin cables at time t_0 and green channel shows actin cables one frame later at $t_0+\Delta t$ of (A) GFP-CHD labeled actin filaments in experiments and (B) simulations. The two channels are merged to show the lateral movement per frame, which is calculated as the perpendicular displacement from the center of the red cable to the center of the green cable (arrows). If the cable remains stationary, the merged frame will show yellow, which is also counted. Scale bar: 1μm.

Second, we measured the lateral movement of the cables in time-lapse movies (see method in Figure 15) and found that the average movement ranges from 0.24 to 0.28 μm in 8 s (WT) or 10 s (other cases) (Figure 18C). Simulations predict the average movement ranges from 0.17 μm to 0.3 μm per 10 s for parameter values in the strong anti-parallel

and strong parallel regimes, respectively (Figure 16B). These numbers are similar in magnitude to the experimental data (see also Discussion).

A more sensitive measure of a shift of the system through the strong parallel and strong anti-parallel regions is a change in cable curvature and formation of loops and curved structures with junctions (Figure 12D, Figure 16A). Thus, we also quantified the curvature distribution of the cables. We categorized the morphology into four types (Figure 18D and Figure 17). Actin cables are more curved in the Ain1 overexpression mutants compared to WT, for both untreated and CK666-treated cells. There are also more loop occurrences in untreated *3nmt1Ain1* cells compared to WT (53% vs. 3%, Figure 18E). Interestingly, loops occur in more than 80% of WT and *3nmt1Ain1* cells in CK666 and remain stable for at least 80 sec. By contrast, in untreated cells, loops only last 20-30 sec.

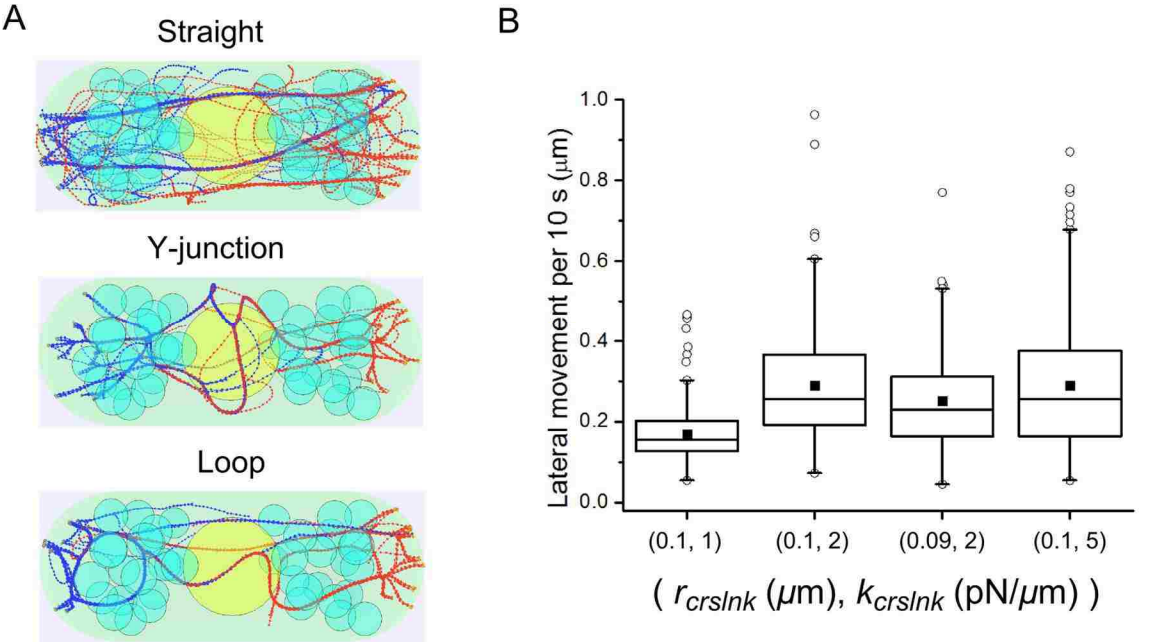

Figure 16. Examples of cable features and lateral movement in simulations. (A) Examples of simulated actin cables showing features: straight, Y-junctions and loops. (Top: r_{crslnk} = 0.1 μm, k_{crslnk} = 1.0 pN/μm; Middle and Bottom panel: r_{crslnk} = 0.1 μm, k_{crslnk} = 5.0 pN/μm). Y-junctions and loops are typical features of high k_{crslnk} cases where parallel cables are preferred and anti-parallel cables bulge and break. (B) Lateral movement of cables is measured upon varying (r_{crslnk}, k_{crslnk}), with values corresponding to the symbols shown in Figure 6F. Dots in graph indicate average values; boxes contain 50% of data; whiskers: 1.5 interquartile range.

The experimental results of Figure 18D and E are in agreement with simulations where we commonly see loops in the high cross-linking regimes where cables tend to bundle in parallel, generating junctions and loops. Figure 18F shows the predominant simulated actin cable curvature as function of r_{crslnk} and k_{crslnk}. The symbols in Figure 18F suggest a possible mapping of the model to experiment. The distribution of actin cable curvature at these points matches the experimental curvature distribution (Figure 18D,G). We also looked at loop occurrences in simulations (Figure 18H). Loops are present for high r_{crslnk} and k_{crslnk} and remain stable for at least 60 sec, a trend that qualitatively agrees with experimental observations in Figure 18E. Overall, our analysis supports that WT cells are near the boundary of the model's strong parallel and strong anti-parallel regimes and that Ain1 overexpression and CK666 treatment both push the system towards the strong parallel regime.

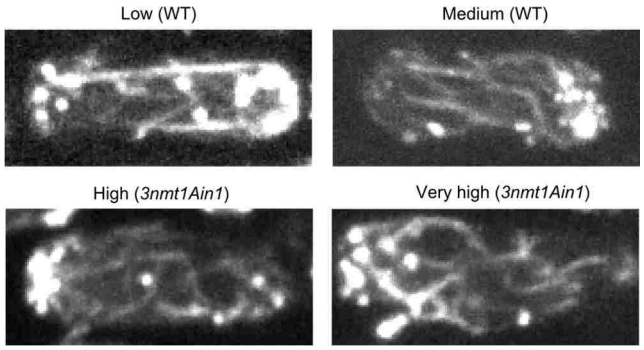

Figure 17. Evaluation of curvature distribution of actin cables. For every point along the contour of cables, we define the curvature κ to be: $\kappa = \left\|\frac{dt}{ds}\right\| = \frac{1}{R}$, where ***t*** is the unit tangent vector, *s* is arc length and *R* is the radius of the circle of curvature. Low: cables are straight and have small curvature (0 → 1/5 μm^{-1}), example from WT. Medium: cables with higher average curvature (1/5 → 1/3 μm^{-1}), WT. High: cables are curved, curvature distribution has values (1/3 → 1/1.5 μm^{-1}), *3nmtAin1* cells. Very high: curvatures have values larger than 1/1.5 μm^{-1}. Most cables are highly curved in *3nmtAin1* mutants. In the simulations of Figure 18F, curvature was calculated as in experimental images, using images of cells obtained after 140 s of simulation time.

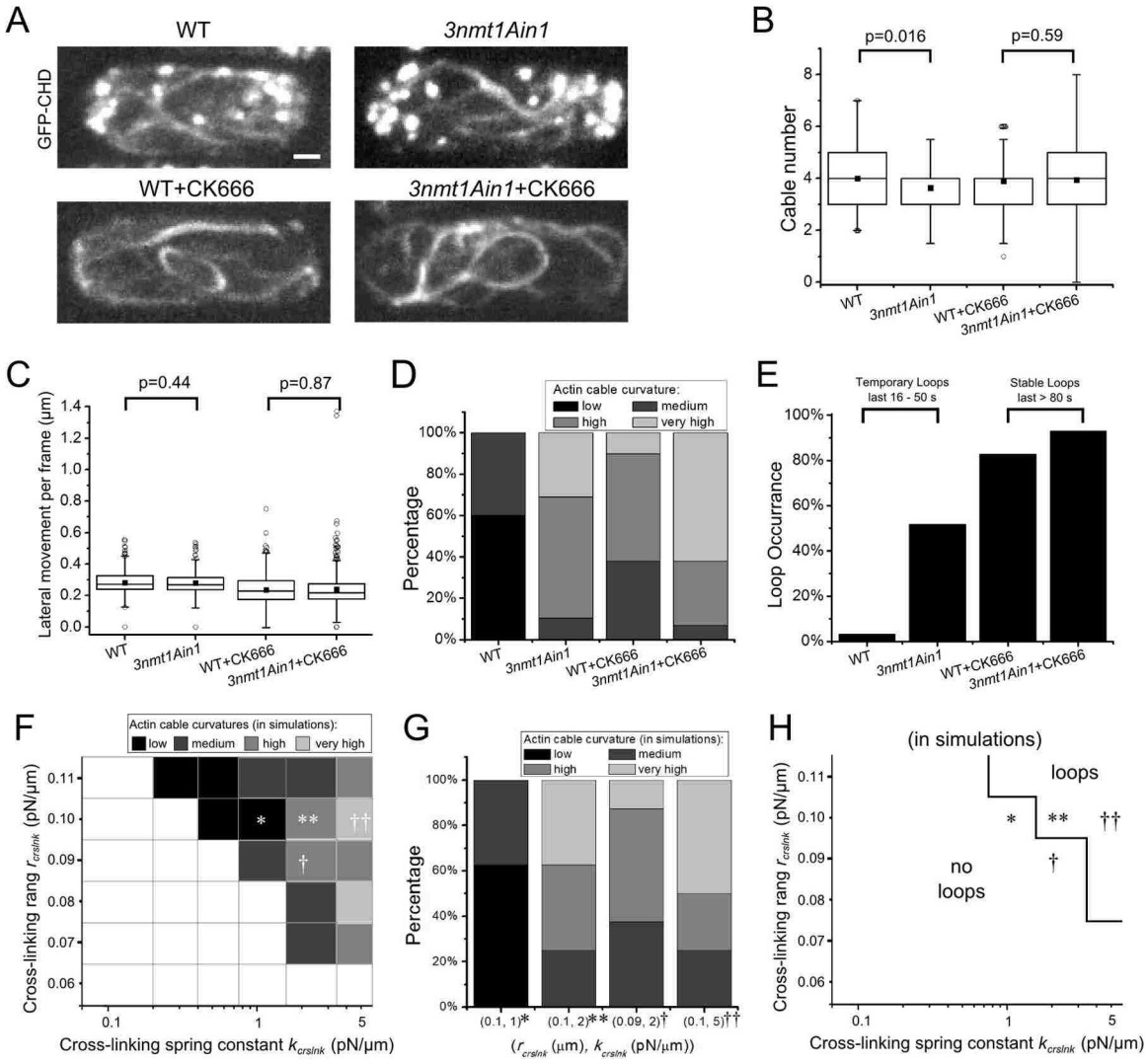

Figure 18. Actin cable morphology changes due to increasing Ain1 concentration in live cells. (A) Fluorescence microscopy shows GFP-CHD labeled actin of both wild type and 3nmt1Ain1 fission yeasts. CK666 is added to the cells to depolymerize actin patches (lower panel). (B) Measurement of cable number in different cells. (C) Measurement of lateral cable movement per frame, 8 s for WT and 10 s for other cases. (D) Curvature of the actin cables in different cells. (E) Loop occurrence in difference cells. For non-CK666 treated cells, loops occur rarely and lasts 16-50 s before disappearing. For CK666 treated cells, loops are stable and last more than 80 s. Dot in graph indicates average value; boxes contain 50% of data; whiskers: 1.5 interquartile range. (F)

Predominant cable curvature as function of cross-linking range and spring constant (n = 3 simulations per square). Symbols show one possible mapping of simulation parameters to experiments (*: WT; **: 3nmt1Ain1; †: WT+CK666; ††: 3nmt1Ain1+CK666). Cables cannot be clearly distinguished in the blank area. (G) Cable curvature distribution for the corresponding parameter sets of panel F (n = 8 per parameter set) match experiments of panel D. (H) Loop occurrences as a function of cross-linking range and spring constant for the same simulations as panel F.

3.3.5 Formin Clustering and Cable Structure

For3 generates cables from tip cortical sites containing ~10 For3 dimers per site (Martin and Chang, 2006). This For3 clustering may help the generation of actin bundles and control of their thickness. It is also possible that For3 clustering is not required for cable formation since filaments growing from For3 at distant tip sites can form bundles by cross-linking in the cytoplasm. We examined how actin cable distribution depends on the degree of clustering of For3 at cell tips and cross-linking among filaments. In Figure 19 we vary the number of cortical tip sites and distribute a fixed number of filament nuclei randomly among these sites. The cortical cluster sites are randomly distributed on the semi-spherical cell tip. Formins within the same cortical site are distributed randomly over a small area around the center of the site. We also study the interplay with cross-linking by varying the effective cross-linking range parameter r_{crslnk}.

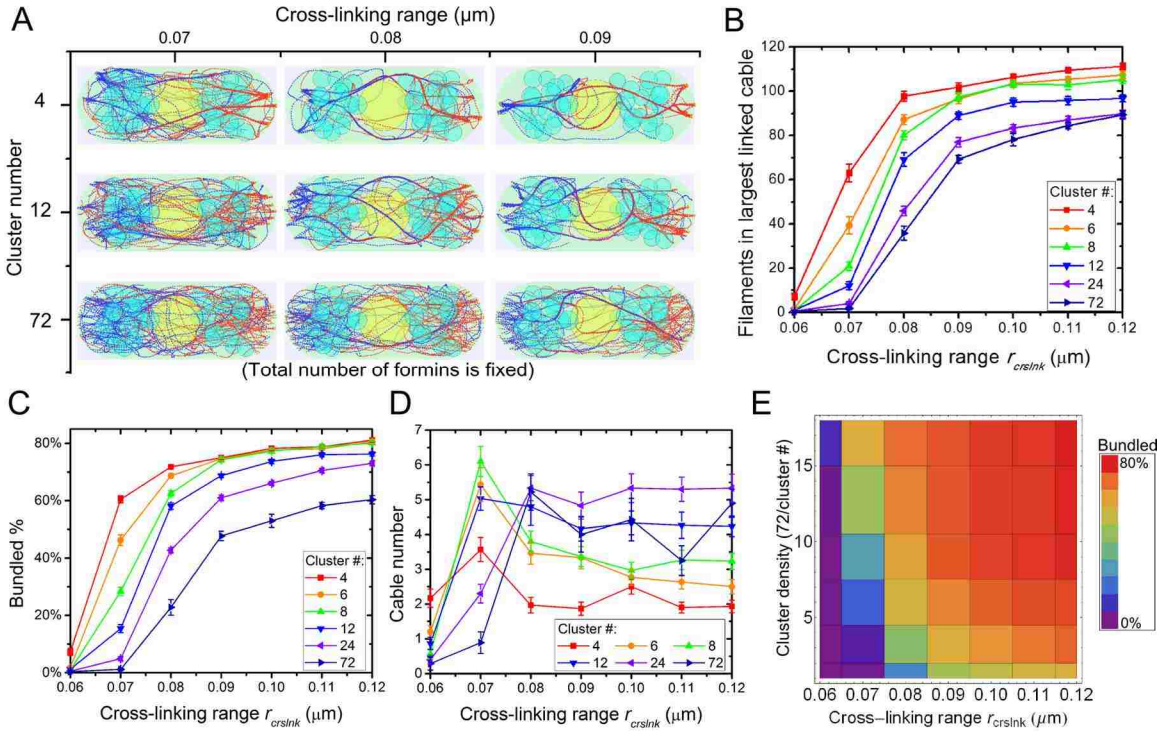

Figure 19. Clustering of For3 and increase in cross-linking strength promotes actin cable formation in simulations. (A) Steady state configurations under different cluster densities and cross-linking interaction range r_{crslnk} with 72 formin nucleation sites per cell tip partitioned in the indicated number of clusters. High For3 clustering (cluster number = 4) and large r_{crslnk} shows fewer and thicker actin cables. (B) Number of actin filaments in largest linked cable increases with increasing r_{crslnk} and cluster density. (C) Bundled actin filament percentage increases with increasing r_{crslnk} and cluster density. (D) Cable number as a function of r_{crslnk} and cluster density. (E) Bundled percentage landscape as function of cluster density and r_{crslnk} corresponding to (C).

The steady state configurations in Figure 19A indicate that formin clustering promotes bundling of actin filaments. The number of filaments in the largest linked cable and the percent of actin filaments found in bundles increases with increasing clustering and cross-linking range r_{crslnk} (Figure 19 B,C). For example, for r_{crslnk} = 0.07 μm, the number of

filaments in the largest linked cable grows from a composition of ~3 filaments to more than 60, while the bundled percentage of actin filaments grows from nearly 0 to 60% as clustering is increased. The number of cables in the system has a more complex dependence on the varied parameters (Figure 19D). At low cross-linking, r_{crslnk} = 0.06 μm, higher formin clustering generates more cables while for high cross-linking, r_{crslnk} > 0.08 μm, the effect is reversed. The reason is that for r_{crslnk} = 0.06 μm most filaments are unbundled (Figure 19C) and the clustering catalyzes the formation of a few bundles among many unbundled filaments. For r_{crslnk} > 0.08 μm, by contrast, most filaments (Figure 19C) get bundled through cross-linking interactions even when formins are unclustered; increasing formin clustering promotes the merging of these cables into thicker ones, leading to fewer cables.

3.4 Discussion

We developed simulations of fission yeast actin cables that incorporate the function of the major actin-filament regulators and take into account the excluded volume of cell organelles. Our model reproduces actin cable structures and dynamics observed in live cells. The simulations show how lack of directional myosin V pulling and obstruction by organelles leads to misoriented and curly cable structure as observed in *myoVΔ* cells (Lo Presti *et al.*, 2012). Two cross-linking parameters (r_{crslnk} and k_{crslnk}) affect the bundling of filaments into cables, but have different effects on cable morphology. We also predict formin clustering at the tips assists the bundling of actin filaments.

Our experimental analysis of wild type cells and cells overexpressing α-actinin (with or without CK666) show that the cable number, lateral cable movement, cable curvature and appearance of cable loops support the model predictions. The results of Figure 18D,E and the fact that fluctuations in lateral movement are larger in CK666 cells, as predicted in the strong parallel regime (Figure 16B), suggest that Ain1 overexpression and CK666 treatment both push the system towards the strong parallel regime.

Electron microscopy images of actin cables (Kamasaki *et al.*, 2005) suggest short segments of actin filaments exist in cables, which may be the result of severing by cofilin or occur during the extraction process. Given these uncertainties, we implemented an approximate description of actin turnover and did not attempt to predict filament length distributions along actin cables. The latter may however have implications on the mechanical properties on actin cables (Heussinger *et al.*, 2007) and relative filament sliding.

Some additional factors that may affect the structure of actin cables are to be explored in future work. We focused on cells in the G2 phase that are bipolar and 9 μm long on average. We did not explore the dependence on cell length or monopolar actin cable growth. Our model assumed filament polymerization exclusively at cell tips. Additional nucleation of actin filaments in the cytoplasm or binding of severed actin filament from patches to cables may help align cables over long distances across the cell, as observed in long *cdc25-22* cells (Huang *et al.*, 2012). Cross-linking was assumed isotropic, consistent with the measured cross-linking of filaments in both parallel and antiparallel orientations by fimbrin (Skau *et al.*, 2011) and α-actinin (Meyer and Aebi, 1990; Courson and Rock,

2010). Addition of cross-link orientation bias may shift the boundaries of the antiparallel and parallel bundle formation in Figure 12D. We also assumed the number of For3 nucleators at the cell tip is approximately constant. Formin For3 detaches from the cell tips and recycles back to the cell tips through diffusion (Martin and Chang, 2006; Wang and Vavylonis, 2008). Its activity may change in time as its Cdc42 activator tip concentration oscillates over 5 min (Das *et al.*, 2012). These mechanisms could contribute to larger fluctuations in cable thickness and movement. Tropomyosin that regulates myosin motor activity and filament stability is another important regulator of actin cables in fission yeast (Skau and Kovar, 2010; Cranz-Mileva *et al.*, 2013; Clayton *et al.*, 2014). In our model, these effects of tropomyosin are collapsed into the myosin V parameters and filament turnover time.

Actin filament cross-linker fimbrin may also play a role in regulating actin cable thickness as described in Figure 12. In vitro experiments show that full-length Fim1 bundles actin filaments, while truncated Fim1 binds actin filaments but does not bundle them (Nakano *et al.*, 2001; Skau *et al.*, 2011). Overexpression of truncated Fim1A2 (containing only one actin binding domain ABD2) generates thick cables in fatter and shorter fission yeast (Nakano *et al.*, 2001) and overexpression of the full length Fim1 results in disorganization of the actin patches and actin cables and to morphological cell defects (Nakano *et al.*, 2001; Laporte *et al.*, 2012). Deletion of fission yeast *fim1* causes a small change in cable orientation and mild polarity defects (Wu *et al.*, 2001; Skau *et al.*, 2011). It is likely that the role of fimbrin Fim1 is more complex than a simple tuning of cross-linking interactions in actin cables. Fim1 has not been detected on actin cables,

perhaps due its low concentration there, but is highly concentrated at the actin patches, regulating their turnover and limiting the effect of tropomyosin (Nakano *et al.*, 2001; Wu *et al.*, 2001; Skau and Kovar, 2010; Skau *et al.*, 2011). Models accounting for the effects of Fim1 concentration would involve considering its effect on the whole actin cytoskeleton that includes actin patches.

In our model the filament cross-link formation rate depends on $r_{crslnk,}$ (thus larger cross-linker concentration corresponds to larger $r_{crslnk,}$) while the rate of cross-link breakage depends on both r_{crslnk} and k_{crslnk} (breakage rate decreases as either parameter increases). These are effective parameters representing the combined action of multiple cross-linkers present in yeast cells. Changing these parameters (Figure 12) helps interpret and predict actin cable structures in cross-linker overexpression or deletion mutants. We note however that a more detailed model would be needed to calculate a more accurate dependence of our effective parameters on the properties and concentrations of multiple molecules that can cross-link actin filaments in different orientations and with different strength. While in many cases actin-filament cross-linkers have redundant function, the properties of a system with two types of cross-linkers can be complex. For example, networks cross-linked by α-actinin and fascin stiffen under shear (Tseng *et al.*, 2002). In actin networks cross-linked by fascin and filamin, structural and viscoelastic properties are modified independently (Schmoller *et al.*, 2008). The viscoelasticity of composite actin networks with α-actinin and palladin is modified by the two types of cross-linkers cooperatively (Grooman *et al.*, 2012). Cross-linking can also influence actin filament

turnover (Schmoller *et al.*, 2011), however we find our model predictions are robust to such an effect even when the turnover rate changes by a factor of 2 (Figure 20).

We performed simulations to study the effect of decreased actin filament disassembly with increased bundling, to explore the effect of reduction of filament disassembly due to cross-linking (Schmoller *et al.*, 2011). We implemented a dynamic turnover rate: average filament removal rates are 1/10 s^{-1}, 1/12.5 s^{-1}, 1/15 s^{-1}, 1/17.5 s^{-1}, 1/20 s^{-1} for total bundled filament length (l_b in μm) of $l_b < 1$, $1 < l_b < 3$, $3 < l_b < 5$, $5 < l_b < 8$, $l_b > 8$. The results are shown in Figure 20 (in all other simulations in this paper we have a fixed turnover rate 1/15 s^{-1}). We found bundled percentages are similar for both fixed and dynamic turnover rates (Figure 20A). The average filament length in the dynamic turnover case is however shorter in the low bundled phase (low k_{crslnk}) and longer in the high bundled phase (high k_{crslnk}) compared to the case with fixed turnover rate (Figure 20B and C). These results indicate that our conclusions with fixed turnover rate are robust even when the lifetime of actin filaments changes by a factor of two as a result of cross-linking.

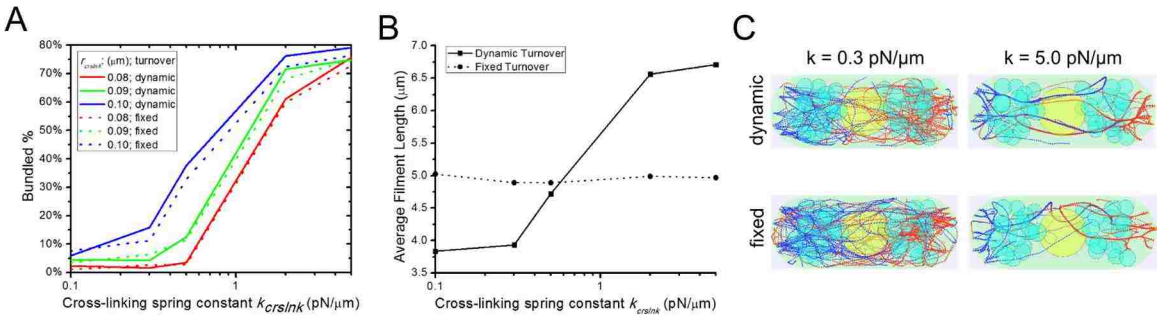

Figure 20. Comparison of simulations with cross-linker-dependent actin filament turnover rate to simulations with fixed turnover rate. In simulations with fixed turnover, the turnover rate was 1/15 s^{-1}. In the simulations with dynamic turnover this rate changed from 1/10 s^{-1} to 1/20 s^{-1} depending

on the total bundled filament length. (A) Similar bundled percentage for fixed (dotted line) and dynamic (solid line) turnover rate as a function of cross-linking range r_{crslnk} and k_{crslnk}. (B) Average filament length remains constant for fixed turnover rate (dotted line). Compared to the fixed turnover case (dotted line), the average filament length is shorter at low k_{crslnk} and longer at high k_{crslnk} for dynamic turnover rate (solid line). (C) Images of simulations showing effects described in panel B.

Budding yeast is another model organism where actin cable organization principles similar to the ones described above for fission yeast may apply. Fimbrin Sac6 cross-links actin filaments to bundles (Adams *et al.*, 1995; Cheng *et al.*, 1999; Sandrock *et al.*, 1999; Miao *et al.*, 2013). Similar to Fim1 in fission yeast, overexpression of Sac6 strongly influences the distribution of both actin patches and actin cables (Sandrock *et al.*, 1999) while deletion of Sac6 disrupts actin cables (Karpova *et al.*, 1995), and changes bud morphology (Watanabe *et al.*, 2009). Unlike cables in fission yeast that can grow from both tips, budding yeast cables grow from the bud into the mother and antiparallel cross-linking may be less important. In budding yeast, formins Bni1p at the bud tip and Bnr1 at the bud neck nucleate actin filaments at different polymerization rates (Huckaba *et al.*, 2006; Moseley and Goode, 2006). The difference in the rates of polymerization may be another factor regulating cable morphology as well as the fact that Bnr1 not only polymerizes actin filaments, but also serves as a bundling factor (Moseley and Goode, 2005). Another layer of complexity is that two types of myosin pull on actin cables in budding yeast. Type V myosin Myo2 moves processively along actin cables in the presence of tropomyosin (Hodges *et al.*, 2012b) while type II myosin Myo1 bound to the bud neck regulates actin cable retrograde flow (Huckaba *et al.*, 2006). A future model of

actin cable morphology in budding yeast would have to account for the above differences as well as the different bud-mother geometry. The present work provides a framework for such studies.

Chapter 4 Modeling Actin Cables in Budding Yeast

This chapter describes the computational actin cable model I built for budding yeast cell. The budding yeast has a more complex shape and different actin associated interactions. I modified the crosslinking interactions between actin filaments to be orientation-dependent and used a more realistic turnover mechanism. At the time of writing, the work in this chapter is in submission (Tang *et al.*, 2015).

4.1 Introduction

The actin cytoskeleton of budding yeast assembles into three distinct structures: actin patches, actin cables, and contractile rings (Amberg, 1998; Moseley and Goode, 2006; Bi and Park, 2012) (Figure 21A). These actin structures contribute to the polarized growth of the bud and its separation from the mother cell. They have been studied extensively experimentally to probe fundamental aspects of polarized growth and division, including mechanistic aspects of the actin cytoskeleton. The actin patches are dense networks of branched actin filaments nucleated by the Arp2/3 complex that assemble at sites of endocytosis and are enriched at the growing bud (Moseley and Goode, 2006; Bi and Park, 2012). Actin cables are long bundles of crosslinked actin filaments that extend from the bud to the mother cell. They serve as tracks for intracellular motor-driven transport of secretory vesicles, organelles, mRNA and regulate spindle alignment (Pruyne *et al.*, 2004). The actin cytokinetic ring is a bundle of antiparallel actin filaments that form around the septin ring structure that recruits myosin II and other proteins at the bud neck (Moseley and Goode, 2006; Bi and Park, 2012). Both actin cables and actin rings, which

are the topic of this paper, are nucleated by the two budding yeast formins Bni1 and Bnr1 (Evangelista *et al.*, 2002; Pruyne *et al.*, 2002; Chesarone *et al.*, 2010).

While a large amount of experimental work has focused on the study of budding yeast actin cables and contractile rings under the effect of genetic modifications, a clear picture of how molecular interactions lead to different macroscopic cable and ring organization remains a challenge. It has been established that during bud growth, Bni1 localizes at the bud tip and Bnr1 at the bud neck (Pruyne *et al.*, 2004; Buttery *et al.*, 2007). The actin filaments elongated out of these formin sites are bundled by fimbrin Sac6 and other proteins along actin cables (Adams *et al.*, 1991; Moseley and Goode, 2006). Cofilin, in coordination with other actin filament binding proteins such as coronin and Aip1, causes severing and turnover of actin filaments (Moon *et al.*, 1993; Iida and Yahara, 1999; Balcer *et al.*, 2003; Okada *et al.*, 2006). Type V myosin Myo2 and Myo4, carrying cargoes such as secretory vesicles, mitochondria and mRNA, walk along actin cables towards the barbed end and accumulates at the bud (Pruyne *et al.*, 1998; Reck-Peterson *et al.*, 2001a; Hodges *et al.*, 2012a). Myosin passenger protein Smy1 associates with Myo2 and interacts with Bnr1 to decrease the actin filament elongation rate (Chesarone-Cataldo *et al.*, 2011b). Type II myosin Myo1 localizes at the bud neck during both interphase and mitosis and affects actin cable retrograde flow rates and ring formation (Bi *et al.*, 1998a; Huckaba *et al.*, 2006). During mitosis, Bni1 joins Bnr1 at the neck where other actin filament binding proteins such as Iqg1/Cyk1 are also recruited to the septin ring at the bud neck (Bi and Park, 2012).

To systematically and quantitatively explore how the molecular interactions described in the preceding paragraph contribute to the development of cable and ring morphologies, here we develop a coarse-grained 3D computational model. By representing actin filaments as semiflexible polymers that can polymerize, sever, and respond to forces by cross-linking and motor proteins, we quantify different types of actin filament organization and the role of cell geometry. We show that a model based on these mechanisms can generate actin cable structures that resemble those in prior experiments. The model captures the morphology of cables in bnr1Δ and bni1Δ cells. In simulations with increased Bnr1 polymerization rate, long and wavy cables result, consistent with prior observations in smy1Δ cells. We describe the predicted response of cables to changes of motor pulling forces. By varying the interaction between actin filaments and the bud neck, our model shows that actin cables structures can transform into actin rings. These results suggest that tuning of a few key interactions by the cell guides the actin system towards a different morphology in order to perform a different biological function.

We conclude with a comparison to fission yeast and our previous 3D models of actin cable and contractile ring formation in fission yeast (Bidone *et al.*, 2014; Tang *et al.*, 2014). In comparison to the models in (Bidone *et al.*, 2014; Tang *et al.*, 2014), the present work includes two important technical improvements: 1) we include explicit severing of filaments into smaller fragments while in the earlier studies turnover was simulated as whole filament removal, and 2) cross-linking interactions have an explicit orientation dependence, which is likely to be more important in budding yeast that has the tight cross-linker fimbrin but lacks the more flexible α-actinin.

4.2 Model and Methods

4.2.1 Semiflexible polymer model for actin filaments

Actin filaments are simulated using a coarse-grained bead-spring model (Nédélec and Foethke, 2007; Tang *et al.*, 2014) (Section 2.1 The Model and Figure 21B). One bead represents a segment of the helical actin filament. The equilibrium distance between beads is $l_0 = 0.1\ \mu m$ (~37 subunits) connected by springs with spring constant large enough to resist extensional forces but small enough to allow a large simulation time step Δt = 2.5·10^{-4} s. Bending deformation and stochastic forces are included. These forces, together with the boundary, myosin motor, and crosslinking forces (to be described below), govern motion of the i^{th} bead through the following equation derived from Langevin dynamics:

$$\mathbf{F}_i^{\text{spring}} + \mathbf{F}_i^{\text{bend}} + \mathbf{F}_i^{\text{stoch}} + \mathbf{F}_i^{\text{boundary}} + \mathbf{F}_i^{\text{crosslink}} + \mathbf{F}_i^{\text{motor}} = \zeta_{\text{b}} \frac{\mathrm{d}\mathbf{r}_i}{\mathrm{d}t}, \qquad (20)$$

where $\mathbf{r}_i$ is the 3D position vector and ζ_{b} is an effective drag coefficient of a filament segment in the cytoplasm. The spring, bending and stochastic forces are as follows:

$$\mathbf{F}_i^{\text{spring}} = -\frac{\partial E^{\text{spring}}}{\partial \boldsymbol{r}_i} = -\frac{k}{2}\sum_{j=1}^{N-1} \frac{\partial\left(|\mathbf{r}_{j+1}-\mathbf{r}_j|-l_0\right)^2}{\partial \mathbf{r}_i},$$

$$\mathbf{F}_i^{\text{bend}} = -\frac{\partial E^{\text{bend}}}{\partial \mathbf{r}_i} = -\frac{\kappa}{l_0}\sum_{j=2}^{N-1} \frac{\partial\left(\mathbf{t}_j \cdot \mathbf{t}_{j-1}\right)}{\partial \mathbf{r}_i}, \qquad (21)$$

$$\langle \mathbf{F}_i^{\text{stoch}} \cdot \mathbf{F}_i^{\text{stoch}^{\text{T}}} \rangle_{\alpha,\beta} = \frac{2k_{\text{B}}T\zeta_{\text{b}}}{\mathrm{d}t}\hat{I}_{\alpha,\beta},$$

where $\mathbf{t}_i \equiv \frac{\mathbf{r}_{j+1}-\mathbf{r}_j}{|\mathbf{r}_{j+1}-\mathbf{r}_j|}$ is the local unit tangent vector, $\kappa = k_B T l_p$ is the flexural rigidity, k_B is Boltzmann's constant, T is temperature, l_p is the persistence length of the filament and $\hat{I}_{\alpha,\beta}$ is the second-order unit tensor. This filament model reproduces the correct tangent correlation function, relaxation dynamics and equipartition of energy in thermal equilibrium as in (Tang *et al.*, 2014) and Section 3.2 Model, Methods and Materials.

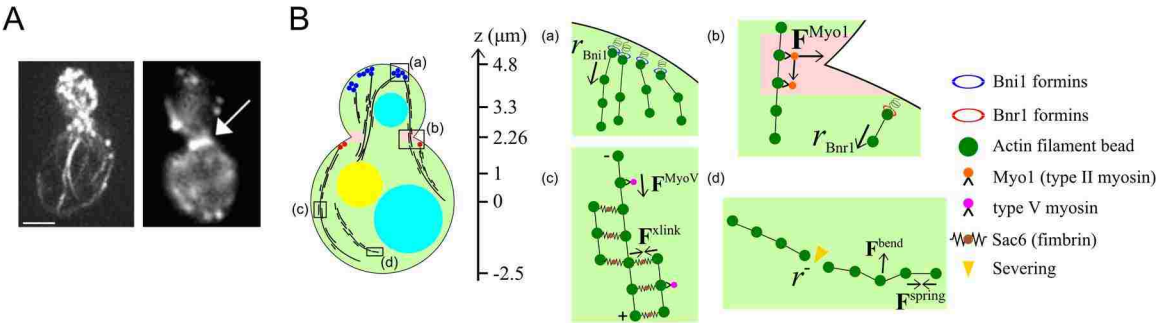

Figure 21. Model description (A) Experimental images of phalloidin-stained actin cables (Liu *et al.*, 2012) (left) and cytokinetic ring (Tolliday *et al.*, 2002) (right, arrow) in budding yeast. Scale bar: 2 μm (B) A schematic diagram shows the geometric shape we use for budding yeast, with one sphere centered at (0,0,3.3) with radius 1.5 μm (bud) and another centered at (0,0,0) with radius 2.5 μm (mother). The two spheres intersect at *z* = 2.26 μm to form the neck. The two cyan and one yellow spheres represent two vacuoles and the nucleus, respectively. (Right) Schematic of implemented simulation mechanisms. (a) Beads representing Bni1 formins placed at the bud tip (blue) polymerize actin filaments (dark green beads). (b) Within the ring-shaped area around the neck (pink), the filament beads experience forces in both tangential and outward directions, representing binding to Myo1 (orange). At the neck, beads representing Bnr1 formins (red) are placed on the mother cell boundary, right below the neck where they polymerize actin filaments at a faster speed compared to Bni1. (c) Myosin V motors (violet) bind to the actin filaments at a certain rate and exert forces toward the barbed ends. An attractive interaction (brown), representing cross-linking is established when two actin filament beads come close to one

another, This interaction depends on the relative orientation of the filaments. (d) Connections between filament beads are severed (yellow) with a rate that depends on the age of the connecting spring, representing age-dependent filament severing by cofilin and cofactors.

4.2.2 Formin-mediated actin filament polymerization

Polymerization of actin filaments out of formins associated with the cell membrane is simulated as elongation of the equilibrium length of the segment between the formin and the first filament bead representing the current barbed end. If the elongating segment reaches twice the size of the spring equilibrium length l_0, a new bead is added to the middle of the segment (Figure 21B). Since formins connect to the cortex through flexible FH1 domains, we assumed the filament ends can rotate freely around their attachment point on the membrane. This is represented in the model as a freely-rotating spring connecting the first filament bead to a point on the surface (with spring constant 100 pN/nm). We assume the polymerization rate is a constant. We neglect fluctuations in formin-mediated polymerization rates that may arise from force fluctuations at the filament end (Courtemanche *et al.*, 2013; Jegou *et al.*, 2013). Actin cables have been measured to extend with a retrograde flow rate of 0.2 – 0.6 μm/s (Yang and Pon, 2002; Huckaba *et al.*, 2006) while studies using TIRFM found a large range of cable movements with speeds exceeding 1 μm/s (Chesarone-Cataldo *et al.*, 2011b; Yu *et al.*, 2011). In vitro assays give Bni1 and Bnr1 polymerization rates that vary depending on the concentration of formins, actin and profilin (Kovar and Pollard, 2004; Moseley and Goode, 2005). As reference values in simulations, we use the Bnr1 and Bni1 polymerization rates 0.6 μm/s and 0.3 μm/s, respectively, taking into account

measurements of average cable extension rates that are higher in *bni1Δ* cells compared to wild type (Chesarone-Cataldo *et al.*, 2011b) (though we note that (Yu *et al.*, 2011) provide evidence that Bni1 polymerizes at a faster rate compared to Bnr1).

Bni1 accumulates in clusters at the bud tip, recruited and activated by polarisome complex containing Spa2, Pea2 and Bud6 (Moseley and Goode, 2006). In our simulations we assume 11 clusters of 6 Bni1 dimers each randomly distributed at the top half of the bud sphere. The Bni1 formin sites are randomly distributed within a small area close to the centers of the clusters as in (Tang *et al.*, 2014). Neck formins Bnr1 are randomly distributed at the cell membrane periphery at 0.1 μm below the neck, towards the mother.

4.2.3 Filament turnover

The precise mechanism of actin cable turnover has not been established, however a large body of work suggests a significant contribution of filament severing, mediated by cofilin, Aip1, coronin, twinfillin, cyclase-associated protein, and tropomyosin (Moon *et al.*, 1993; Iida and Yahara, 1999; Balcer *et al.*, 2003; Moseley and Goode, 2006; Okada *et al.*, 2006). As actin filaments are polymerized out of the formin sites, ATP-bound actin subunits are hydrolyzed into ADP-P_i-actin and further release phosphate to convert into ADP-actin. Cofilin binds to the sides of actin filaments, accelerates phosphate release and severs ADP-actin (Blanchoin *et al.*, 2014). Together, these processes are expected to lead to a cooperative, age-dependent severing mechanism. Similar to (Wang and Vavylonis, 2008), we use Hill function to assign different disassembly rates for different segments of the filament:

$$r^{-}(t) = r_{\max}^{-} t^{n} / (t^{n} + \tau_{\text{age}}^{n}) \tag{22}$$

where $r_{\max}^{-}$ is the maximum rate of disassembly for fully aged segments, τ_{age} is the characteristic time of aging and n is a cooperativity coefficient. Every Δt, each segment between two filament beads is tested for severing. Upon severing, the specific segment is removed, generating two shortened filaments.

4.2.4 Filament crosslinking

The cross-linking interaction between actin filaments is simulated as an attractive force between the filament beads that come close to one another. This represents an effective interaction, averaged over multiple cross-links between the corresponding filament segments. Unlike in (Tang *et al.*, 2014) and Chapter 3 where we used an interaction that only depends on the distance between beads, here we use an orientation-dependent spring potential to represent such force. An attractive spring force is exerted when the distance between bead i and bead j from a different filament is smaller than crosslinking interaction distance r_{c}, and when the unit direction vector is nearly perpendicular to the local tangent vectors of the two interacting filaments:

$$\mathbf{F}_i^{\text{xlink}} = -\frac{k_{\text{c}}}{2} \sum_j \frac{\partial \left(\left| \mathbf{r}_i - \mathbf{r}_j \right| - r_0 \right)^2}{\partial \mathbf{r}_i} \tag{23}$$

for $\left| \mathbf{r}_i - \mathbf{r}_j \right| \leq r_c$ and $\mathbf{u}_{ij} \cdot \mathbf{t}_i < 0.5$ and $\mathbf{u}_{ij} \cdot \mathbf{t}_j < 0.5$, where $\mathbf{u}_{ij}$ is the unit vector pointing from bead i to bead j, $\mathbf{t}_i$ and $\mathbf{t}_j$ are the local filament tangent unit vectors, r_0 is

the equilibrium length and $k_c$is the corresponding spring constant. This force is stronger when filaments align in parallel or anti-parallel, consistent with the ability of fission-yeast fimbrin to crosslink actin filaments to form compact bundles (Skau *et al.*, 2011) and the lack of alpha-actinin in budding yeast that would allow for a large range of crosslink angles (Wu *et al.*, 2001). We used r_0= 12 nm, of order the size of fimbrin (Volkmann *et al.*, 2001; Klein *et al.*, 2004). We use a crosslinker spring constant k_c in the range 1 – 10 pN/μm, which corresponds to the modulus of fimbrin, 10 – 10^2 pN/μm^2 (Klein *et al.*, 2004) (assuming length 0.01 μm, cross-section 10^{-4} μm^2, 10 fimbrin proteins per 0.1 μm segment).

4.2.5 Actin filament pulling by myosin motors and bud neck proteins

We account for the two types of myosin motor proteins, type II and V, that influence actin cable behavior in budding yeast. The only type II myosin in budding yeast, Myo1, localizes around the bud neck during bud growth and cytokinesis (Bi *et al.*, 1998a; Huckaba *et al.*, 2006) and contributes to increasing actin cable retrograde flow rates by 2 fold (Huckaba *et al.*, 2006).To account for the presence of Myo1 at the neck, we assume that filament beads reaching a ring-shaped area around the bud neck experience two forces due to Myo1 (Figure 21A): a pulling force toward the barbed end, $\mathbf{F}_{\mathrm{pull}}^{\mathrm{Myo1}}$, as well as an attractive force towards the closest point on the bud neck, $\mathbf{F}_{\mathrm{capt}}^{\mathrm{Myo1}}$. The reference value of the magnitude of these two forces, which represents capture and pulling, was 0.5 pN. Since typically two filament beads are within range to the bud neck, this corresponds to total forces 1 pN. Since the simulations do not implement tension-dependent actin

filament elongation rates, the retrograde flow rate is not influenced significantly my Myo1 pulling. To simulate the effects of actin filament binding to proteins bound at the septin ring at the bud neck during contractile actin ring assembly (Mavrakis *et al.*, 2014), we add a force of same direction and varying magnitude to $\mathbf{F}_{\text{capt}}^{\text{Myo1}}$.

Type V myosins Myo2 and Myo4 bind to the sides of the actin filaments and walk towards the barbed ends, carrying secretory vesicles, mitochondria, late Golgi elements or attaching to static vacuoles (Reck-Peterson *et al.*, 2001b; Pruyne *et al.*, 2004). We approximate the myosin V pulling force F^{MyoV} as a tangential force on filament beads of magnitude 0.8 pN, smaller than the myosin V stall force of 3 pN (Mehta *et al.*, 1999) (Figure 21B). This estimate is calculated by assuming that myosin V opposes the drag force on a carried vesicle $F^{\text{MyoV}} = 6\pi\eta r v$. Here η is the cytoplasmic viscosity (see Table 2), the vesicle radius r = 100 nm as indicated in electron microscopic vesicle images (Klemm *et al.*, 2009) and v = 1.4 μm/s is the walking speed taken from in vitro and live cell experiments that indicate speeds 1 - 5 μm/s (Schott *et al.*, 2002a; Sheltzer and Rose, 2009; Hodges *et al.*, 2012a). Since the duration of vesicle movement is of order 0.5 s (Schott *et al.*, 2002b), in the simulations we assume that each filament bead experiences a transient tangential force for 0.5 s, with a probability giving a linear density of myosin V pulling forces ρ_{MyoV}. We varied ρ_{MyoV} to simulate the effects of deletion and overexpression of type V myosins.

Table 2. Reference parameter values used in budding yeast cable simulations.

Parameter	Description	Value
Shape:		
V_{bud}	Volume of the bud	14.14 μm^3
V_{mother}	Volume of the mother cell	65.45 μm^3
V_{bvac}	Volume of the vacuole in the bud	0.9 μm^3
V_{mvac}	Volume of the vacuole in the mother cell	7.23 μm^3
D_{nuc}	Diameter of nucleus	1.6 μm
z_{neck}	Neck z location	2.26 μm
r_{neck}	Neck radius	1.08 μm
Filament:		
T	Temperature	300 K
l_p	Persistence length of actin filaments	10 μm
κ	Flexural rigidity, $\kappa = k_B T\, l_p$	0.0414 pN·μm^2
l_0	Filament model segment equilibrium length	0.1 μm
k	Spring constant	100 pN/μm
η	Cytoplasmic viscosity (350 times larger than water)	0.301 pN/μm^2·s
τ_{age}	Actin filament aging time	5 s
n	Hill severing function coefficient	6
r_{max}^{-}	Aged actin severing rate	0.08 s^{-1}
Formins:		
N_{Bni1}	Number of active Bni1 formins	55
N_{Bnr1}	Number of active Bnr1 formins	40
r_{Bni1}	Bni1 formin polymerization rate	0.3 μm/s
r_{Bnr1}	Bnr1 formin polymerization rate	0.6 μm/s
$N_{cluster}$	Number of clusters of Bni1 formins	11
Crosslinking:		
k_c	Cross-linking spring constant	4 pN/μm
r_0	Cross-linking gap distance	0.012 μm
r_c	Cross-linking interaction range	0.10 μm
Myosin:		
F^{Myo2}	Myo2 walking force	0.8 pN
ρ^{Myo2}	Myo2 linear density along filament	0.7 μm^{-1}
τ_{Myo2}	Myo2 average lifetime on actin filament	0.5 s
F^{Myo1}	Myo1 walking and outward pulling force	0.5 pN
r_{Myo1}	Thickness of the Myo1 interaction area around the neck	0.3 μm
h_{Myo1}	Height of the Myo1 interaction area around the neck	0.1 μm

4.2.6 Budding yeast shape and excluded volume by vacuoles and nucleus

Since in this work we consider the spatial distribution of actin cables, we took into account the large excluded volume presented by the nucleus and vacuoles. We used numbers for yeast shape and location of the yeast nucleus and vacuoles from electron microscopy images (Klionsky *et al.*, 1990; Voeltz and Prinz, 2007; Bertin *et al.*, 2012). The shape of G2 phase budding yeast is represented by two spheres intersecting at the neck of radii 2.5 μm and 1.5 μm, for the mother and daughter, respectively (Figure 21B). These numbers correspond to the centers of the bud and mother cell volume distribution in (Chan and Marshall, 2014). They are positioned such as the bud neck has radius 1 μm. Narrower bud necks that are closer to typical neck radii of order 0.5 μm were also considered, see Results section. We placed two vacuoles, one in the mother cell, one in the bud, with radii 1.2 μm and 0.6 μm. This gives vacuole to bud volume and mother vacuole to mother volume ratios consistent with the distributions in (Chan and Marshall, 2014). Reflecting boundary conditions are imposed at the boundaries by application of a perpendicular force of magnitude 1 pN to any bead crossing it.

4.2.7 Calculation of cable number, thickness, curvature and filament tension

For our analysis we picked time points after 60 s, a number higher than the characteristic severing time (5 s from Table 2) and free filament relaxation time (4.5 s for 2-μm-long filament). By that time parameters such as number of filament beads, cable thickness and curvature reach a plateau. However we note that the longest relaxation time of the system may be very long, involving processes such as whole filament unbundling. For this

reason the results after 60 s have a small dependence on initial conditions, such as the initial angle of polymerization. By changing the initial angle of filament polymerization, we checked that the effect is not significant, except for cases such as simulated *bni1Δ* cells that are discussed separately.

Since simulated cables are connected and branched, we measure the cable number and thickness by grouping the points of the cables intersecting the cross-section planes at z = 3.3, 2.26, 1, 0, -1 μm (Figure 21B). If the distance between two points is smaller than r_c, the two points form a pair. A group is defined as a collection of points with all and only their corresponding pairs. If a group contains more than 4 points, it qualifies as a cable. The filament curvature is calculated by $\kappa = \left|\frac{\Delta \mathbf{t}}{\Delta s}\right| = \left|\frac{\mathbf{t}(s+\Delta s)-\mathbf{t}(s)}{\Delta s}\right|$, where we used $\Delta s = 4l_0$ and filaments longer than 10 beads. The average filament tension is calculated by averaging all the extension and compression of the related segments (Bnr1, Bni1 associated or free filaments) and multiplying by the spring constant k.

4.3 Results

4.3.1 Simulations reproduce actin cable structures

We first examined actin cable formation in interphase budding yeast cells. Simulations successfully reproduced 3D actin cable structures that are similar to those observed in fluorescence microscopy images (Figure 21A). Table 2 shows the parameter values used in simulations (for justification of parameter values see also Model and Methods). Actin filaments elongate from the two sites of formin localization at the bud neck and bud

(Bnr1 randomly distributed at the neck and Bni1 clusters at the bud tip), get crosslinked and form bundles (Figure 22A; Bnr1-associated, Bni1-associated and free filaments are in red, blue, gray respectively). The average number of cables in the mother, at z = 3.3 μm of Figure 21B is 5.2, close to the count of about 5 in previous experiments on wild type cells (Lipkin, 2011). From different perspectives, the simulated mature actin cable structures are extended and smooth structures on the cell scale (Figure 22B). Actin cables curve and connect at the bottom, as a result of the mother cell boundary. As viewed from the top, clustering of Bni1 formins help bundle the actin filaments (Figure 22B). Projection of the actin filaments on a plane (where the pixel intensity is proportional the cable thickness) generates images resembling those observed in prior experiments (Figure 22C, inverted gray scale).

The actin cables were robust to changes in the size of the bud and mother size (Figure 23). Actin cables can also form with bud neck radii 0.5 μm (the typical case (Bertin *et al.*, 2012) rather than 1 μm as in Figure 22). Narrower bud necks generally result in increased bundling of the simulated Bni1 filaments. This effect is increased by the effective additional narrowing when positioning the vacuole close to the neck. Since our model is coarse-grained on the 0.1 μm scale (distance between filament beads), we focused on larger neck diameters that are better described by our model.

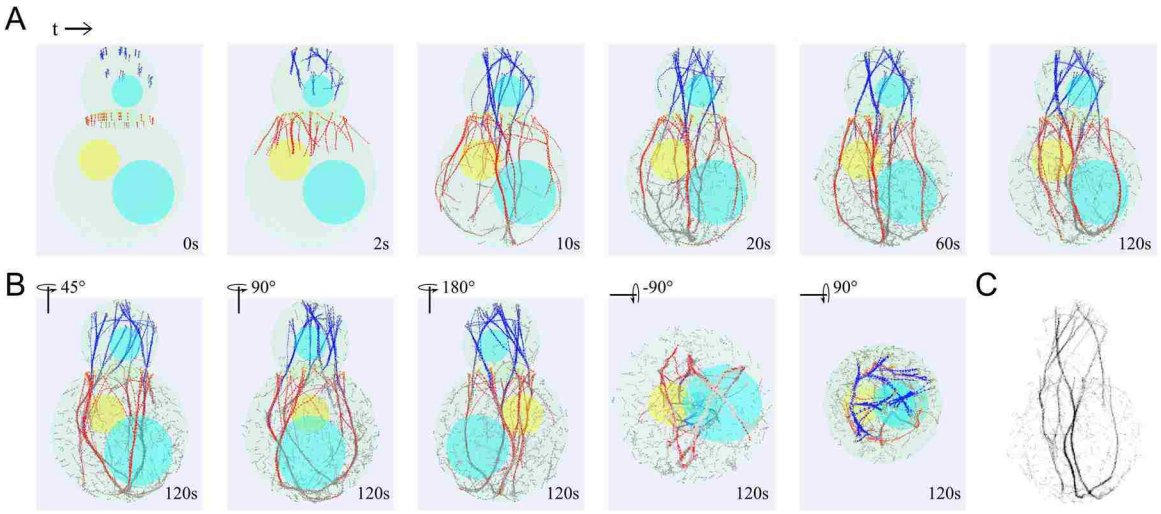

Figure 22. Simulation snapshots showing actin cable formation. (A) Simulation snapshots using parameters from Table 2 show the time evolution of actin cable structures and dynamics. Bni1-associacted actin filaments shown in blue, Bnr1-associated filaments in red and severed filament segments in gray. Formin sites shown as circles at the barbed ends of filaments. The nucleus and vacuoles are shown in yellow and blue. (B) Rotated images of simulation at 120s showing a robust 3D actin cable structure. (C) Projection of the simulated actin cable structure on the *y-z* plane (*z* is along the mother-bud axis) to compare to fluorescence microscopy images. The image was calculated by assigning to each pixel (of size 0.04 μm) an intensity proportional to the sum of all filament beads with the same *y, z* coordinate, within a range *x* values and inverting the final result.

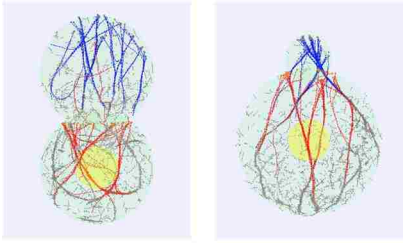

$r_{bud} = 2.1$ μm
$r_{mother} = 2.1$ μm

$r_{bud} = 0.9$ μm
$r_{mother} = 2.7$ μm

Figure 23. Cable structure is robust to changes in bud/mother size. (A) Simulation snapshot of big bud centered at (0,0,3.5) with radius 2.1 and small mother cell centered at (0,0,0) with radius 2.1 (units: μm). Neck radius: 1.16 μm. (B) Simulation snapshot of small bud centered at (0,0,3.1) with radius 0.9 and big mother cell centered at (0,0,0) with radius 2.7 (units: μm). Neck radius: 0.75 μm.

In the simulations the main body of actin cables consists of long filaments that are associated with formins while the older segments contain severed filaments. Some severed filament fragments remain as parts of actin cables while the short ones detach and depolymerize completely in the bulk of the simulated cell. We found a weak dependence of cable structure on the cooperativity coefficient n of severing kinetics in Equation (3) (Figure 24), however the aging time τ_{age} contributes to the length of the cables.

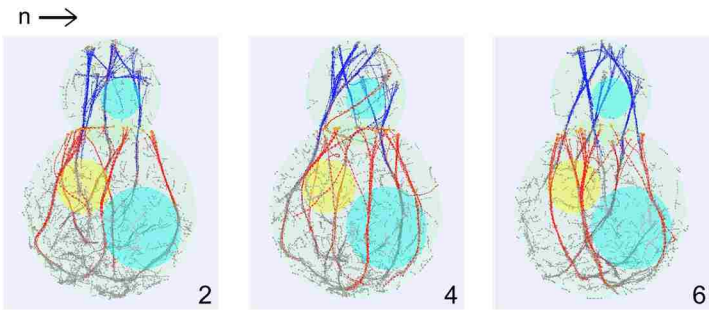

Figure 24. Effect of filament severing cooperativity parameter *n*. In our simulations, the actin filament severing rate is described a Hill function with cooperativity coefficient *n,* Equation (3). Higher values of *n* represent stronger cooperativity and the lengths of actin filaments are less variable. Snapshots of simulations at 120 s with *n* varied from 2 to 6, with other parameters from Table 2 (the value of *n* used in all other simulations in this paper is *n* = 6). There is no significant

change in cable structure, however with increased *n* the formin associated actin filaments (red and blue) are less likely to sever at shorter length.

The result of Figure 22 indicates that the minimal set of interactions in our simulations – polymerization, thermal fluctuations, filament mechanical properties, crosslinking, myosin pulling, excluded volume and turnover – were able to represent the major features of the actin cables in budding yeast. While use of the simpler whole-filament-turnover and orientation-independent filament bead crosslink mechanism of (Bidone *et al.*, 2014; Tang *et al.*, 2014) can also produce actin cable structures (Figure 25), the current model also contains a model of actin filament oligomers that may have a complex role in actin dynamics (Okreglak and Drubin, 2010; Chen and Pollard, 2011). These simulations thus provide a way for us to pry into the system and study it quantitatively.

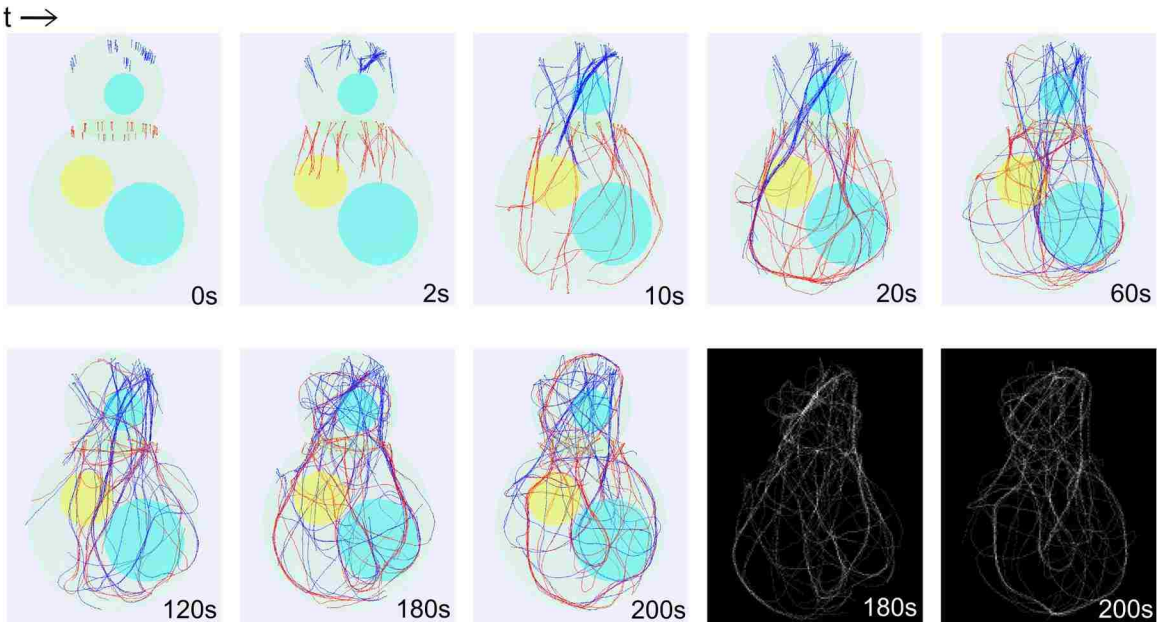

Figure 25. Actin cable formation using the turnover and crosslinking mechanism of (Bidone *et al.*, 2014; Tang *et al.*, 2014). Actin cable structures are also seen when using a crosslinking potential

(r_c = 0.12 μm and k_c = 2 pN/μm) between filament beads that is not angle-dependent and simulating turnover by removing the whole filament with a rates that correspond to the average filament length of 6 μm (1/20 s^{-1} for Bni1 filaments and 1/10 s^{-1} for Bnr1 filaments). Lower right are two projected images.

4.3.2 Actin cable formation requires sufficiently high crosslinking interaction strength

In our model, two parameters together regulate the crosslinking kinetics: r_c and k_c, which represent the cutoff range and depth of the crosslinking interaction potential. These parameters determine the rates of cross-link formation/breakage and reflect the type and concentration of cross-linker proteins in cells, with larger values representing stronger cross-linking (Tang *et al.*, 2014). We explored the crosslinking parameter space and found a clear trend of increased bundling as we increase either r_c or k_c (Figure 26A). The average number of cables exhibits a plateau phase of highly bundled filaments (with cable numbers between 4.5 and 5.5) at high r_c and k_c, and an unbundled phase at low r_c and k_c (Figure 26B). The cable thickness increases with r_c (Figure 26C) and is in the range 7 to 10 filaments within the highly bundled phase.

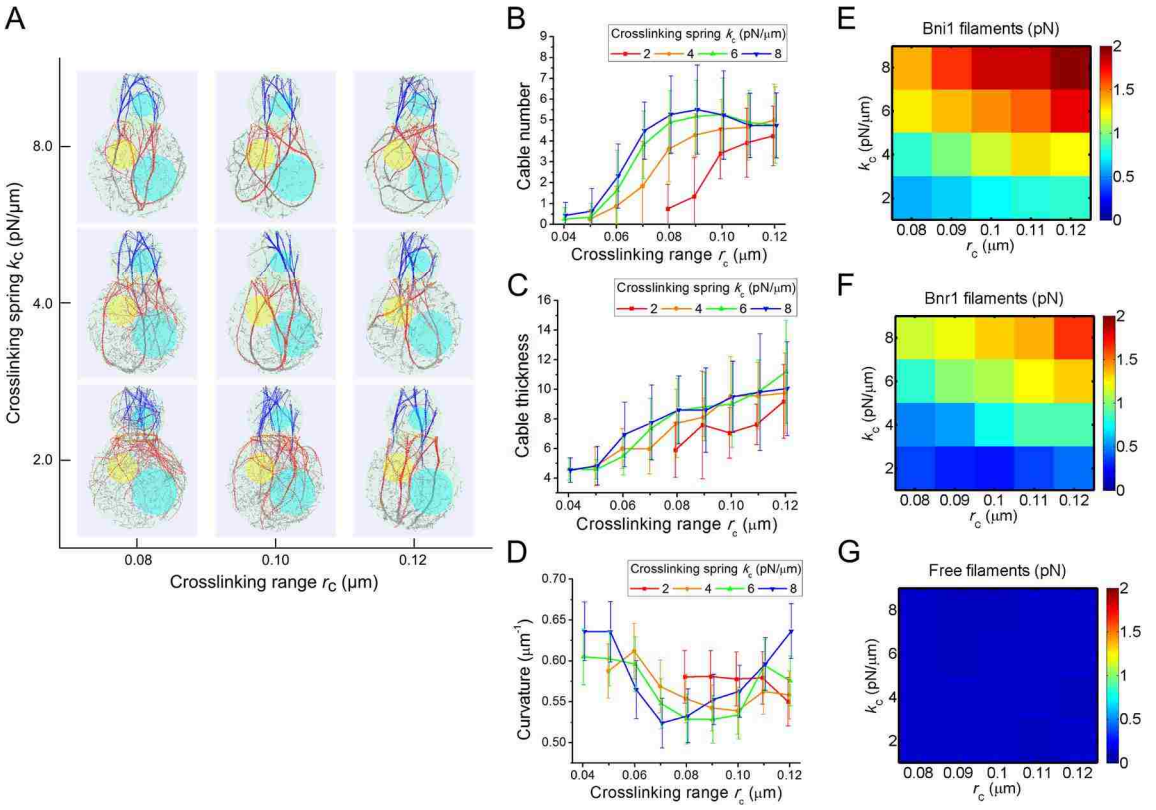

Figure 26. Effects of crosslinking interactions in cable formation. (A) Simulation snapshots (at 80 s) under different crosslinking range r_c and spring constant k_c. Actin filaments become more bundled with increase of either parameter. (B) Average cable number as a function of r_c, for different k_c. In this and following panels, each point is an average of measurements of five cross-section measures (z = 3.3, 2.26, 1, 0, -1 μm) of 15 time points (separated by 10 s starting at 60 s) from 3 independent runs. The error bar is the standard deviation among all measurements. (C) Average cable thickness as a function of r_c for different k_c. (D) Average filament curvature as a function of r_c for different k_c. The curvature is a non-monotonic function of either variable (see main text). (E-G) Heat map of average tensile forces of Bni1-associated (E), Bnr1-associted (F) and free (G) filaments under different r_c and k_c. As cables get more bundled, forces in Bni1 and Bnr1 filaments segments increase.

We further investigated the curvature of actin cables as function of crosslinking strength. We noticed a complex behavior in Figure 26D due to two factors that affect cable curvature: 1) bundling of actin filaments results in a bundles of higher bending rigidity, which reduces the curvature and 2) the difference in polymerization rates between Bni1- and Bnr1-associated filaments causes bending of the cables due to forces that prevent filament sliding with the cable, which increases the curvature - an effect discussed in the prior model of fission yeast cables (Tang *et al.*, 2014). These two trends result in a bowl-shape curve for k_c = 4, 6, 8 pN/μm with increasing r_c in Figure 26D. Consistent with this interpretation, in simulations that lack Bni1 filaments, there is no noticeable increase in curvature at large r_c (not shown). To further quantify bundling-related deformation, we measured the average tensile forces in Bni1, Bnr1 associated and free filament segments. Increasing crosslinking parameters causes the tensile force of the Bni1 and Bnr1 filament to increase by four-fold, while in the free filaments, the forces barely change (Figure 26E, F and G). In selecting the standard parameter set for the simulations, we used r_c or k_c that are large enough to produce bundles but low enough to avoid excessive cable bending.

4.3.3 Simulated loss of Bni1 or Bnr1 disrupts the cable numbers but not cable thickness

Deletion of either Bni1 or Bnr1 formin leads to a decrease in the total intensity of actin cables in the mother cell during polarized growth (Evangelista *et al.*, 2002; Pruyne *et al.*, 2004; Buttery *et al.*, 2007; Chesarone-Cataldo *et al.*, 2011b; Liu *et al.*, 2012). In published images of *bni1Δ* cells the number of actin cables that remain in the mother cell

has no drastic decrease as compared to wild type cells, however *bnr1Δ* cells show cables in the bud but only sparse cables extending to the mother (Evangelista *et al.*, 2002; Buttery *et al.*, 2007; Chesarone-Cataldo *et al.*, 2011b; Liu *et al.*, 2012). Due to the high fluorescent intensity of actin patches inside the bud, it is hard to quantify how the number and thickness of actin cables change in the bud in prior experimental images.

We next tested if our model can reproduce the behavior in cells lacking Bni1 or Bnr1. In simulations lacking Bnr1, actin cables are observed inside the bud and extend to the mother cell (Figure 27A). Due to constant severing, there are only sparse actin cables in the mother. Simulations without Bni1 show robust structures of actin cables inside the mother and occasional single filaments going into the bud, which are unable to bundle into cables (Figure 27A). Robust cables in the mother also occur when placing the Bnr1 formins at the bud neck cusp (rather than below the neck) and when the initial angle of Bnr1 polymerization is random rather than vertical. This occurs even though the initial number of filaments growing towards the bud is different in each case. The origin of this behavior is that myosin V pulling stretches the actin filaments and gives a preference for bundle formation in the larger mother cell.

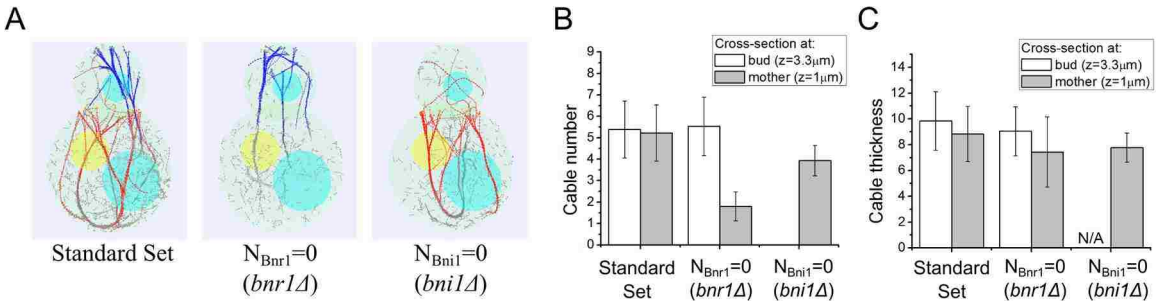

Figure 27. Simulations of formin deletion (bni1Δ and bnr1Δ). Parameter sets taken from Table 2 unless otherwise indicated. (A) Simulation snapshots at 120 s using standard parameter set (left), without neck formins (middle), and without bud tip formins (right), simulating wild type, bnr1Δ and bni1Δ mutants, respectively. (B) Cable number at cross-sections z = 3.3 μm in the bud and z = 1 μm in the mother cell. With NBnr1 = 0, the number of cables in the bud is not significantly different from that in the standard set, but the number of cables in the mother is reduced significantly. With NBni1 = 0 simulations, there are slightly smaller number of cables in the mother cells and none in the bud. (C) Cable thickness at the same cross-sections as panel B. The cable thickness does not very significantly in the three cases in either bud or mother. In panels B and C, each point is an average of measurements at 15 time points, separated by 10 s starting at 80 s, from 3 independent runs; error bars are one standard deviation.

We quantified the number and thickness of actin cables by investigating the cross-sections inside the bud and the mother, at z = 3.3 μm and 1 μm, respectively, as in Figure 21B. First, taking out Bnr1 does not alter the number of cables inside the bud (5.5 ± 1.3 comparing to 5.4 ± 1.3; average±StDev), while inside the mother, the cable number decreases from 5.2 ± 1.3 to 1.8 ± 0.7 (Figure 27B). Second, taking out Bni1 leads to absence of cables inside the bud and the number of cables in the mother decreases to 3.93 ± 0.70 (Figure 27B). Third, the cable thickness (i.e. number of filaments of the cable penetrating the cross-section) inside the bud (for Bnr1 deletion) and inside mother (for

either Bnr1 or Bni1 deletion) is slightly lower than the wild type case, but the change is small compared to the magnitude of the standard deviation (Figure 27C). Thus by eliminating either type of formins in simulations that use the standard parameter set leads to a decrease in the number of the cables in the mother but does not significantly change the thickness of cables in either the bud or mother, consistent with the experimental observations described in the previous paragraph.

4.3.4 Increased Bnr1 polymerization rate reproduces actin cable defects observed in *smy1Δ* cells

We next performed simulations varying the Bnr1 polymerization rate from 0.6 to 1.0 μm/s, to compare to the phenotype of *smy1Δ* cells (Figure 28A). The myosin passenger protein Smy1 is transported along actin cables towards the barbed ends where it interacts with Bnr1 and decreases the filament elongation rates, serving as a "damper" to detect cable length and prevent cable overgrowth (Chesarone-Cataldo *et al.*, 2011b). Experimental observations (Figure 28B) show that in *smy1Δ* cells, actin cables are abnormally long and wavy (Chesarone-Cataldo *et al.*, 2011b). A clear observation from simulation projection snapshots is that increasing Bnr1 rate results in a denser actin cable network with more interconnected cables (Figure 28A). It also results in cables that are highly curved with abrupt turns and bends. We manually counted the bends and turns where the change in direction is greater than 60° and found that the number of bends increases from 0.28 to 4.78 (Figure 28C). This is further confirmed by measuring the cable curvature that increases from 0.54 ± 0.03 to 0.65 ± 0.04 μm^{-1} (Figure 28D). These

results agree with the experimental observations of *smy1Δ* cells showing more occurrences of cables that change direction more than twice (Chesarone-Cataldo *et al.*, 2011b) (Figure 28B). The wavy cable structures partly at high polymerization rates, partly because filaments grow longer and thus their thermal relaxation time becomes longer than their lifetime (the severing aging time). The longer filaments at high polymerization rates are also forced to curve when reaching the bottom part of the mother.

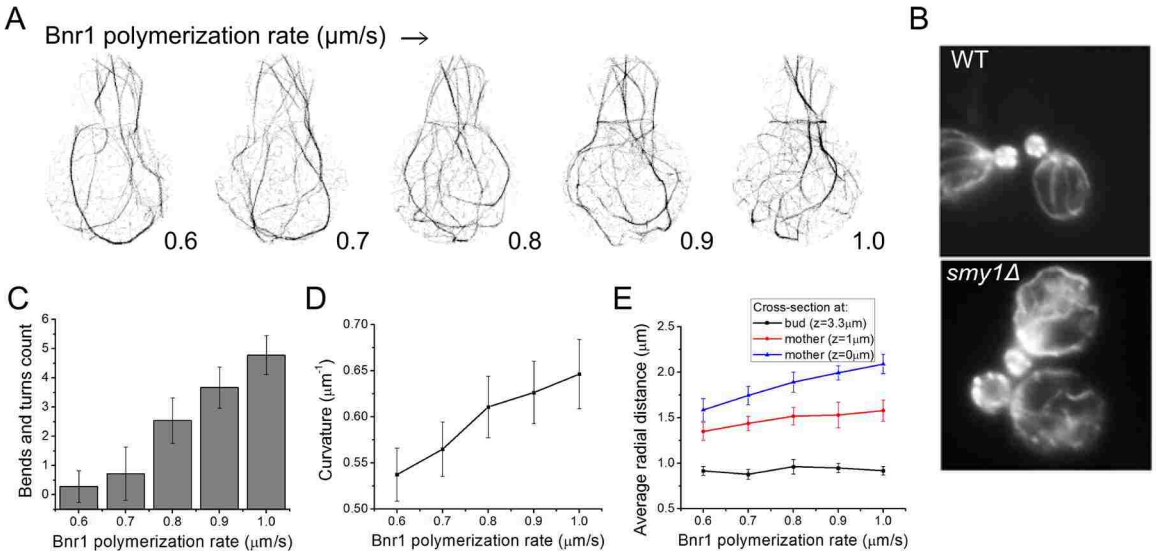

Figure 28. Increase of Bnr1 polymerization rate in simulations reproduces phenotype of smy1Δ cells. (A) Projection snapshots taken at 80 s (as in Figure 2C) as a function of increasing Bnr1 polymerization rate show an increase in cable curvature. (B) Experimental images of phalloidin-labeled actin cables adapted from (Chesarone-Cataldo *et al.*, 2011b). The smy1Δ cells show long and more curved actin cables compared to wild type. (C) Number of cable bends and turns as a function of Bnr1 polymerization rate (manual counting using simulation projection snapshots). Data: 15 time points starting at 50 s, separated by 5 s from 3 independent runs (same for D, E). Error bar is one standard deviation. (D) Average curvature increases with increasing polymerization rate. (E) Average radial distance (measured from the axis that runs through the

centers of mother and bud) of actin filaments as a function of Bnr1 polymerization rate. The average radial distance increases with increasing Bnr1 polymerization rate below the neck (z = 1 μm) and in the bud (z = 3.3 μm). No significant change for cross-section at the bud center (z = 0 μm).

An implication of the actin cable network becoming denser and more curved is that the actin cables buckle and explore more space perpendicularly to the bud-mother axis. Inside the mother cell, at z = 1 μm (below the neck above the mother center), the average radial distance measured from the center of a horizontal cross-section increases from 1.35 ± 0.10 μm (average±StDev) to 1.58 ± 0.12 μm at the highest Bnr1 polymerization rate. At z = 3 μm (through mother center) it increases from 1.59 ± 0.12 to 2.09 ± 0.11 μm (Figure 28E). The average radial distance does not change in the bud that contains very few Bnr1 filaments.

4.3.5 Change in simulated myosin pulling density and location alters actin cable structure

Previous simulations of fission yeast actin cables (Tang *et al.*, 2014), which implemented type V myosin pulling along actin filaments, reproduced the highly curved actin cables near the two cell tips that fail to span the cell, as in myosin V deletion mutants (Lo Presti *et al.*, 2012). The type V myosin Myo2 is an essential protein in budding yeast. Thick actin cable bars were observed in the temperature sensitive *myo2-66* mutants (Johnston *et al.*, 1991), indicating a role of Myo2 in actin cable organization. However, no significant

change of actin cytoskeleton structure was observed for the same mutants in (Schott *et al.*, 1999; Yu *et al.*, 2011).

To explore the role of type V myosin, we varied the density of simulated myosin walkers along actin filaments, similarly to what was done for fission yeast (Tang *et al.*, 2014) (Figure 29). The first observation is that the actin cables become unbundled and straighter as the myosin density, ρ_{MyoV}, is changed from 0 to 5 μm^{-1} (Figure 29A). The absence of myosin V pulling occasionally leads to ring formation around the neck (Figure 29A), which we discuss in more detail in the subsequent section. The average cable number first increases from 4.7 (no myosin pulling), peaks at 6.3 and then decreases to 1.7 as ρ_{MyoV} is increased (Figure 29B). The cable thickness, by contrast, monotonically decreases with increasing ρ_{MyoV}, by nearly two-fold (Figure 29C). The last two results suggest that unbundling at high ρ_{MyoV} consists of two phases: first, unbundling of fewer thick cables into thinner cables and second, unbundling of thin cables into individual filaments. The average curvature decreases from 0.76 to 0.4 μm^{-1} as a result of stiffening accompanied by myosin walking (Figure 29D). Myosin V also causes the tensile force to increase in all Bni1, Bnr1 associated and free filaments (Figure 29E).

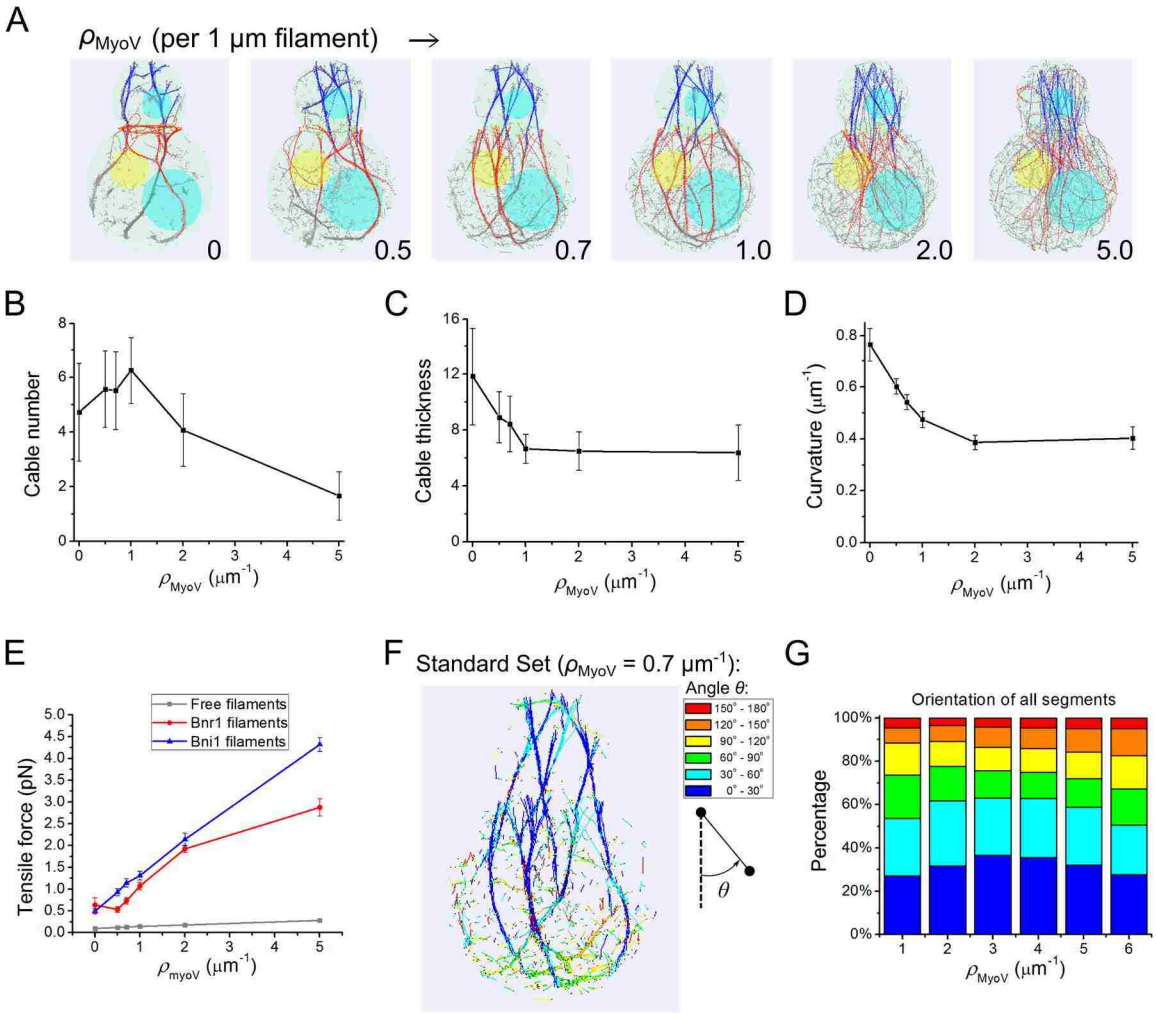

Figure 29. Myosin V pulling stretches actin filaments and influences bundling into cables in simulations. (A) Snapshots at 60 s with increasing myosin V density ρ_{MyoV}. Filaments become unbundled and straighter along with ρ_{MyoV} increase. (B-E) Effects of myosin V pulling on cable number (B), thickness (C), average curvature (D) and tensile forces of Bni1, Bnr1 and free filaments segments (E). The number of cables goes through a maximum while filaments get stiffer, thinner and more tense as the myosin V density increases. All error bars are standard deviations from 15 time points (separated by 10 s starting at 60 s) of 3 independent runs. (F) Snapshot with standard parameter set (Table 2, ρ_{MyoV} = 0.7 pN/μm) with segments colored according to their barbed-to-pointed end orientation with respect to the z axis. (G) Orientation distribution as a function of myosin V density ρ_{MyoV}. Legends of angle distribution are shown

corresponding to the color codes in F. The degree of filament alignment goes through a maximum, similar to the cable number in panel B. Data: average from 15 time points (separated by 10 s starting at 60 s) of 3 independent runs.

We further characterized the effect of simulated myosin V pulling on actin filament segment orientation distribution. Figure 29F shows the actin filament segment orientation distribution colored according to the angle with respect to the vertical axis (cooler colors represent segments with barbed end pointing up). This figure shows that actin filament segments mostly point upwards when they are part of actin cables, except for filaments near the bottom where the cables bend and for free filaments in the cytoplasm that have a very broad distribution of orientations. As function of $\rho_{\mathrm{MyoV},}$, the vertical polarity of actin filament segments first increases then decreases. This is due to the fact that at low ρ_{MyoV} increased pulling orients and stiffens the actin cables while at high ρ_{MyoV} increased pulling unbundles filaments from cables, leading to less cooperative orientation.

Since type V myosin binds to the cortical endoplasmic reticulum (ER) (Du *et al.*, 2004), another possible role of type V myosin is to displace actin cables closer to the cell cortex. We find that assuming an enhanced density of motors on the cell cortex can pull the cables closer to the cell membrane (Figure 30).

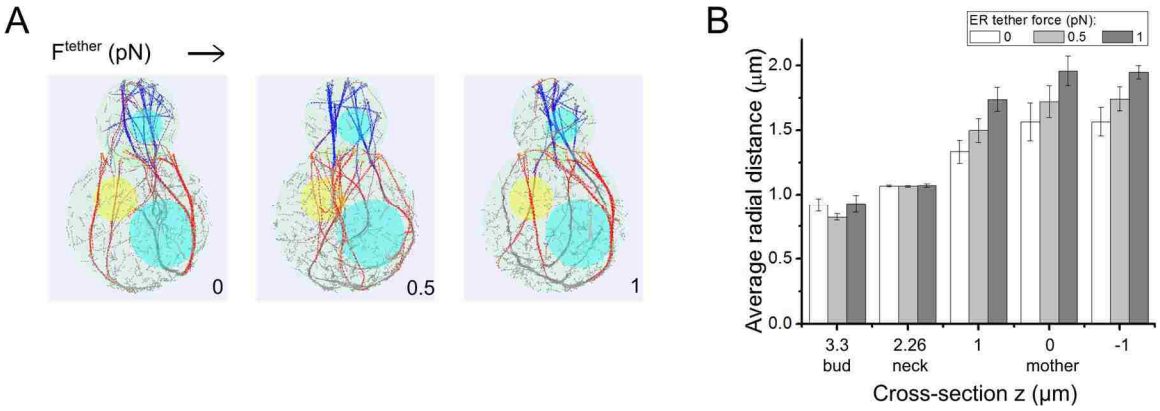

Figure 30. Simulation of the effects of interaction of actin filaments with type V myosin tethered to the cortical Endoplasmic Reticulum (ER). This effect was implemented by assigning an outward pulling force exerted on filament beads that are close to the mother cell boundary. (A) Simulation snapshots showing the effect of an increase of tethering force. The actin cables in the mother cell get pulled closer to the boundary. (B) Graph showing increase of average radial distance of actin filaments showing that the cables get pulled closer to the plasma membrane due to ER tethering in the mother cell (cross-section at *z* equal to 1, 0, -1 μm).

The effects of Myo1 pulling at the bud neck were also explored. Figure 31 shows that the Bni1-associated filaments go through the neck very close to neck boundary using the standard parameter set (see cross-section at the neck at lower panel). Elimination of the short-range attraction toward the neck and of the Myo1 pulling forces causes the Bni1-associated filaments to cross the neck through the middle (Figure 30A). These results suggest that Myo1 plays a role in organizing actin cables to provide a complete track for successful transport of secretory vesicles and organelles towards the bud.

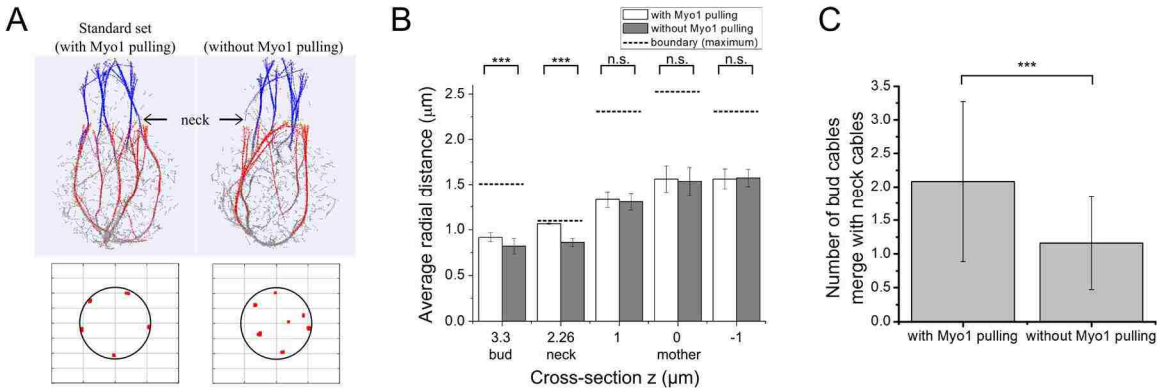

Figure 31. Simulated binding and Myo1 pulling at the neck connects Bni1 associated cables with Bnr1 associated cables. (A) Simulation snapshots of actin cable structures with or without neck binding and Myo1 pulling. Cell boundary, nucleus and vacuoles are not shown. (Lower) Cross-section cut at the neck (z = 2.26 μm) shows the distribution of actin filaments crossing the plane (circle: neck boundary). The neck forces attract the actin cables at the neck area towards the neck boundary. (B) Average radial distance of actin filament beads for five cross-sections (z = 3.3, 2.26, 1, 0, -1 μm) in the bud, at the neck and in the mother cell (dashed lines show the maximum possible radius at each z, ***: p < 0.001, n.s.: not significant). The effect of Myo1 pulling is significant for actin cables at the neck and in the bud, but not in the mother cell. (C) Number of cables in the bud that extend to the mother and merge with the neck cables. Significantly more bud cables connect with neck cables with Myo1 pulling. All error bars in the figure are standard deviations from 15 data points, separated by 10 s starting at 80 s, from 3 independent runs.

4.3.6 Formation of actin ring at the bud neck with increased bud neck binding

The computational model can also demonstrate how cells build an actin ring at the bud neck for cytokinesis using the same formins that they also use to build actin cables. The process of ring assembly is known to depend on dynamic actin filaments nucleated by Bnr1 and Bni1 (Tolliday *et al.*, 2002) (both of which localize to the bud neck during the

M phase), binding of actin filaments to Myo1 and IQGAP-like Iqg1/Cyk1 (Bi *et al.*, 1998b; Shannon and Li, 1999; Bi and Park, 2012), and possibly directly to septins at the bud neck (Mavrakis *et al.*, 2014). The ability of the model to generate rings is already apparent in Figure 28A (highest Bnr1 polymerization rate) and 6A (no Myosin V pulling force). In both cases there is an enhanced concentration of actin filaments near the bud neck as compared to the standard parameter cases. The attraction of these filaments to bud neck results in bundle formation around the neck.

To better illustrate how the association of actin filaments to the bud neck may help in ring formation for cytokinesis, in Figure 32 we varied the force pulling actin filaments towards the bud neck but left the Myo1 pulling force towards the barbed end unchanged. In these simulations we did not include formins at the bud tip and did not include pulling by myosin V motors. To compare to the preceding results on actin cable formation, all other parameters such as cell shape and number of formins at the bud neck, including the polymerization rate at the bud neck, were unchanged as compared to Table 2 (here polymerization at the neck represents a combination of Bni1 and Bnr1 polymerization).

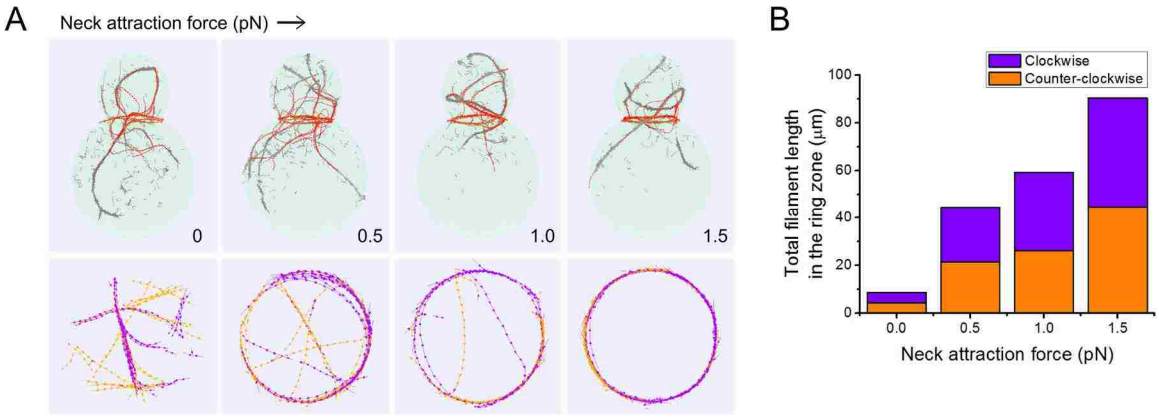

Figure 32. Increase of attraction of actin-filament to the neck region produces a ring of antiparallel filaments at the bud neck. (A) Snapshots of simulations without Bni1 and myosin V pulling taken at 180 s, as function of force of attraction to the bud neck region. Bottom row shows actin filaments colored in orange and purple depending on their clockwise or counter-clockwise direction at a cross section of thickness 0.4 μm at the bud neck. As the neck attraction force is increased, the actin filaments at the bud neck are able to form a ring of antiparallel filaments drawn from filaments that would otherwise form parallel actin cable structures. (B) Total filament length in the ring zone (sum of all the filament segments) characterized by their directions (purple: clockwise, orange: counter-clockwise) as a function of neck region outward attraction force. Data: average from 15 time points (separated by 10 s starting at 120 s) of 3 independent runs.

Figure 32A shows that in the absence of attractive interactions with the neck, the actin filaments that nucleate at the bud neck form cables, extending towards both the bud and mother cell. The concentration of actin filaments segments is higher at the bud neck, however without neck pulling, they form bundles of parallel filaments oriented along random directions (see cross-section at bottom of Figure 32A). With increasing neck attraction force, actin filaments align along the bud neck, forming a ring that is a bundle of antiparallel filaments (Figure 32B). The formation of a ring results in a smaller number

of filaments in cables, which can coexist with the ring structure, consistent with images of cells with both actin rings and cables (Amberg, 1998).

The simulations of Figure 32 show that tuning of the strength of interactions with the bud neck may be one of the main controls for ring assembly, following the removal of Bni1 from the bud tip. This is consistent with recent findings showing premature formation of rings in cells with nonphosphorylatable Iqg1/Cyk1 mutants that cause Iqg1/Cyk1 to arrive prematurely at the bud neck (Naylor and Morgan, 2014). The ability of filaments to maintain antiparallel bundles relies on the use of parameters for r_c and k_c that correspond to dynamic cross-linking among filaments. Implicit in our model of ring formation is that the interactions between actin filaments and the bud neck are also dynamic, allowing filaments attached with their barbed ends at the neck, to slide around the neck as they polymerize.

4.4 Discussion

The computational model in this work shows how actin cable and actin ring morphologies can arise in budding yeast through the combination of a few key interactions that take into account cell shape, nucleation geometry, motor pulling, cross-linking and turnover. The simulations highlight the degree of complexity and robustness of a system that depends on these processes. Since many regulatory proteins determine cytoskeletal interactions, the parameters of the model represent effective rate constants whose detailed dependence on molecular mechanism remains to be examined in more detail in future work. Having a model with enough elements to reproduce main

experimental features of actin cables and rings is however crucial in interpreting the results of genetic and pharmacological perturbations. We were for example able to use the model to interpret actin cable structures in cells lacking Bni1, Bnr1, and Smy1.

We did not consider the kinetics of actin patches, focusing instead on actin cables and rings. Future modeling work that accounts for all three structures should help clarify the effect of global changes in actin turnover and cross-linking. For example, deletion of cofilin is lethal but a temperature sensitive mutation of Cof1 disrupts actin cables and generates enlarged actin patches (Lappalainen and Drubin, 1997). Cells lacking Cap2, the β subunit of capping protein show diminished cable staining (Amatruda *et al.*, 1990). Tropomyosin decorates and stabilizes actin filaments, and some tropomyosin mutants result in loss of actin cables (Liu and Bretscher, 1989; Liu and Bretscher, 1992; Okada *et al.*, 2006). Some of these observation may reflect the competition among actin cables, actin rings with actin patches for the same pool of actin and associated protein (Gao and Bretscher, 2008; Burke *et al.*, 2014).

Dynamic crosslinking in the model promotes actin cable formation, which is consistent with the requirement of fimbrin Sac6 for formation of normal actin structures (Adams *et al.*, 1991; Karpova *et al.*, 1995) and the lethality of Sac6 overexpression (Sandrock *et al.*, 1999). Clustering of formins at the polarisome complex at the bud tip and possible clustering of Bnr1 at the bud neck also helps formation of actin cables (Tang *et al.*, 2014).

The simulations further suggest that pulling by type V myosins helps organize the actin cables and that there exists an optimal density of pulling forces for cable formation. In

simulations lacking myosin V pulling, actin cables become more bundled and curved, similar to prior simulations and experiments of myosin V deletion mutants in fission yeast (Lo Presti *et al.*, 2012; Tang *et al.*, 2014). Deletion of Myo2 is lethal for budding yeast. Overexpression of either Myo2 or Myo4 leads to cell morphological defects independent of the motor domain (Haarer *et al.*, 1994). Use of a temperature sensitive cell mutation *myo2-66*, which is defective in actin-binding has been reported to lead to thick actin bars in (Johnston *et al.*, 1991) but not in (Schott *et al.*, 1999; Yu *et al.*, 2011), possibly a result of different strain background and growth conditions (Schott *et al.*, 1999). In our simulations without myosin V pulling, the actin cables are thicker (50% increase than standard set), which may related to the thick bars of (Johnston *et al.*, 1991), while the cable number is not changed significantly.

We further modeled type II myosin pulling at the bud neck. We predict that Myo1 helps connect actin cables in the bud with those in the mother, consistent with experiments showing that Myo1 contributes to robustness and polarity of actin cables (Huckaba *et al.*, 2006; Gao and Bretscher, 2009) (however we did not account for the changes in polymerization rate by Myo1 pullings. We also provide computational evidence that during ring formation, Myo1 motor activity may contribute to actomyosin ring formation by binding keeping the filaments close to the bud neck (together with Iqg1/Cyk1), consistent with the role of Myo1 in ring assembly (Bi and Park, 2012). Actin and myosin dynamics may change during ring constriction when actin filament have been reported to become less dynamic and Myo1 motor activity is dispensable for constriction (Lord *et al.*, 2005; Mendes Pinto *et al.*, 2012).

The actin filaments within cables in our simulations are relatively long: the filament segments attached to formins have lengths of order microns, comparable to the total length of actin cables. Electron microscopy studies suggest that cables consist of many short actin filaments (Kamasaki *et al.*, 2005) though studies of cable depolymerization in latrunculin A indicate the existence of long filaments (Karpova *et al.*, 1998). A better understanding of the severing mechanism by cofilin and cofactors such as Aip1 and tropomyosin would help in modifying the model to account for the length distribution within bundles. Filament severing may change the filament sliding kinetics within cables and rings that our study suggests is important for formation of mixed Bni1/Bnr1 cables and for formation of a ring of antiparallel filaments.

The cortical ER is associated with actin cytoskeleton (Fehrenbacher *et al.*, 2002) and its inheritance in budding yeast cell is achieved through type V myosin transport on actin cables (Estrada *et al.*, 2003; Du *et al.*, 2004; West *et al.*, 2011; Rowland and Voeltz, 2012). We tested the ER tethering effect by adding an outward pulling force for filaments come close to the cortical sites in the mother cell (Figure 30A). Such pulling forces help actin cables to organize closer to the cell cortex (Figure 30B).

In this study we did not account for the turnover of formins, which is faster for Bni1 as compared to Bnr1 (Buttery *et al.*, 2007). In addition to increasing fluctuations in filament length and cable thickness, these processes may also enable faster global restructuring of the actin cables through the cell. Similarly, we did not explicitly account for the activation/inactivation of Bnr1formins by Bud14 that displaces the Bnr1 FH2 domain

from the barbed ends and thus influences filament length and actin cable structures (Chesarone *et al.*, 2009).

Finally, in the following paragraphs we compare the mechanisms for actin cable and contractile ring formation between budding yeast and fission yeast as suggested by computational modeling. In simulations of fission yeast, actin filaments polymerizing out of the cell tips by For3 can meet at the cell center where they can establish straight bundles of antiparallel filaments when cross-linking interactions are dynamic enough to allow polymerizing filaments to slide past one another (Tang *et al.*, 2014) and Chapter 3. By contrast, simulated actin cables in budding yeast are mostly bundles of parallel filament. Dynamic cross-linking still helps the formation of straight bundles containing filaments polymerizing at different rates from two different formins (Bni1 and Bnr1).

Unlike budding yeast where the site of ring formation is marked by septins at the bud neck, fission yeast needs to define the site of the contractile ring prior to cytokinesis. This process depends on the formation and condensation of a broad band of nodes that contain anilin Mid1, type II myosin Myo2, and formin Cdc12 (Lee *et al.*, 2012). Computational modeling suggests a process for broad band condensation through search, capture, pull and release and dynamic filament cross-linking that allows filaments to align in antiparallel bundles (Vavylonis *et al.*, 2008; Bidone *et al.*, 2014) and Chapter 5. An alternative model envisions contractile ring formation as a process of actin cable closure followed by remodeling of actin filaments within the cable (Kamasaki *et al.*, 2007). In practice, these two mechanisms may coexist, reflecting the fluctuations of a

finite system that is able to assemble both parallel and antiparallel bundles and transition between these two structures (Bidone *et al.*, 2014) and Chapter 5.

Since budding yeast can place its formins and Myo1 at the septin ring, its additional task in terms of ring formation is the alignment of actin filaments around the bud neck. Here we suggest that tuning of the association of actin filaments (and possibly reducing myosin V pulling) may be sufficient to reorient actin filaments and establish a bundle of antiparallel filaments, provided cross-linking interactions among actin filaments are sufficiently dynamic. Time lapse movies of simulations shows that the ring is formed by polymerization and aligning of filaments in a uniform manner around the ring, however cable features and cable merging into the ring are also observed. This suggests a process for ring formation as in fission yeast, but without the node condensation episode.

Since the polarity of actin filaments bundles is closely related to their biological function, progress in understanding mechanistic aspects of cytoskeletal assembly mechanisms in yeast should provide insight to cytoskeletal remodeling and associated biological function across many species.

Chapter 5 Cytokinetic Ring Model

We extended our 3D fission yeast actin cable model (Tang *et al.*, 2014) and previous "search, capture, pull and release" (SCPR) model (Vavylonis *et al.*, 2008; Laporte *et al.*, 2012) to describe the fission yeast cytokinetic ring in 3D. My colleague Tamara Bidone made the major contribution and I helped in extending the code, developing the numerical model and visualization. The work is published on Biophysical Journal (Bidone *et al.*, 2014).

5.1 Introduction

Cytokinesis in fungi and animal cells requires self-organization of a medial contractile ring of dynamic actin filaments, myosin motors and associated proteins to cleave a mother cell into two daughter cells (Eggert *et al.*, 2006; Pollard and Wu, 2010; West-Foyle and Robinson, 2012). In the fission yeast, the cytokinetic ring assembles from a broad band of membrane-associated node complexes, which bind myosin II molecular motors and Cdc12 formins. The nodes condense into a narrow ring in a process that depends on actin polymerization and lasts about 10 minutes (Lee *et al.*, 2012; Mishra *et al.*, 2014).

Consistent with a process of ring assembly through a broad condensing actomyosin network, changes in the dynamics of actin filaments during ring formation lead to delayed ring assembly or formation of non-functional actomyosin structures, such as clumps, extended meshworks and double rings. Increase in the concentration of actin

filament cross-linkers alpha-actinin Ain1 and fimbrin Fim1 leads to extended actomyosin meshworks, while deletion of Ain1 with simultaneous reduction of Fim1 concentration leads to clumps (Laporte *et al.*, 2012) (Figure 33A). Mutations that impair Cdc12-mediated actin polymerization lead to node clumps (Hachet and Simanis, 2008; Coffman *et al.*, 2013). In cells where the cofilin Cof1 severing activity is compromised by mutations, nodes coalesce into multiple clumps instead of a ring (Chen and Pollard, 2011).

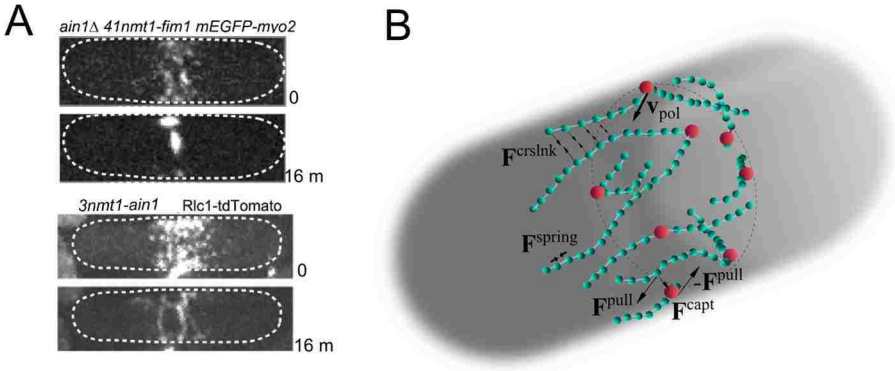

Figure 33. Experimental images of fission ring assembly and cartoon of computational model.. (A) Example of nodes condensing into clumps and meshworks instead of rings in mutant cells. Top: Myo2-labeled nodes condensed into a few clumps after 16 m in cell lacking α-actinin Ain1 and depleted fimbrin Fim1. Bottom: In cells overexpressing Ain1, nodes condensed into a meshwork after 16 m. (C) Cartoon of 3D model (nodes in red; actin filaments in green), with arrows indicating forces imposed during the ring assembly process. To illustrate force vectors, nodes and filaments shown at low density.

The interplay between actin filament polymerization, myosin motor activity, severing and cross-linking interactions in the morphology of the condensing actin network has been

previously characterized theoretically using SCPR (Vavylonis *et al.*, 2008; Laporte *et al.*, 2012). One of the aims of this study is to test if a 3D model based on the SCPR mechanisms can lead to star/cable morphologies during contractile ring assembly, in addition to the other morphologies described before, as observed in(Arai and Mabuchi, 2002).

The previous SCPR models (Vavylonis *et al.*, 2008; Laporte *et al.*, 2012) were developed in 2D which represent the cortical cell membrane surface, where membrane-bound node component Mid1 accumulates in nodes and recruits myosin Myo2 and Cdc12 (Laporte *et al.*, 2011). However how the actin filaments that reach 0.5-2 μm in length become parallel and tightly packed to the cell membrane has not been resolved. It was proposed that the cortical ER that influences Mid1 distribution (Zhang *et al.*, 2012) may also confine actin filaments near the membrane by restricting their motion (Pollard and Wu, 2010). Alternatively, binding of actin filaments to Myo2 as well as to one another, through cross-linkers, could be a mechanism for confinement. The second aim of this chapter is to use a 3D model to predict profiles of cortical density of the actin filaments under different conditions of myosin and cross-linker activities and to relate them with the resulting network morphologies.

Prior modeling did not address the buildup of cortical tension during cytokinetic ring assembly. The magnitude and direction of the microscopic tensions acting on filaments and cortical node complexes depends on the morphology of the condensing actin filament network and the activity of regulators of actin dynamics such as myosin pulling and cross-linking. The third aim of this study is to identify patterns in the evolution of

microscopic forces during contractile ring assembly, and to relate them with network architecture.

In order to address the above mentioned aims, here we extend the previous 2D SCPR model of cytokinetic ring assembly (Laporte *et al.*, 2012) to 3D (Figure 33B). Results from the 3D model show that: (*i*) the model parameter space leading to final ring morphologies is near parameter regions that result in cables/stars, networks, and clumps; (*ii*) confinement of actin filaments against the cell cortex can occur just by filament turnover, myosin capturing and cross-linking interactions, with no need for additional mechanisms, such as confinement by the ER or adhesion of actin filaments at the membrane; (*iii*) in early stages of ring formation, forces acting on the cortical nodes help narrow the broad band, whereas at later stages, they re-orient towards the cell interior and can subsequently aid in ring constriction.

5.2 Computational Model

We extended a prior 2D model (Laporte *et al.*, 2012), using methods of actin cable formation in non-dividing yeast (Tang *et al.*, 2014) (Chapters 3, 4 and Figure 33B). The computational domain was a tube with radius R = 1.74 μm and length 13 μm. 65 nodes were initially distributed on the cylindrical boundary, randomly circumferentially and according to a Gaussian distribution with standard deviation σ = 0.9 μm along the cell long axis (Motegi *et al.*, 2000; Vavylonis *et al.*, 2008; Akamatsu *et al.*, 2014). Filament representation, crosslinking, polymerization and boundary condition are realized similar to our actin cable model (Tang *et al.*, 2014) and Chapter 3.

Capturing of actin filament beads that passed within 0.1 μm from a node was established by a harmonic interaction potential with spring constant 2.5 pN/μm and equilibrium length 0 μm. Upon establishing a connection, the node exerted an additional tangential pulling force on the filament bead $F_{\mathrm{myo}}^{0} = 4$ pN, toward the barbed end of the captured filament. To satisfy force balance, an equal and opposite force was exerted on the connected node. Nodes could establish only one connection with the same filament but were able to connect with many filaments. To limit the magnitude of pulling force when nodes connect with bundles of actin filaments, the pulling force on each connected bead was $F_{\mathrm{myo}} = \mu F_{\mathrm{myo}}^{0}/N_c^2$, where $\mu = 0.3$ and N_c is equal to the number of filament beads cross-linked to the captured bead, when $N_c > 3$. This reduction in force represents the distribution of myosin force over many filaments in the bundle and the interference of myosin activity with actin cross-linkers. Here we used a stronger dependence of F_{myo} on N_c compared to (Laporte *et al.*, 2012), however our results are not influenced by this choice. To avoid node overlap, nodes were subjected to exclude volume interactions: when the centers of two nodes were closer than 0.2 μm, a repulsive radial force of magnitude 50 pN was applied. The position of a node, $\mathbf{r}_{\mathrm{node}}$, was found by solving $d\mathbf{r}_{\mathrm{node}}/dt = \mathbf{F}_{\mathrm{node}}^{\mathrm{total}}/\zeta_{\mathrm{node}}$, where the node drag coefficient was $\zeta_{\mathrm{node}} = 400$ pN s/μm (Vavylonis *et al.*, 2008). The total force on the node, $\mathbf{F}_{\mathrm{node}}^{\mathrm{total}}$, is the sum of (*i*) elastic forces transmitted through filaments polymerizing out of the node; (*ii*) forces due to the elastic spring that connects the node captured actin filament beads; (*iii*) forces that balance node pulling on actin filaments; (*iv*) excluded volume interactions.

Langevin dynamics was used to update the positions of actin filaments and nodes.

$$\mathbf{F}_i^{spring} + \mathbf{F}_i^{bend} + \mathbf{F}_i^{thermal} + \mathbf{F}_i^{crslnk} + \mathbf{F}_i^{myo} + \mathbf{F}_i^{capt} = \zeta_b d\mathbf{r}_i/dt \qquad (24)$$

5.3 Results

5.3.1 The 3D model reproduces cytokinetic ring assembly

The 3D model reproduced assembly of a narrow ring of actin filaments and nodes, through condensation of nodes initially distributed within a broad band of width 1.8 μm (two times the standard deviation of node distribution), along a cylindrical surface (Figure 34A, B).

We verified that our model reproduces the features of prior 2D models based on the SCPR mechanism (Vavylonis *et al.*, 2008; Laporte *et al.*, 2012) that were used to compare them to experimental observations. In Figure 33, the broad band of nodes condensed in about 10 minutes and the distribution of node velocities at the onset of ring assembly (1 min) ranged between 0 and 40 nm/s, consistent with experimental observations (Vavylonis *et al.*, 2008; Laporte *et al.*, 2012). A connection between two nodes by a single filament corresponds to 10 nm/s so this distribution reflects nodes connected with one another through variable numbers of actin filaments. The average node velocity decreases with time (Figure 34C), a result of (*i*) cancelation of forces pulling in opposite directions circumferentially, (*ii*) increasing excluded volume interactions that prevent node overlap, and (*iii*) increasing cross-linking interactions among filaments.

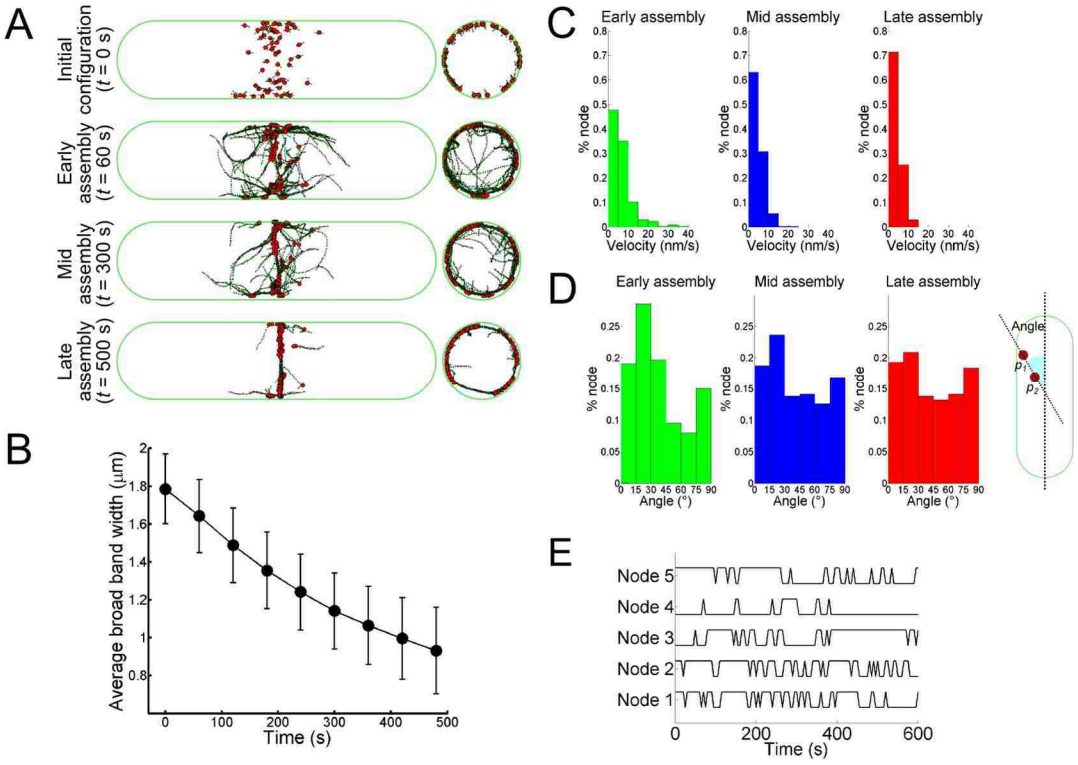

Figure 34. The model reproduces ring assembly through intermittent motion of nodes. (A) Representative simulation results in top and cross-sectional views (radius: 1.74 μm) of cortical nodes (red) and actin filaments (dark green) at 0, 60, 300 and 500 s. (B) Width of broad band of nodes versus time (n = 12 simulations, error bar: standard error). The average broad band width at 480 s includes lagging nodes and tilted rings and is wider than the width of the main ring bundle in panel A. (C) Histograms of node velocity distributions at early, mid and late ring assembly (n = 5 simulations). Velocities were calculated by measuring displacement over 1 s. (D) Histogram showing distribution of cortical node directions, relative to the long cell axis, at early, mid and late ring assembly (n = 5 simulations). The cartoon shows how the angle is computed, where p_1 and p_2 are consecutive positions of a node moving towards the cell equator. (E) Graph showing start-stop node motion. Individual node motion in different simulations was discretized into a series of moves (velocity > 1 nm/s) and pauses (velocity < 1 nm/s). Upper (bottom)

horizontal lines represent moves (pauses) and vertical lines indicate state switching. Velocities were calculated by measuring displacement over 5 s.

The distribution of node movement direction in simulations was broad, as observed (Vavylonis *et al.*, 2008; Laporte *et al.*, 2012) (Figure 34D): at the onset of ring assembly, about 50% of the nodes moved within 30º from the cell long axis (Figure 34D, cartoon); at later stages of ring assembly about 40% of the nodes moved within 30º from the cell long axis, indicating increase in circumferential movement of the nodes along the cortex, consistent with prior experiments (Laporte *et al.*, 2012).

The 3D model also reproduced features of node motion in experiments, which is characterized by many starts-stops and change of direction of motion (Vavylonis *et al.*, 2008; Laporte *et al.*, 2012). Figure 34E shows node intervals of movement in between pauses. The probability for a node to change direction by more than 15º after a pause was above 50% at all times of ring assembly. The frequency of node starts-and-stops increased with the progression of ring assembly, reaching a plateau at 150-300 s (data not shown).

5.3.2 Network morphology as function of cross-linking properties

We next focused on how actin filament cross-linkers contribute to the organization of actin filaments and nodes in a bundle on the cell cortex. We used a set of three parameters to quantify the morphology of node-filament structures that form when varying parameter values of the simulations, similar to prior work (Ojkic *et al.*, 2011;

Laporte *et al.*, 2012): width of the node broad band, percent of actin filaments close to the membrane, and 1D porosity. The node band width was computed from the standard deviation σ of node positions along the cell long axis as $w = 2\sigma$. The 1D porosity, a measure of the uniformity of node distribution along the circumferential direction, was computed as the ratio of the sum of the lengths of all circumferential gaps with no nodes to the cell circumference, $2\pi R$.

The above three measures together with visual inspection of the results indicate regions in parameter space that provide different node-filament morphologies after 500 s of simulation time. Figure 35 shows results using the same parameters as in previous figures, but varying cross-linking parameters r_{crslnk} and k_{crslnk} (Tang *et al.*, 2014). The latter are effective parameters representing the combined action of the multiple cross-linkers. When both r_{crslnk} and k_{crslnk} are small compared to the other values tested in Figure 35, the broad band of nodes did not condense towards the cell middle (w remained larger than 1.2 μm) but instead organized into many small clumps. In this case cross-linking is too weak to confine actin filaments along the cortex and thus nodes establish few connections with their nearest neighbors, which results in many clumps (Ojkic and Vavylonis, 2010).

In region marked "few clumps," k_{crslnk} is high enough to allow partial confinement of actin filaments and condensation; however overall cross-linking is still too weak to align nodes and filaments into a bundle, which results in few clumps. Using $r_{\text{crslnk}} \sim 0.12$ μm and $k_{\text{crslnk}} \sim 1$ pN/μm results in ring formation. The results of Figure 34. For r_{crslnk} higher than 0.15 μm and $k_{\text{crslnk}} \sim 1$ pN/μm generates meshworks due to premature formation of bundles, which often consisted of double rings. This transition from clumps to rings to

meshworks for k_{crslnk} around 1 pN/μm is similar to the results of the 2D model of ref. (Laporte *et al.*, 2012) and experimental observations of cells with varying concentrations of cross-linkers (Laporte *et al.*, 2012). However here we show that this occurs when parameters allow partial filament confinement on the cell membrane and that this confinement is weaker in the clump region.

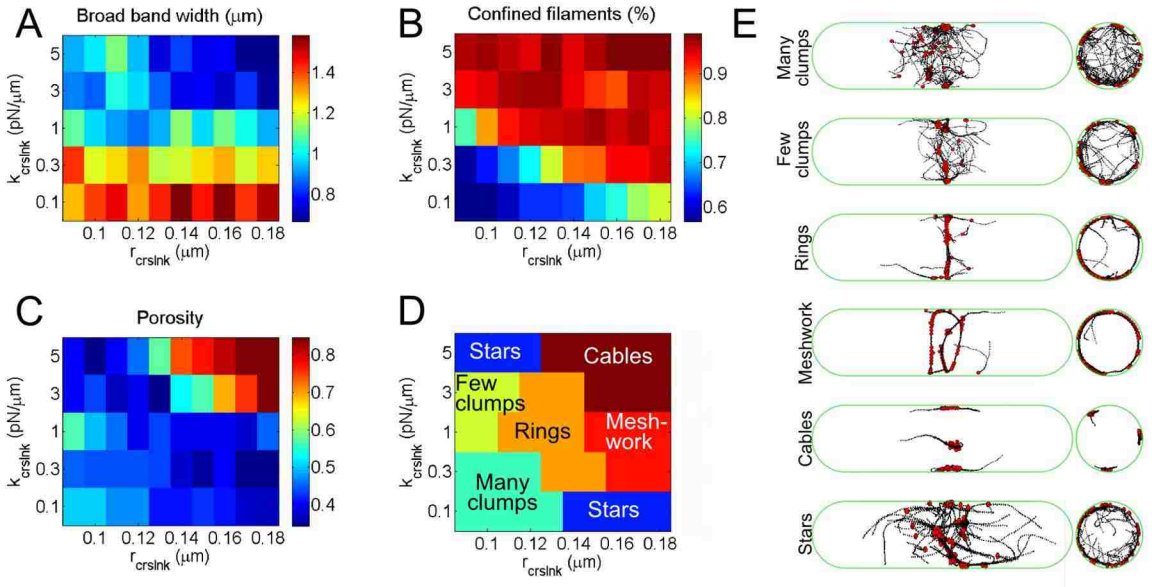

Figure 35. Dependence of the node-filament aggregate structures on cross-linker model parameters. (A-C) Width of the node broad band, percentage of actin filaments within 0.29 μm from cell boundary, and porosity as a function of r_{crslnk} and k_{crslnk}, calculated at 480-500 s after the start of the simulations (mean values of 8-12 runs). (D) Summary of regions of different morphologies based on the preceding panels and visual inspection. (E) Representative images of top and cross-sectional views of the detected morphologies: many clumps, few clumps, rings, meshworks, cables and stars. Nodes, actin filaments and cell boundary represented in red, black and green, respectively.

In two regions of parameter space of Figure 35, the morphology of the aggregates resembles that of stars, which are transient structures that last 1-5 min. The main difference between clumps and stars is in the organization of the actin filaments: in both cases, node coalesce into disconnected aggregates, however, in stars the actin filaments elongating from the node aggregates formed several bundles of aligned filaments that extended along the cell cortex. The few-clumps region also showed a slightly higher porosity with respect to that of stars (Figure 35C).

For the highest cross-linking parameters in the simulations, only one or two bundles emerge from the node aggregates, resulting in configurations that resemble actin cables. The cables align along the long axis of the cell such that they do not bend during extension. This phase occurred with both high k_{crslnk} (> 1 pN/μm) and high r_{crslnk} (> 0.12 μm). Cables had the maximum density of actin filaments at the cortex (Figure 35B) and maximum circumferential porosity (Figure 35C) with respect to the other simulated actomyosin morphologies.

5.3.3 Impact of myosin motor pulling force on network morphology

Myosin motor pulling works together with actin filament cross-linking to assemble the contractile ring (Laporte *et al.*, 2012). To explore this interplay in 3D, we varied the force per node-filament connection described by parameter F^0_{myo} together with one of the two parameters describing the strength of cross-linking interactions, r_{crslnk}. In Figure 36 we used the same three measures as in Figure 35 to quantify the resulting morphology after 500 s of simulation time.

A minimum amount of myosin pulling was necessary to condense the broad band of myosin nodes towards the cell equator, corresponding to F^0_{myo} ~ 1pN (Figure 36A). This is consistent with the experimental and modeling results in (Laporte *et al.*, 2012) that showed failure of node condensation in *myo2-E1* mutant cells with defective Myo2 motor activity. For such cases, the resulting configuration is an extended meshwork structure, with a varying degree of actin filament confinement along the surface depending on the value of r_{crslnk}.

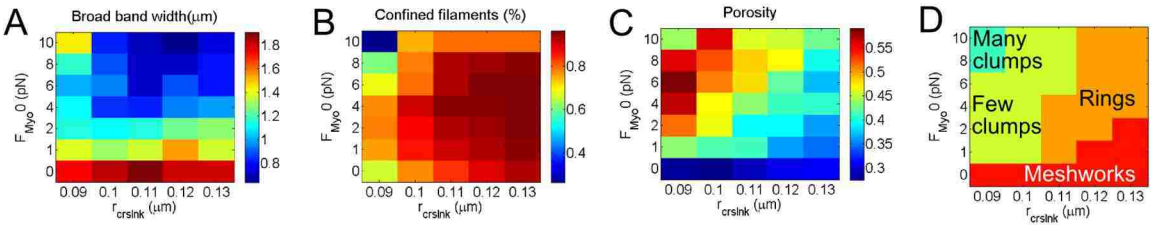

Figure 36. Dependence of the node-filament aggregate structures on myosin pulling and cross-linking**.** (A-C) Width of the node broad band, percentage of actin filaments within 0.29 μm from cell boundary, and porosity as a function of r_{crslnk} and k_{crslnk}, calculated around 500 s after the start

of the simulations (mean values of 8-12 runs). (D) Summary of regions of different morphologies based on the preceding panels and visual inspection.

We find the region of ring formation lies approximately along the diagonal in the parameter space of Figure 36D. Instead of rings, weak cross-linking interactions lead to either a few node clumps or else to many small clumps if the node pulling force is large enough (top left corner in Figure 36D). Sufficiently high cross-linking interactions lead to extended node-filament meshworks instead of rings, which is a result of our assumption that the node pulling force per captured filament decreases with increasing number of cross-links. As cross-linking parameter r_{crslnk} increases above 0.11 μm, a higher value of pulling force F_{myo}^{0} is required for ring formation, to overcome the slowing-down induced by the cross-linking. These results are in agreement with the results in (Laporte *et al.*, 2012), both with the 2D model in this work, as well as with the experimental observations that (*i*) Myo2 overexpression rescues the meshwork phenotype of Ain1 overexpressing cells and (*ii*) Myo2 overexpression results in clumps in cells with deleted Ain1. These results also show that the magnitude of the myosin pulling force provides an additional parameter that cells can use to achieve ring formation, in addition to tuning cross-linking parameters (Figure 35D).

5.3.4 Buildup of tension and filament polarity during cytokinetic ring assembly

To examine how tension builds up for ring constriction during the assembly of the contractile ring, we first studied the tension along actin filaments (Figure 37A). Microscopic tension between consecutive beads of an actin filament was positive or

negative depending on the extension or contraction of the spring connecting the filament beads. Thermal forces produce tension between consecutive filament beads of average magnitude ~0.6 pN, using spring constant 100 pN/μm between filament beads. Compressive forces between actin filament beads arise from formin-induced polymerization and extensive forces from myosin pulling (4 pN for a single captured filament). Cross-link formation and breakage also contributes to the spatially-varying tension distribution shown in Figure 37A, that has a few spots of contractile forces (above 1 pN) at all stages of ring assembly. On average, actin filaments springs are extended, (Figure 37B). The forces on nodes are shown as vectors in Figure 37A. These forces became constricting during ring assembly, pointing towards cell center (Figure 37A).

Nodes pull on actin filaments that form a bundle of filaments of mixed polarity. In Figure 37C, where the actin filaments with a barbed-to-pointed end orientation in the clockwise direction around the cell axis are shown in red, and those in the counterclockwise direction in blue. The development of a bundle of mixed filament polarity depends on filament growth along random directions and intermediate cross-linking strength that allows filaments to align and slide past one another as they polymerize (Figure 35). For the reference parameter values, the average ratio of clockwise-oriented filaments to counterclockwise-oriented ones in the fully assembled ring was 1:1 and remained approximately uniform around the ring. We calculated the total circumferential tension for the reference model parameter values, which increases over time, reading a value of about 4 pN (Figure 35D).

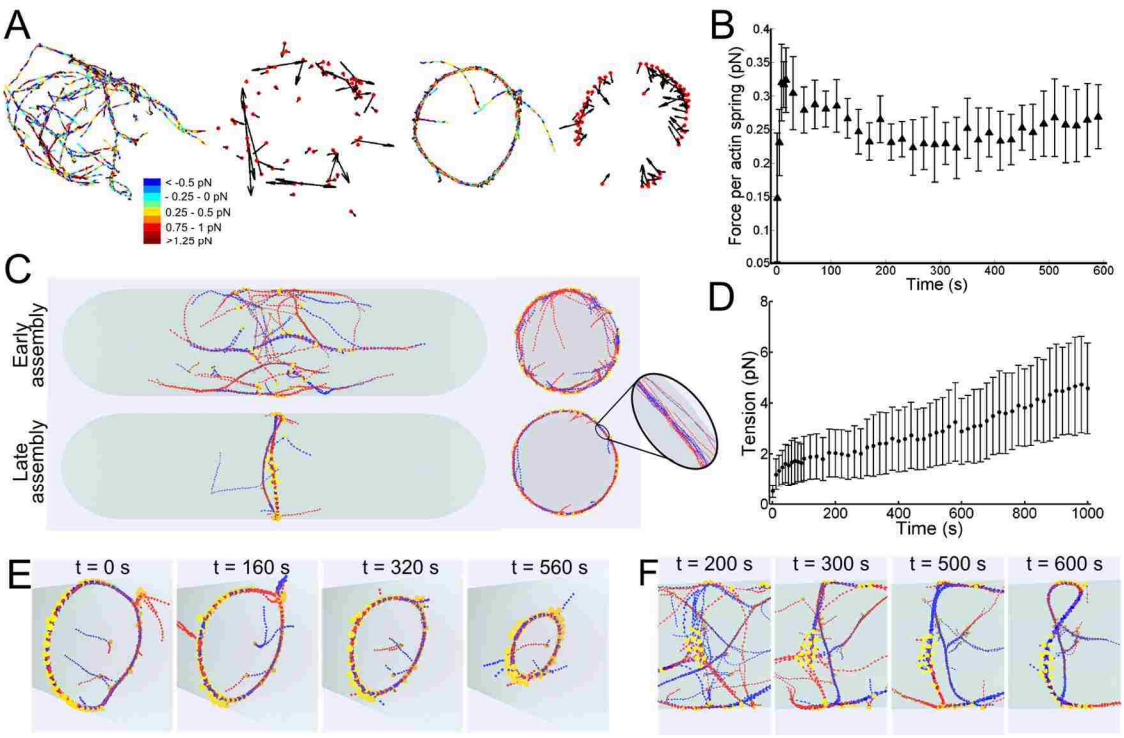

Figure 37. Buildup of tension during ring assembly and polarity of filaments in simulation**.** (A) 3D snapshots of simulations at early and late stages of ring assembly showing actin filament tension distribution with colors representing the spring force between actin filament beads. Positive (negative) values correspond to extension (compression). Arrows: sum of all forces acting on nodes (red circles), excluding boundary force. Node forces become constricting with time. The largest vector magnitude is 11 pN. (B) Average actin filament bead spring force over time (N=7). (C) Assembly of a ring of filaments with mixed polarity. Nodes: yellow. Filaments are colored red (blue) depending on their clockwise (counter-clockwise) barbed-to-pointed end orientation around the cell long axis. (D) Contractile ring tension versus time. N = 7, error bars: Standard deviation. At 600 s, the force that restricts nodes to the cell boundary is set to zero and the ring starts to constrict. (E) Snapshots of constricting ring obtained by setting the force that restricts nodes to lie on the cell boundary to zero. (F) Results of a simulation with cell forming a transient “star” and filaments colored according to orientation as in panel C. A transient star structure is observed at 200 s, which eventually transforms to a ring. At 500 s filaments form polarized parallel bundles

out of a node clump. As the ring closes, the clump disperses and filament polarity becomes mixed around the ring.

The contractile rings of our 3D model constrict if we eliminate the force that keeps the nodes on the boundary after ring assembly (at 600 s). This is shown in Figure 37E, where the nodes were released from the boundary but their drag coefficient was unchanged. When nodes were released from the cell boundary, the ring tension increased as the average distance between nodes decreases and the overlap between filaments and nodes increased (Figure 37D). Without any modification to our model, the resulting rate of ring constriction, ~0.2 μm/min, is of the same order as the experimentally-measured value, 0.3 μm/min (Stachowiak *et al.*, 2014). We note however that this agreement may be the result of underestimating both tension and drag, since the measured tension of contractile rings of fission yeast protoplasts is ~ 390 pN, working against an estimated drag coefficient 55 times larger than the drag due to the precursor nodes (Stachowiak *et al.*, 2014), see Discussion.

Even for the reference parameter values, we occasionally observed transient star-shapes that become rings, as in Figure 37F (Coffman *et al.*, 2009). This panel shows two polarized bundles that emanate from a former star-shaped structure (red, blue bundles at t = 500 s). These bundles connected with other linear structures and formed a ring, which developed into a bundle of filaments of mixed polarity.

5.4 Discussion

In this work, we presented a 3D model of contractile ring assembly, based on the "search, capture, pull and release" mechanism. Our model predicts that confinement of actin filaments against the cell cortex can occur just by filament turnover and crosslinking interactions, with no need for additional mechanisms, such as confinement by the ER or adhesion of actin filaments at the membrane. However, we cannot exclude that additional confining mechanisms contribute to the robustness of ring assembly, by enlarging the region of parameter space where rings can form. The excluded volume of the nucleus, which is located in the middle of the cell at the onset of actin polymerization at the nodes, can play some role in the early stages of ring assembly, which is the stage with the largest fraction of unconfined filaments in the simulations. Experiments imaging actin filament dynamics in 3D can elucidate these aspects. More generally, our 3D model can be related to the dynamics of actin filament confinement at the cortex of non-dividing cells, where formins, actin filaments, cross-linkers and myosin motors localize close to the plasma membrane (Biro *et al.*, 2013; Clark *et al.*, 2013; Luo *et al.*, 2013).

Our work provides general predictions about the morpho-dynamic landscape of the node-filament system during ring assembly, as a function of myosin and cross-linker activities. We found that in the parameter space of the model, the region of ring-assembly is located in between regions where actin filament and nodes coalesce into clumps, meshworks/double rings, or stars. This structure of different morphologies in parameter space likely represents a general feature of the node-filament system, resulting from the underlying mechanisms of tethered actin filament polymerization, actin filament turnover,

transient actomyosin connections, and cross-linking among actin filaments. It may not be possible to change all the model's parameter values independently of one another experimentally, using mutations and pharmacological treatments. However any such perturbations that influence the microscopic mechanisms implemented in the model (polymerization, cross-linking, myosin pulling) should shift the system towards the different morphological regions in a continuous manner. These large scale changes in structure are some of the most reliable predictions of the model since they are less dependent on the precise choice of parameter values.

Chapter 6 Conclusion

The purpose of this research has been to further the understanding of actin cytoskeleton in cells. To achieve this end I developed a 3D computational model of actin cables and actin cytokinetic ring in the model organism yeasts. I started by simulating individual actin filament using a coarse-grained bead-spring model. I tested the mechanical properties including the tangent correlation, relaxation dynamics and equipartition of energy in thermal equilibrium. Simulations with mechanisms of polymerization, crosslinking, motor protein pulling and severing reproduced actin cable structures and supported actin cable formation in the fission yeast system with essential actin associated proteins For3, Fim1, α-actinin, Myo5 and Cof1. Tuning of parameters such as walking force and crosslinking affected actin cable structure and dynamics, generated simulations that are similar to that observed in experiments and made testable predictions. I then studied another yeast system – budding yeast where I have refined the model to have more realistic crosslinking and filament turnover mechanisms. The new model confirmed the experimental study of *Smy1Δ* increases the polymerization rate of Bnr1 nucleated actin filaments, producing long and wavy cables. It also suggested significant roles motor proteins play in polarized cable growth and cytokinesis, where type V myosin walking unbundles and stiffens the cables and type II myosin pulling helps formation of ring and connects bud cables with mother cables. Furthermore, together with my colleague Dr. Tamara Bidone, we extended this model and included the capturing by myosin nodes to simulate the cytokinetic ring assembly.

This work provides a powerful tool to investigate the filamentous structures in the cell system in a quantitative way. The developed model lays the foundation for future studies of more complex systems or studies of physical and mechanical properties in depth. Here I list a few possibilities:

1) There are intensive experimental studies on actin network structures in *in vitro* systems with purified proteins. This can serve as a great reference for us to test our models: how are structures generated from our computational model compared to the experimental observations, how do the simulated outputs relate to the mechanical properties of the experiments, how will the simulated system change when we change the parameters?

2) In the yeast cell systems, actin patches (sites of endocytosis) compete with actin cables over the same actin monomer pool. As can been seen in the CK666 (actin patches depolymerizer) treated fission yeast, actin cables are thicker and more curved. Our model's polymerization rate is constant, which does not consider such competition. Future work should include two states of actin monomers.

3) We simulated the steady state actin cables and the formation of cytokinetic ring. However, how fission yeast tip associated cables dissemble, accumulate at the cell middle and form cytokinetic ring remains a open question. An ambitious future work would be to consider the actin cable dynamics for the complete cell cycle. However, that requires much bigger effort to include factors such as geometry change, diffusion of actin, interaction with other proteins.

To model more complex systems and to study cytoskeletal filaments' physical indications to cell mechanics in depth, our computational work of actin cables in the yeast systems is a good start.

Bibliography

Adams, A.E., Botstein, D., and Drubin, D.G. (1991). Requirement of yeast fimbrin for actin organization and morphogenesis in vivo. Nature *354*, 404-408.

Adams, A.E., Shen, W., Lin, C.S., Leavitt, J., and Matsudaira, P. (1995). Isoform-specific complementation of the yeast sac6 null mutation by human fimbrin. Mol Cell Biol *15*, 69-75.

Akamatsu, M., Berro, J., Pu, K.M., Tebbs, I.R., and Pollard, T.D. (2014). Cytokinetic nodes in fission yeast arise from two distinct types of nodes that merge during interphase. The Journal of cell biology *204*, 977-988.

Alvarado, J., Sheinman, M., Sharma, A., MacKintosh, F.C., and Koenderink, G.H. (2013). Molecular motors robustly drive active gels to a critically connected state. Nature Physics *9*, 591-597.

Amatruda, J.F., Cannon, J.F., Tatchell, K., Hug, C., and Cooper, J.A. (1990). Disruption of the actin cytoskeleton in yeast capping protein mutants. Nature *344*, 352-354.

Amberg, D.C. (1998). Three-dimensional imaging of the yeast actin cytoskeleton through the budding cell cycle. Molecular biology of the cell *9*, 3259-3262.

Andrianantoandro, E., and Pollard, T.D. (2006). Mechanism of actin filament turnover by severing and nucleation at different concentrations of ADF/cofilin. Mol. Cell *24*, 13--23.

Arai, R., and Mabuchi, I. (2002). F-actin ring formation and the role of F-actin cables in the fission yeast Schizosaccharomyces pombe. J. Cell Sci. *115*, 887--898.

Bähler, J., Steever, A.B., Wheatley, S., Wang, Y., Pringle, J.R., Gould, K.L., and McCollum, D. (1998). Role of polo kinase and Mid1p in determining the site of cell division in fission yeast. J. Cell Biol. *143*, 1603--1616.

Balcer, H.I., Goodman, A.L., Rodal, A.A., Smith, E., Kugler, J., Heuser, J.E., and Goode, B.L. (2003). Coordinated Regulation of Actin Filament Turnover by a High-Molecular-Weight Srv2/CAP Complex, Cofilin, Profilin, and Aip1. Current Biology *13*, 2159--2169.

Bertin, A., McMurray, M.A., Pierson, J., Thai, L., McDonald, K.L., Zehr, E.A., Garcia, G., 3rd, Peters, P., Thorner, J., and Nogales, E. (2012). Three-dimensional ultrastructure of the septin filament network in Saccharomyces cerevisiae. Molecular biology of the cell *23*, 423-432.

Bi, E., Maddox, P., Lew, D.J., Salmon, E.D., McMillan, J.N., Yeh, E., and Pringle, J.R. (1998a). Involvement of an actomyosin contractile ring in Saccharomyces cerevisiae cytokinesis. The Journal of cell biology *142*, 1301-1312.

Bi, E., Maddox, P., Lew, D.J., Salmon, E.D., McMillan, J.N., Yeh, E., and Pringle, J.R. (1998b). Involvement of an actomyosin contractile ring in Saccharomyces cerevisiae cytokinesis. J Cell Biol *142*, 1301-1312.

Bi, E., and Park, H.O. (2012). Cell polarization and cytokinesis in budding yeast. Genetics *191*, 347-387.

Bidone, T.C., Tang, H., and Vavylonis, D. (2014). Dynamic Network Morphology and Tension Buildup in a 3D Model of Cytokinetic Ring Assembly. Biophys J *107*, 2618-2628.

Biro, M., Romeo, Y., Kroschwald, S., Bovellan, M., Boden, A., Tcherkezian, J., Roux, P.P., Charras, G., and Paluch, E.K. (2013). Cell cortex composition and homeostasis resolved by integrating proteomics and quantitative imaging. Cytoskeleton *70*, 741-754.

Blanchoin, L., Boujemaa-Paterski, R., Sykes, C., and Plastino, J. (2014). Actin dynamics, architecture, and mechanics in cell motility. Physiological reviews *94*, 235-263.

Bone, N., Millar, J.B., Toda, T., and Armstrong, J. (1998). Regulated vacuole fusion and fission in Schizosaccharomyces pombe: an osmotic response dependent on MAP kinases. Curr Biol *8*, 135-144.

Borukhov, I., Bruinsma, R.F., Gelbart, W.M., and Liu, A.J. (2005). Structural polymorphism of the cytoskeleton: a model of linker-assisted filament aggregation. Proceedings of the National Academy of Sciences of the United States of America *102*, 3673-3678.

Bugyi, B., Didry, D., and Carlier, M.F. (2010). How tropomyosin regulates lamellipodial actin-based motility: a combined biochemical and reconstituted motility approach. The EMBO journal *29*, 14-26.

Burke, T.A., Christensen, J.R., Barone, E., Suarez, C., Sirotkin, V., and Kovar, D.R. (2014). Homeostatic actin cytoskeleton networks are regulated by assembly factor competition for monomers. Current biology : CB *24*, 579-585.

Buttery, S.M., Yoshida, S., and Pellman, D. (2007). Yeast Formins Bni1 and Bnr1 Utilize Different Modes of Cortical Interaction during the Assembly of Actin Cables. Molecular Biology of the Cell *18*, 1826-1838.

Carlsson, A.E., Mogilner, A., and Carlier, M.-F. (2010). Mathematical and Physical Modeling of Actin Dynamics in Motile Cells

Actin-based Motility. In: Actin-based Motility, vol. 3: Springer Netherlands, 381-412.

Chan, Y.H., and Marshall, W.F. (2014). Organelle size scaling of the budding yeast vacuole is tuned by membrane trafficking rates. Biophys J *106*, 1986-1996.

Chaudhry, F., Breitsprecher, D., Little, K., Sharov, G., Sokolova, O., and Goode, B.L. (2013). Srv2/cyclase-associated protein forms hexameric shurikens that directly catalyze actin filament severing by cofilin. Mol Biol Cell *24*, 31-41.

Chen, Q., and Pollard, T.D. (2011). Actin filament severing by cofilin is more important for assembly than constriction of the cytokinetic contractile ring. J Cell Biol *195*, 485-498.

Cheng, D., Marner, J., and Rubenstein, P.A. (1999). Interaction in vivo and in vitro between the yeast fimbrin, SAC6P, and a polymerization-defective yeast actin (V266G and L267G). J Biol Chem *274*, 35873-35880.

Chesarone-Cataldo, M., Guerin, C., Yu, J.H., Wedlich-Soldner, R., Blanchoin, L., and Goode, B.L. (2011a). The myosin passenger protein Smy1 controls actin cable structure and dynamics by acting as a formin damper. Dev Cell *21*, 217-230.

Chesarone-Cataldo, M., Guerin, C., Yu, J.H., Wedlich-Soldner, R., Blanchoin, L., and Goode, B.L. (2011b). The myosin passenger protein Smy1 controls actin cable structure and dynamics by acting as a formin damper. Dev Cell *21*, 217-230.

Chesarone, M., Gould, C.J., Moseley, J.B., and Goode, B.L. (2009). Displacement of formins from growing barbed ends by bud14 is critical for actin cable architecture and function. Dev Cell *16*, 292-302.

Chesarone, M.A., DuPage, A.G., and Goode, B.L. (2010). Unleashing formins to remodel the actin and microtubule cytoskeletons. Nat Rev Mol Cell Biol *11*, 62-74.

Clark, A.G., Dierkes, K., and Paluch, E.K. (2013). Monitoring actin cortex thickness in live cells. Biophysical journal *105*, 570-580.

Clayton, J.E., Pollard, L.W., Sckolnick, M., Bookwalter, C.S., Hodges, A.R., Trybus, K.M., and Lord, M. (2014). Fission yeast tropomyosin specifies directed transport of myosin-V along actin cables. Molecular biology of the cell *25*, 66-75.

Clayton, J.E., Sammons, M.R., Stark, B.C., Hodges, A.R., and Lord, M. (2010). Differential regulation of unconventional fission yeast myosins via the actin track. Current biology : CB *20*, 1423-1431.

Coffman, V.C., Nile, A.H., Lee, I.J., Liu, H., and Wu, J.-Q. (2009). Roles of Formin Nodes and Myosin Motor Activity in Mid1p-dependent Contractile-Ring Assembly during Fission Yeast Cytokinesis. Mol. Biol. Cell *20*, 5195--5210.

Coffman, V.C., Sees, J.A., Kovar, D.R., and Wu, J.Q. (2013). The formins Cdc12 and For3 cooperate during contractile ring assembly in cytokinesis. The Journal of cell biology *203*, 101-114.

Courson, D.S., and Rock, R.S. (2010). Actin cross-link assembly and disassembly mechanics for alpha-Actinin and fascin. J Biol Chem *285*, 26350-26357.

Courtemanche, N., Lee, J.Y., Pollard, T.D., and Greene, E.C. (2013). Tension modulates actin filament polymerization mediated by formin and profilin. Proceedings of the National Academy of Sciences of the United States of America *110*, 9752-9757.

Cranz-Mileva, S., Pamula, M.C., Barua, B., Desai, B., Hong, Y.H., Russell, J., Trent, R., Wang, J., Walworth, N.C., and Hitchcock-DeGregori, S.E. (2013). A molecular evolution approach to study the roles of tropomyosin in fission yeast. PLoS One *8*, e76726.

Cyron, C.J., Muller, K.W., Schmoller, K.M., Bausch, A.R., Wall, W.A., and Bruinsma, R.F. (2013). Equilibrium phase diagram of semi-flexible polymer networks with linkers. Epl *102*.

Das, M., Drake, T., Wiley, D.J., Buchwald, P., Vavylonis, D., and Verde, F. (2012). Oscillatory dynamics of Cdc42 GTPase in the control of polarized growth. Science *337*, 239-243.

Das, M., MacKintosh, F.C., and Levine, A.J. (2007). Effective medium theory of semiflexible filamentous networks. Phys Rev Lett *99*, 038101.

Dasanayake, N.L., and Carlsson, A.E. (2013). Stress generation by myosin minifilaments in actin bundles. Physical biology *10*, 036006.

Ditlev, J.A., Mayer, B.J., and Loew, L.M. (2013). There is more than one way to model an elephant. Experiment-driven modeling of the actin cytoskeleton. Biophys J *104*, 520-532.

Drake, T., and Vavylonis, D. (2010). Cytoskeletal dynamics in fission yeast: a review of models for polarization and division. HFSP J *4*, 122-130.

Du, Y., Ferro-Novick, S., and Novick, P. (2004). Dynamics and inheritance of the endoplasmic reticulum. Journal of cell science *117*, 2871-2878.

Eggert, U.S., Mitchison, T.J., and Field, C.M. (2006). Animal cytokinesis: from parts list to mechanisms. Annu. Rev. Biochem. *75*, 543-566.

Estrada, P., Kim, J., Coleman, J., Walker, L., Dunn, B., Takizawa, P., Novick, P., and Ferro-Novick, S. (2003). Myo4p and She3p are required for cortical ER inheritance in Saccharomyces cerevisiae. J Cell Biol *163*, 1255-1266.

Evangelista, M., Pruyne, D., Amberg, D.C., Boone, C., and Bretscher, A. (2002). Formins direct Arp2/3-independent actin filament assembly to polarize cell growth in yeast. Nat. Cell Biol. *4*, 260--269.

Faix, J., and Grosse, R. (2006). Staying in Shape with Formins. Developmental Cell *10*, 693-706.

Falzone, T.T., Lenz, M., Kovar, D.R., and Gardel, M.L. (2012). Assembly kinetics determine the architecture of alpha-actinin crosslinked F-actin networks. Nat Commun *3*, 861.

Fan, X., Martin-Brown, S., Florens, L., and Li, R. (2008). Intrinsic capability of budding yeast cofilin to promote turnover of tropomyosin-bound actin filaments. PLoS One *3*, e3641.

Fehrenbacher, K.L., Davis, D., Wu, M., Boldogh, I., and Pon, L.A. (2002). Endoplasmic reticulum dynamics, inheritance, and cytoskeletal interactions in budding yeast. Molecular biology of the cell *13*, 854-865.

Feierbach, B., and Chang, F. (2001). Roles of the fission yeast formin for3p in cell polarity, actin cable formation and symmetric cell division. Current Biology *11*, 1656-1665.

Firat-Karalar, E.N., and Welch, M.D. (2011). New mechanisms and functions of actin nucleation. Curr Opin Cell Biol *23*, 4-13.

Fujime, S., and Maruyama, M. (1973). Spectrum of Light Quasielastically Scattered from Linear Macromolecules. Macromolecules *6*, 237-241.

Gao, L., and Bretscher, A. (2008). Analysis of Unregulated Formin Activity Reveals How Yeast Can Balance F-Actin Assembly between Different Microfilament-based Organizations. Mol. Biol. Cell.

Gao, L., and Bretscher, A. (2009). Polarized growth in budding yeast in the absence of a localized formin. Mol Biol Cell *20*, 2540-2548.

Gardel, M.L., Shin, J.H., MacKintosh, F.C., Mahadevan, L., Matsudaira, P., and Weitz, D.A. (2004). Elastic behavior of cross-linked and bundled actin networks. Science *304*, 1301-1305.

Gittes, F., B, M., Nettleton, J., and Howard, J. (1993a). Flexural rigidity of microtubules and actin filaments measured from thermal fluctuations in shape. J. Cell Biol. *120*, 923-934.

Gittes, F., Mickey, B., Nettleton, J., and Howard, J. (1993b). Flexural rigidity of microtubules and actin filaments measured from thermal fluctuations in shape. J. Cell Biol. *120*, 923-934.

Goode, B.L., and Eck, M.J. (2007). Mechanism and Function of Formins in the Control of Actin Assembly. Annual Review of Biochemistry *76*, 593–627.

Grallert, A., Martin-Garcia, R., Bagley, S., and Mulvihill, D.P. (2007). In vivo movement of the type V myosin Myo52 requires dimerisation but is independent of the neck domain. Journal of cell science *120*, 4093-4098.

Graziano, B.R., Yu, H.Y., Alioto, S.L., Eskin, J.A., Ydenberg, C.A., Waterman, D.P., Garabedian, M., and Goode, B.L. (2014). The F-BAR protein Hof1 tunes formin activity to sculpt actin cables during polarized growth. Mol Biol Cell *25*, 1730-1743.

Grooman, B., Fujiwara, I., Otey, C., and Upadhyaya, A. (2012). Morphology and viscoelasticity of actin networks formed with the mutually interacting crosslinkers: palladin and alpha-actinin. PLoS One *7*, e42773.

Haarer, B.K., Petzold, A., Lillie, S.H., and Brown, S.S. (1994). Identification of MYO4, a second class V myosin gene in yeast. Journal of cell science *107 (Pt 4)*, 1055-1064.

Hachet, O., and Simanis, V. (2008). Mid1p/anillin and the septation initiation network orchestrate contractile ring assembly for cytokinesis. Genes Dev *22*, 3205--3216.

Head, D.A., Levine, A.J., and MacKintosh, F.C. (2003). Deformation of cross-linked semiflexible polymer networks. Phys Rev Lett *91*, 108102.

Heussinger, C., Bathe, M., and Frey, E. (2007). Statistical mechanics of semiflexible bundles of wormlike polymer chains. Physical review letters *99*, 048101.

Higuchi, R., Vevea, J.D., Swayne, T.C., Chojnowski, R., Hill, V., Boldogh, I.R., and Pon, L.A. (2013). Actin dynamics affect mitochondrial quality control and aging in budding yeast. Curr Biol *23*, 2417-2422.

Hill, T.L. (1987). Linear aggregation theory in cell biology. Springer-Verlag: New York.

Hodges, A.R., Bookwalter, C.S., Krementsova, E.B., and Trybus, K.M. (2009). A nonprocessive class V myosin drives cargo processively when a kinesin- related protein is a passenger. Curr Biol *19*, 2121-2125.

Hodges, A.R., Krementsova, E.B., Bookwalter, C.S., Fagnant, P.M., Sladewski, T.E., and Trybus, K.M. (2012a). Tropomyosin is essential for processive movement of a class V myosin from budding yeast. Curr Biol *22*, 1410-1416.

Hodges, A.R., Krementsova, E.B., Bookwalter, C.S., Fagnant, P.M., Sladewski, T.E., and Trybus, K.M. (2012b). Tropomyosin Is Essential for Processive Movement of a Class V Myosin from Budding Yeast. Current Biology *22*, 1410-1416.

Hoog, J.L., Schwartz, C., Noon, A.T., O'Toole, E.T., Mastronarde, D.N., McIntosh, J.R., and Antony, C. (2007). Organization of interphase microtubules in fission yeast analyzed by electron tomography. Dev Cell *12*, 349-361.

Howard, J. (2001). Mechanics of Motor Proteins and the Cytoskeleton. Sinauer Associates.

Huang, J., Huang, Y., Yu, H., Subramanian, D., Padmanabhan, A., Thadani, R., Tao, Y., Tang, X., Wedlich-Soldner, R., and Balasubramanian, M.K. (2012). Nonmedially assembled F-actin cables incorporate into the actomyosin ring in fission yeast. J Cell Biol *199*, 831-847.

Huckaba, T.M., Lipkin, T., and Pon, L.A. (2006). Roles of type II myosin and a tropomyosin isoform in retrograde actin flow in budding yeast. J. Cell Biol. *175*, 957-969.

Iida, K., and Yahara, I. (1999). Cooperation of two actin-binding proteins, cofilin and Aip1, in Saccharomyces cerevisiae. Genes Cells *4*, 21-32.

Jegou, A., Carlier, M.F., and Romet-Lemonne, G. (2013). Formin mDia1 senses and generates mechanical forces on actin filaments. Nature communications *4*, 1883.

Johnston, G.C., Prendergast, J.A., and Singer, R.A. (1991). The Saccharomyces cerevisiae MYO2 gene encodes an essential myosin for vectorial transport of vesicles. J Cell Biol *113*, 539-551.

Kamasaki, T., Arai, R., Osumi, M., and Mabuchi, I. (2005). Directionality of F-actin cables changes during the fission yeast cell cycle. Nature Cell Biology *7*, 916-917.

Kamasaki, T., Osumi, M., and Mabuchi, I. (2007). Three-dimensional arrangement of F-actin in the contractile ring of fission yeast. J. Cell Biol. *178*, 765-771.

Karpova, T.S., McNally, J.G., Moltz, S.L., and Cooper, J.A. (1998). Assembly and function of the actin cytoskeleton of yeast: relationships between cables and patches. J Cell Biol *142*, 1501-1517.

Karpova, T.S., Tatchell, K., and Cooper, J.A. (1995). Actin filaments in yeast are unstable in the absence of capping protein or fimbrin. J. Cell Biol. *131*, 1483-1493.

Kierfeld, J., Kuhne, T., and Lipowsky, R. (2005). Discontinuous unbinding transitions of filament bundles. Phys Rev Lett *95*, 038102.

Kim, T., Hwang, W., and Kamm, R.D. (2009a). Computational Analysis of a Cross-linked Actin-like Network. Experimental Mechanics *49*, 91-104.

Kim, T., Hwang, W., Lee, H., and Kamm, R.D. (2009b). Computational analysis of viscoelastic properties of crosslinked actin networks. PLoS Comput Biol *5*, e1000439.

Klein, M.G., Shi, W., Ramagopal, U., Tseng, Y., Wirtz, D., Kovar, D.R., Staiger, C.J., and Almo, S.C. (2004). Structure of the actin crosslinking core of fimbrin. Structure *12*, 999-1013.

Klemm, R.W., Ejsing, C.S., Surma, M.A., Kaiser, H.J., Gerl, M.J., Sampaio, J.L., de Robillard, Q., Ferguson, C., Proszynski, T.J., Shevchenko, A., and Simons, K. (2009). Segregation of sphingolipids and sterols during formation of secretory vesicles at the trans-Golgi network. J Cell Biol *185*, 601-612.

Klionsky, D.J., Herman, P.K., and Emr, S.D. (1990). The fungal vacuole: composition, function, and biogenesis. Microbiol Rev *54*, 266-292.

Kojima, H., Ishijima, A., and Yanagida, T. (1994). Direct measurement of stiffness of single actin filaments with and without tropomyosin by in vitro nanomanipulation. Proc Natl Acad Sci U S A *91*, 12962-12966.

Kovar, D.R. (2005). Molecular details of formin-mediated actin assembly. Current Opinion in Cell Biology *18*, 11-17.

Kovar, D.R., and Pollard, T.D. (2004). Insertional assembly of actin filament barbed ends in association with formins produces piconewton forces. Proc. Natl. Acad. Sci. U S A *101*, 14725--14730.

Kovar, D.R., Sirotkin, V., and Lord, M. (2011). Three's company: the fission yeast actin cytoskeleton. Trends Cell Biol *21*, 177-187.

Kubler, E., and Riezman, H. (1993). Actin and fimbrin are required for the internalization step of endocytosis in yeast. EMBO J *12*, 2855-2862.

Kurniawan, N.A., Enemark, S., and Rajagopalan, R. (2012). The role of structure in the nonlinear mechanics of cross-linked semiflexible polymer networks. J Chem Phys *136*, 065101.

Laporte, D., Coffman, V.C., Lee, I.J., and Wu, J.Q. (2011). Assembly and architecture of precursor nodes during fission yeast cytokinesis. J Cell Biol *192*, 1005-1021.

Laporte, D., Courtout, F., Salin, B., Ceschin, J., and Sagot, I. (2013). An array of nuclear microtubules reorganizes the budding yeast nucleus during quiescence. J Cell Biol *203*, 585-594.

Laporte, D., Ojkic, N., Vavylonis, D., and Wu, J.Q. (2012). alpha-Actinin and fimbrin cooperate with myosin II to organize actomyosin bundles during contractile-ring assembly. Mol Biol Cell *23*, 3094-3110.

Lappalainen, P., and Drubin, D.G. (1997). Cofilin promotes rapid actin filament turnover in vivo. Nature *388*, 78-82.

Lee, I.J., Coffman, V.C., and Wu, J.Q. (2012). Contractile-ring assembly in fission yeast cytokinesis: Recent advances and new perspectives. Cytoskeleton *69*, 751-763.

Lipkin, T. (2011). Actin Cable Function and Regulation in the Budding Yeast, Saccharomyces cerevisiae, Columbia University, New York, NY.

Lippincott, J., and Li, R. (1998). Dual function of Cyk2, a cdc15/PSTPIP family protein, in regulating actomyosin ring dynamics and septin distribution. J Cell Biol *143*, 1947-1960.

Liu, H., and Bretscher, A. (1992). Characterization of TPM1 disrupted yeast cells indicates an involvement of tropomyosin in directed vesicular transport. J Cell Biol *118*, 285-299.

Liu, H.P., and Bretscher, A. (1989). Disruption of the single tropomyosin gene in yeast results in the disappearance of actin cables from the cytoskeleton. Cell *57*, 233-242.

Liu, W., Santiago-Tirado, F.H., and Bretscher, A. (2012). Yeast formin Bni1p has multiple localization regions that function in polarized growth and spindle orientation. Molecular biology of the cell *23*, 412-422.

Lo Presti, L., Chang, F., and Martin, S.G. (2012). Myosin Vs organize actin cables in fission yeast. Mol Biol Cell *23*, 4579-4591.

Lord, M., Laves, E., and Pollard, T.D. (2005). Cytokinesis depends on the motor domains of myosin-II in fission yeast but not in budding yeast. Mol. Biol. Cell *16*, 5346--5355.

Luo, W., Yu, C.H., Lieu, Z.Z., Allard, J., Mogilner, A., Sheetz, M.P., and Bershadsky, A.D. (2013). Analysis of the local organization and dynamics of cellular actin networks. The Journal of cell biology *202*, 1057-1073.

Martin, S.G., and Chang, F. (2006). Dynamics of the formin for3p in actin cable assembly. Curr. Biol. *16*, 1161-1170.

Martin, S.G., McDonald, W.H., Yates, J.R., and Chang, F. (2005). Tea4p Links Microtubule Plus Ends with the Formin For3p in the Establishment of Cell Polarity. Developmental Cell *8*, 479-491.

Matsushita, S., Adachi, T., Inoue, Y., Hojo, M., and Sokabe, M. (2010). Evaluation of extensional and torsional stiffness of single actin filaments by molecular dynamics analysis. J Biomech *43*, 3162-3167.

Mavrakis, M., Azou-Gros, Y., Tsai, F.C., Alvarado, J., Bertin, A., Iv, F., Kress, A., Brasselet, S., Koenderink, G.H., and Lecuit, T. (2014). Septins promote F-actin ring formation by crosslinking actin filaments into curved bundles. Nature cell biology *16*, 322-334.

Mehta, A.D., Rock, R.S., Rief, M., Spudich, J.A., Mooseker, M.S., and Cheney, R.E. (1999). Myosin-V is a processive actin-based motor. Nature *400*, 590-593.

Mendes Pinto, I., Rubinstein, B., Kucharavy, A., Unruh, J.R., and Li, R. (2012). Actin depolymerization drives actomyosin ring contraction during budding yeast cytokinesis. Developmental cell *22*, 1247-1260.

Meyer, R.K., and Aebi, U. (1990). Bundling of actin filaments by alpha-actinin depends on its molecular length. The Journal of cell biology *110*, 2013-2024.

Miao, Y., Wong, C.C., Mennella, V., Michelot, A., Agard, D.A., Holt, L.J., Yates, J.R., 3rd, and Drubin, D.G. (2013). Cell-cycle regulation of formin-mediated actin cable assembly. Proceedings of the National Academy of Sciences of the United States of America.

Milo, R. (2013). What is the total number of protein molecules per cell volume? A call to rethink some published values. Bioessays *35*, 1050-1055.

Mishra, M., Huang, J., and Balasubramanian, M.K. (2014). The yeast actin cytoskeleton. FEMS microbiology reviews *38*, 213-227.

Mogilner, A., and Odde, D. (2011). Modeling cellular processes in 3D. Trends Cell Biol *21*, 692-700.

Moon, A.L., Janmey, P.A., Louie, K.A., and Drubin, D.G. (1993). Cofilin is an essential component of the yeast cortical cytoskeleton. J Cell Biol *120*, 421-435.

Moseley, J.B., and Goode, B.L. (2005). Differential activities and regulation of Saccharomyces cerevisiae formin proteins Bni1 and Bnr1 by Bud6. J Biol Chem *280*, 28023-28033.

Moseley, J.B., and Goode, B.L. (2006). The yeast actin cytoskeleton: from cellular function to biochemical mechanism. Microbiol. Mol. Biol. Rev. *70*, 605-645.

Motegi, F., Nakano, K., and Mabuchi, I. (2000). Molecular mechanism of myosin-II assembly at the division site in Schizosaccharomyces pombe. J. Cell Sci. *113*, 1813--1825.

Muller, K.W., Bruinsma, R.F., Lieleg, O., Bausch, A.R., Wall, W.A., and Levine, A.J. (2014). Rheology of semiflexible bundle networks with transient linkers. Phys Rev Lett *112*, 238102.

Mulvihill, D.P., Pollard, P.J., Win, T.Z., and Hyams, J.S. (2001). Myosin V-mediated vacuole distribution and fusion in fission yeast. Curr Biol *11*, 1124-1127.

Nakano, K., and Mabuchi, I. (2006). Actin-capping protein is involved in controlling organization of actin cytoskeleton together with ADF/cofilin, profilin and F-actin crosslinking proteins in fission yeast. Genes Cells *11*, 893--905.

Nakano, K., Satoh, K., Morimatsu, A., Ohnuma, M., and Mabuchi, I. (2001). Interactions among a fimbrin, a capping protein, and an actin-depolymerizing factor in organization of the fission yeast actin cytoskeleton. Mol Biol Cell *12*, 3515-3526.

Naylor, S.G., and Morgan, D.O. (2014). Cdk1-dependent phosphorylation of Iqg1 governs actomyosin ring assembly prior to cytokinesis. Journal of cell science *127*, 1128-1137.

Nédélec, F., and Foethke, D. (2007). Collective Langevin dynamics of flexible cytoskeletal fibers. New Journal of Physics *9*, 427-451.

Nolen, B.J., Tomasevic, N., Russell, A., Pierce, D.W., Jia, Z., McCormick, C.D., Hartman, J., Sakowicz, R., and Pollard, T.D. (2009). Characterization of two classes of small molecule inhibitors of Arp2/3 complex. Nature *460*, 1031--1034.

Ojkic, N., and Vavylonis, D. (2010). Kinetics of Myosin node aggregation into a contractile ring. Phys. Rev. Lett. *105*, 048102.

Ojkic, N., Wu, J.Q., and Vavylonis, D. (2011). Model of myosin node aggregation into a contractile ring: the effect of local alignment. Journal of physics. Condensed matter : an Institute of Physics journal *23*, 374103.

Okada, K., Ravi, H., Smith, E.M., and Goode, B.L. (2006). Aip1 and cofilin promote rapid turnover of yeast actin patches and cables: a coordinated mechanism for severing and capping filaments. Mol Biol Cell *17*, 2855-2868.

Okreglak, V., and Drubin, D.G. (2010). Loss of Aip1 reveals a role in maintaining the actin monomer pool and an in vivo oligomer assembly pathway. The Journal of cell biology *188*, 769-777.

Pasquali, M., Shankar, V., and Morse, D.C. (2001). Viscoelasticity of dilute solutions of semiflexible polymers. Phys. Rev. E *64*, 020802.

Paul, A., and Pollard, T. (2008). The role of the FH1 domain and profilin in formin-mediated actin-filament elongation and nucleation. Curr. Biol. *18*, 9--19.

Pfaendtner, J., Branduardi, D., Parrinello, M., Pollard, T.D., and Voth, G.A. (2009). Nucleotide-dependent conformational states of actin. Proc Natl Acad Sci U S A *106*, 12723-12728.

Pfaendtner, J., Lyman, E., Pollard, T.D., and Voth, G.A. (2010). Structure and dynamics of the actin filament. J Mol Biol *396*, 252-263.

Pollard, T.D., and Borisy, G.G. (2003). Cellular Motility Driven by Assembly and Disassembly of Actin Filaments. Cell *112*, 453-465.

Pollard, T.D., and Cooper, J.A. (2009). Actin, a central player in cell shape and movement. Science *326*, 1208--1212.

Pollard, T.D., and Earnshaw, W.C. (2004). Cell biology. Saunders: Philadelphia.

Pollard, T.D., and Wu, J.-Q. (2010). Understanding cytokinesis: lessons from fission yeast. Nat Rev Mol Cell Biol *11*, 149--155.

Pruyne, D., Evangelista, M., Yang, C., Bi, E., Zigmond, S., Bretscher, A., and Boone, C. (2002). Role of Formins in Actin Assembly: Nucleation and Barbed-End Association. Science *297*, 612-615.

Pruyne, D., Legesse-Miller, A., Gao, L., Dong, Y., and Bretscher, A. (2004). Mechanisms Of Polarized Growth And Mechanisms Of Polarized Growth And Organelle Segregation In Yeast. Annu. Rev. Cell Dev. Biol *20*, 559-591.

Pruyne, D.W., Schott, D.H., and Bretscher, A. (1998). Tropomyosin-containing actin cables direct the Myo2p-dependent polarized delivery of secretory vesicles in budding yeast. J Cell Biol *143*, 1931-1945.

Reck-Peterson, S.L., Tyska, M.J., Novick, P.J., and Mooseker, M.S. (2001a). The yeast class V myosins, Myo2p and Myo4p, are nonprocessive actin-based motors. J Cell Biol *153*, 1121-1126.

Reck-Peterson, S.L., Tyska, M.J., Novick, P.J., and Mooseker, M.S. (2001b). The yeast class V myosins, Myo2p and Myo4p, are nonprocessive actin-based motors. The Journal of cell biology *153*, 1121-1126.

Reymann, A.C., Martiel, J.L., Cambier, T., Blanchoin, L., Boujemaa-Paterski, R., and Thery, M. (2010). Nucleation geometry governs ordered actin networks structures. Nat Mater *9*, 827-832.

Ridley, A.J. (2011). Life at the leading edge. Cell *145*, 1012-1022.

Rowland, A.A., and Voeltz, G.K. (2012). Endoplasmic reticulum-mitochondria contacts: function of the junction. Nature reviews. Molecular cell biology *13*, 607-625.

Sandrock, T.M., Brower, S.M., Toenjes, K.A., and Adams, A.E. (1999). Suppressor analysis of fimbrin (Sac6p) overexpression in yeast. Genetics *151*, 1287-1297.

Schmoller, K.M., Lieleg, O., and Bausch, A.R. (2008). Cross-linking molecules modify composite actin networks independently. Physical Review Letters *101*, 118102.

Schmoller, K.M., Semmrich, C., and Bausch, A.R. (2011). Slow down of actin depolymerization by cross-linking molecules. Journal of structural biology *173*, 350-357.

Schott, D., Ho, J., Pruyne, D., and Bretscher, A. (1999). The COOH-terminal domain of Myo2p, a yeast myosin V, has a direct role in secretory vesicle targeting. J Cell Biol *147*, 791-808.

Schott, D.H., Collins, R.N., and Bretscher, A. (2002a). Secretory vesicle transport velocity in living cells depends on the myosin-V lever arm length. J Cell Biol *156*, 35-39.

Schott, D.H., Collins, R.N., and Bretscher, A. (2002b). Secretory vesicle transport velocity in living cells depends on the myosin-V lever arm length. The Journal of cell biology *156*, 35-39.

Schreiber, C.H., Stewart, M., and Duke, T. (2010). Simulation of cell motility that reproduces the force-velocity relationship. Proc. Natl. Acad. Sci. U. S. A. *107*, 9141-9146.

Sept, D., and Carlsson, A.E. (2014). Modeling large-scale dynamic processes in the cell: polarization, waves, and division. Q Rev Biophys *47*, 221-248.

Shannon, K.B., and Li, R. (1999). The multiple roles of Cyk1p in the assembly and function of the actomyosin ring in budding yeast. Molecular biology of the cell *10*, 283-296.

Sheltzer, J.M., and Rose, M.D. (2009). The class V myosin Myo2p is required for Fus2p transport and actin polarization during the yeast mating response. Mol Biol Cell *20*, 2909-2919.

Sjoblom, B., Salmazo, A., and Djinovic-Carugo, K. (2008). Alpha-actinin structure and regulation. Cell Mol Life Sci *65*, 2688-2701.

Skau, C.T., Courson, D.S., Bestul, A.J., Winkelman, J.D., Rock, R.S., Sirotkin, V., and Kovar, D.R. (2011). Actin filament bundling by fimbrin is important for endocytosis, cytokinesis, and polarization in fission yeast. J Biol Chem *286*, 26964-26977.

Skau, C.T., and Kovar, D.R. (2010). Fimbrin and tropomyosin competition regulates endocytosis and cytokinesis kinetics in fission yeast. Curr Biol *20*, 1415--1422.

Smith, M.B., Li, H., Shen, T., Huang, X., Yusuf, E., and Vavylonis, D. (2010). Segmentation and tracking of cytoskeletal filaments using open active contours. Cytoskeleton *67*, 693--705.

Stachowiak, M.R., Laplante, C., Chin, H.F., Guirao, B., Karatekin, E., Pollard, T.D., and O'Shaughnessy, B. (2014). Mechanism of cytokinetic contractile ring constriction in fission yeast. Developmental cell *29*, 547-561.

Tang, H., Bidone, T.C., and Vavylonis, D. (2015). Computational model of actin cable and contractile ring formation in budding yeast. in preparation.

Tang, H., Laporte, D., and Vavylonis, D. (2014). Actin cable distribution and dynamics arising from cross-linking, motor pulling, and filament turnover. Mol Biol Cell *25*, 3006-3016.

Tolliday, N., VerPlank, L., and Li, R. (2002). Rho1 directs formin-mediated actin ring assembly during budding yeast cytokinesis. Curr Biol *12*, 1864-1870.

Tseng, Y., Schafer, B.W., Almo, S.C., and Wirtz, D. (2002). Functional synergy of actin filament cross-linking proteins. J Biol Chem *277*, 25609-25616.

Unterberger, M.J., and Holzapfel, G.A. (2014). Advances in the mechanical modeling of filamentous actin and its cross-linked networks on multiple scales. Biomech Model Mechanobiol *13*, 1155-1174.

Vallen, E.A., Caviston, J., and Bi, E. (2000). Roles of Hof1p, Bni1p, Bnr1p, and myo1p in cytokinesis in Saccharomyces cerevisiae. Mol Biol Cell *11*, 593-611.

Vavylonis, D., Wu, J.Q., Hao, S., O'Shaughnessy, B., and Pollard, T.D. (2008). Assembly mechanism of the contractile ring for cytokinesis by fission yeast. Science *319*, 97--100.

Vavylonis, D., Yang, Q., and O'Shaughnessy, B. (2005). Actin polymerization kinetics, cap structure, and fluctuations. Proc. Natl. Acad. Sci. U. S. A. *102*, 8543-5488.

Vidali, L., van Gisbergen, P.A.C., Guérin, C., Franco, P., Li, M., Burkart, G.M., Augustine, R.C., Blanchoin, L., and Bezanilla, M. (2009). Rapid formin-mediated actin-filament elongation is essential for polarized plant cell growth. Proc Natl Acad Sci U S A *106*, 13341--13346.

Voeltz, G.K., and Prinz, W.A. (2007). Sheets, ribbons and tubules - how organelles get their shape. Nat Rev Mol Cell Biol *8*, 258-264.

Volkmann, N., DeRosier, D., Matsudaira, P., and Hanein, D. (2001). An atomic model of actin filaments cross-linked by fimbrin and its implications for bundle assembly and function. J Cell Biol *153*, 947-956.

Wang, H., and Vavylonis, D. (2008). Model of For3p-mediated actin cable assembly in fission yeast. PLoS ONE *3*, e4078.

Wang, S., and Wolynes, P.G. (2012). Active contractility in actomyosin networks. Proceedings of the National Academy of Sciences of the United States of America *109*, 6446-6451.

Watanabe, M., Watanabe, D., Nogami, S., Morishita, S., and Ohya, Y. (2009). Comprehensive and quantitative analysis of yeast deletion mutants defective in apical and isotropic bud growth. Curr Genet *55*, 365-380.

West-Foyle, H., and Robinson, D.N. (2012). Cytokinesis mechanics and mechanosensing. Cytoskeleton *69*, 700-709.

West, M., Zurek, N., Hoenger, A., and Voeltz, G.K. (2011). A 3D analysis of yeast ER structure reveals how ER domains are organized by membrane curvature. J Cell Biol *193*, 333-346.

Win, T.Z., Gachet, Y., Mulvihill, D.P., May, K.M., and Hyams, J.S. (2001). Two type V myosins with non-overlapping functions in the fission yeast Schizosaccharomyces pombe: Myo52 is concerned with growth polarity and cytokinesis, Myo51 is a component of the cytokinetic actin ring. J. Cell Sci. *114*, 69--79.

Wu, J.Q., Bähler, J., and Pringle, J.R. (2001). Roles of a fimbrin and an alpha-actinin-like protein in fission yeast cell polarization and cytokinesis. Mol. Biol. Cell *12*, 1061--1077.

Wu, Y., Yan, J., Zhang, R., Qu, X., Ren, S., Chen, N., and Huang, S. (2010). Arabidopsis FIMBRIN5, an actin bundling factor, is required for pollen germination and pollen tube growth. Plant Cell *22*, 3745-3763.

Yamaoka, H., Matsushita, S., Shimada, Y., and Adachi, T. (2012). Multiscale modeling and mechanics of filamentous actin cytoskeleton. Biomech Model Mechanobiol *11*, 291-302.

Yang, H., and Pon, L.A. (2002). Actin cable dynamics in budding yeast. Proc. Natl. Acad. Sci. USA *99*, 751-756.

Yu, J.H., Crevenna, A.H., Bettenbuhl, M., Freisinger, T., and Wedlich-Soldner, R. (2011). Cortical actin dynamics driven by formins and myosin V. Journal of cell science *124*, 1533-1541.

Zhang, D., Vjestica, A., and Oliferenko, S. (2012). Plasma membrane tethering of the cortical ER necessitates its finely reticulated architecture. Curr Biol *22*, 2048-2052.

Vita

Haosu Tang
haosutang@gmail.com

Education:

Lehigh University 2010.8-2015.5
Bethlehem PA, USA
Ph. D., Physics

University of Science and Technology of China 2006.8-2010.7
Hefei, PR. China
B. S., Special Class for the Gifted Young, Physics, Optical Engineering and Information

Peer reviewed journal publications and conference proceedings:

1. **Haosu Tang**, Damien Laporte, Dimitrios Vavylonis, "Actin cable distribution and dynamics arising from cross-linking, motor pulling, and filament turnover", *Molecular Biology of the Cell* (2014).

2. Tamara C. Bidone, **Haosu Tang**, Dimitrios Vavylonis, "Insights into the mechanics of cytokinetic ring assembly using 3D modeling", *Proceedings of the ASME 2014 International Mechanical Engineering Conference* (2014).

3. Tamara C. Bidone, **Haosu Tang**, Dimitrios Vavylonis, "Dynamic Network Morphology and Tension Buildup in a 3D Model of Cytokinetic Ring Assembly", *Biophysical Journal* (2014)

4. **Haosu Tang**, Tamara C. Bidone, Dimitrios Vavylonis, Computational model of actin cable and contractile ring formation in budding yeast, *submitted for review*.

5. Tian Zhang, **Haosu Tang**, Dimitrios Vavylonis, Daniel J. Cosgrove, *work in progress*.

Conferences:

1). Biophysical Society 57th Annual Meeting, Philadelphia, PA: poster presentation, "Model of Yeast Actin Cable Distribution and Dynamics", February, 2013.

2). American Physical Society March Meeting 2013, Baltimore, MD: panel presentation, “Modeling the Distribution and Dynamics of Actin Cables”, March, 2013.

3). Biophysical Society Penn State Network Meeting, State College, PA: poster presentation, “Model of Yeast Actin Cable Distribution and Dynamics”, October, 2013.

4). American Society of Cell Biology 2013 meeting, New Orleans, LA: poster presentation, “Model of Yeast Actin Cable Distribution and Dynamics”, December, 2013.

5). American Society of Cell Biology 2014 meeting, Philadelphia, PA: poster presentation, “Organization of actin cables in budding yeast: a computational model”, December, 2014.